The Dissertation Committee for Dorinamaria Carka Certifies that this is the approved version of the following dissertation:

NON-LINEAR ANALYSIS OF FERROELASTIC/FERROELECTRIC MATERIALS

Committee:

Chad M. Landis, Supervisor

Rui Huang

Mark Mear

Krishnaswamy Ravi-Chandar

John L. Tassoulas

NON-LINEAR ANALYSIS OF FERROELASTIC/FERROELECTRIC MATERIALS

by

Dorinamaria Carka, Diploma; M.Sc.

Dissertation

Presented to the Faculty of the Graduate School of

The University of Texas at Austin

in Partial Fulfillment

of the Requirements

for the Degree of

Doctor of Philosophy

The University of Texas at Austin

December 2012

Acknowledgements

I owe a debt of gratitude to many generous and inspiring people. Their contribution to the completion of this work and to my development as a person and a scholar will always be cherished.

To my advisor Professor Chad M. Landis, for his gracious mentoring and his always invaluable vision. He has my utmost respect, admiration and heartfelt gratitude for all his effort and all that I learned from him during these years. Working with him has been a source of great intellectual wealth.

To the members of the Graduate Committee Professors Rui Huang, Mark Mear, K. Ravi-Chandar and John Tassoulas for generously giving their time and expertise. Their thoughtful criticism and suggestions are truly appreciated.

To Professor Mark Mear for his insightful contribution to the development of the numerical method as part of this work. To Professor John Huber for generously allowing me to use his optical micrographs of the ferroelectric domains.

To my current and past colleagues and friends Dr. Yiannis Korkolis, Dr. Wenyuan Li, Dr. Julian Hallai and Nikolas Bouklas for their help and advice on academic matters or not.

Finally, to the people that I love most and who with one way or another have taken this journey with me, but perhaps suffered more. To my parents Milto and Elvira for showing me the sky, teaching me how to fly and catching me when I fall. To my brother Genci, for not allowing the distance to get between us even though I missed so much of his growing up. To my life partner, colleague and best friend Stavros, whose presence, love and support always makes every adventure in life so much more interesting. It is to them that I dedicate this work.

NON-LINEAR ANALYSIS OF FERROELASTIC/FERROELECTRIC MATERIALS

Dorinamaria Carka, Ph.D.

The University of Texas at Austin, 2012

Supervisor: Chad M. Landis

Ferroelectric/ferroelastic ceramics are used in a range of smart structure applications, such as actuators and sensors due to their electromechanical coupling properties. However, their inherent brittleness makes them susceptible to cracking and understanding their fracture is of prominent importance.

A numerical study for a stationary, plane strain crack in a ferroelastic material is performed as part of this work. The stress and strain fields are analyzed using a constitutive law that accounts for the strain saturation, asymmetry in tension versus compression, Bauschinger effects, reverse switching, and remanent strain reorientation that can occur in these materials due to the non-proportional loading that arises near a crack tip. The far-field K-loading is applied using a numerical method developed for two-dimensional cracks allowing for the true infinite boundary conditions to be enforced. The J -integral is computed on various integration paths around the tip and the results are discussed in relation to energy release rate results for growing cracks and for stationary cracks in standard elastic–plastic materials.

In addition to the fracture studies, we examine the far field electromechanical loading conditions that favor the formation, existence and evolution of stable needle domain array patterns, using a phase-field modeling approach. Such needle arrays are often seen in experimental imaging of ferroelectric single crystals, where periodic arrays

of needle-shaped domains of a compatible polarization variant coexist with a homogeneous single domain parent variant. The infinite arrays of needles are modeled via a representative unit cell and the appropriate electrical and mechanical periodic boundary conditions. A theoretical investigation of the generalized loading conditions is carried out to determine the sets of averaged loading states that lead to stationary needle tip locations. The resulting boundary value problems are solved using a non-linear finite element method to determine the details of the needle shape as well as the field distributions around the needle tips.

Table of Contents

List of Tables

List of Figures

Chapter I Introduction

Ferroelectricity is the property of some pyroelectric crystals wherein the electric polarization of a material sample can be changed or switched due to the application of electric field. Materials exhibiting the property can be found in the form of bulk single crystals, thin films and ceramics with ABO_3 compositions such as barium and lead zirconate titanate and exhibit many interesting coupled effects. They possess large dielectric constant, piezoelectric, pyroelectric and electro-optical effects. Manipulation of the chemical composition and the methods in which they are fabricated and processed can further enhance the material properties.

The linear electromechanical properties have been traditionally exploited in many technological applications such as capacitors, transducers, optical and memory devices. A very informative historical and technological review on the tailoring of the properties on the plethora of applications can be found in Haertling (1999). In the last two decades there is increasing interest in the industrial use of ferroelectrics for their nonlinear properties, which will greatly facilitate the ongoing trend of miniaturization of devices in engineering applications (Scott, 2000).

Ferroelectric materials involve different length scales in their technologically useful forms, hence different approaches are employed in the analysis of the constitutive response. At the single crystal scale and when domain structure and evolution is analyzed, sharp and diffuse interface models of domain wall interactions dominate, while at the grain and polycrystalline level, phenomenological models are mainly employed. In this work both approaches are used for the nonlinear analysis of ferroelectric/ferroelastic materials. A phenomenological model is used to analyze the fracture of ferroelastic materials and a phase-field model approach is applied to simulate domain patterns.

Background information on both subject and a brief review of the main features of ferroelastic and ferroelectric materials, relevant to the thesis are presented in the remainder of the chapter.

1.1 FERROELECTRIC AND FERROELASTIC MATERIALS

In a historical review on ferroelectricity (Jaynes, 1953), referring to the work of Anderson, Nicolson and Cady in 1917 on the piezoelectric properties of Rochelle salt, describes the discovery of ferroelectricity as the observation of *"anomalies in the dielectric behavior, among which significant were the existence of hysteresis between applied electric field and polarization and a sudden change in polarization activity at* $23^{o}C$*"*. At this transition temperature, later called the Curie temperature, the 'anomaly' is experienced by a loss of centrosymmetry of the crystal. The distortion of the crystal structure and the relative displacement of the ions of the unit cell, create a permanent dipole moment per unit volume in the crystal (polarization).

A typical example of such a transition is the cubic to tetragonal transition experienced by barium titanate ($BaTiO_3$) at 120^0C. To demonstrate the range of physical properties of ferroelectrics, the unit cell of barium titanate, shown schematically in Figure 1.1.1 following Landis (http://www.ae.utexas.edu/~landis/Landis/Research.html) is employed. Above the Curie point, T_c, barium titanate is in its paraelectric cubic phase. The unit cell is composed of eight positively charged barium ions (Ba, +2) at the cube corners, six negatively charged oxygen ions (O, -2) in the center of the cube faces, and a positively charged titanium ion (Ti, +4) in the center of the cell. Below T_c, the central titanium ion will shift away from the center of the unit cell, displacing the centers of the positive and negative charge. The unit cell is spontaneously polarized in this state.

Applying an electric field, smaller that the coercive field of the material, on the spontaneously polarized cell, will cause the ions to move along with the electric field. On one hand, this change of the relative position of the centers of positive and negative charge is followed by a change of electric polarization, and this is the cause of the dielectric effect in ferroelectric materials.

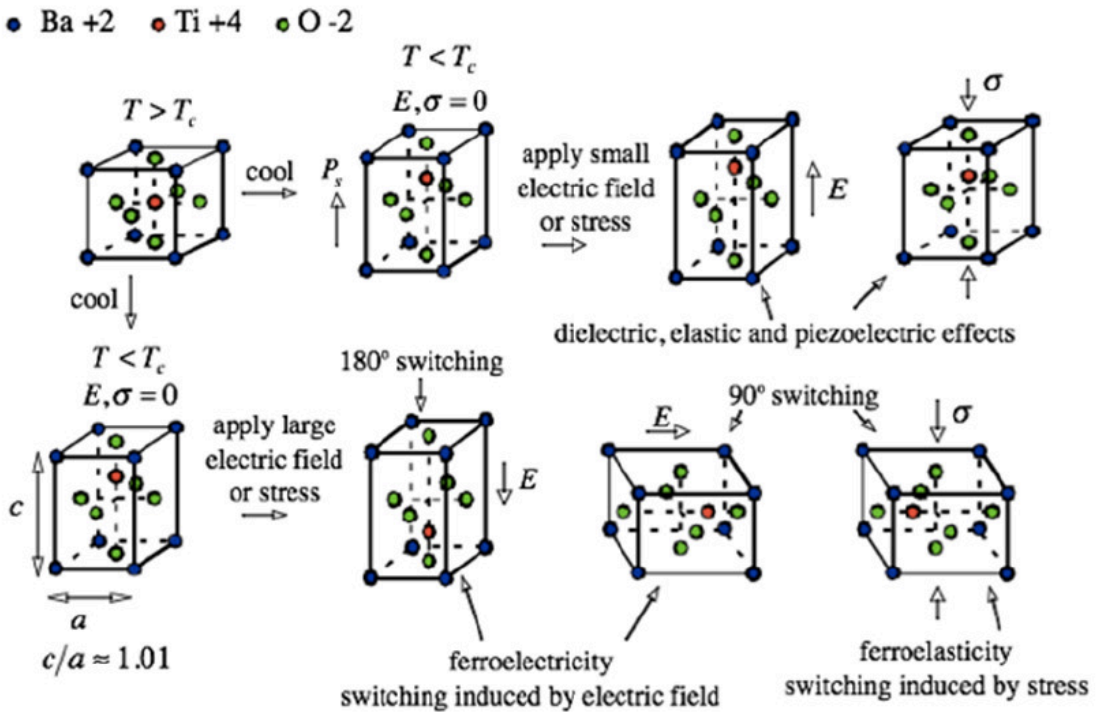

Figure 1.1.1 A simplified schematic of the crystal structure of barium titanate is illustrated above. Ferroelectric and ferroelastic switching behavior including the linear piezoelectric, dielectric and elastic effects are depicted. (http://www.ae.utexas.edu/~landis/Landis/Research.html)

On the other hand, the position change of the ions will cause an elongation or shortening of the cell, which leads to mechanical strain and the converse piezoelectric effect. The direct piezoelectric effect appears when a small stress is applied. Elongation or shortening of the unit cell will change the relative positions of the centers of positively

and negatively charged ions, inducing a change of the electric polarization. Finally the geometric change of the unit cell induced by the stress field is observed as mechanical strain, and this effect is the elastic material response.

Application of large electric field, larger than the coercive field of the material, will permanently pole the unit cell along the direction favored by the loading, giving rise to the ferroelectric response. Application of electric field parallel and at the opposite direction of the polarization vector will cause the polarization vector to switch by 180^o or 90^o if the electric field is applied perpendicularly to the polarization vector. Application of large mechanical stress can cause 90^o switching of the polarization direction, giving rise to the ferroelastic response of the unit cell.

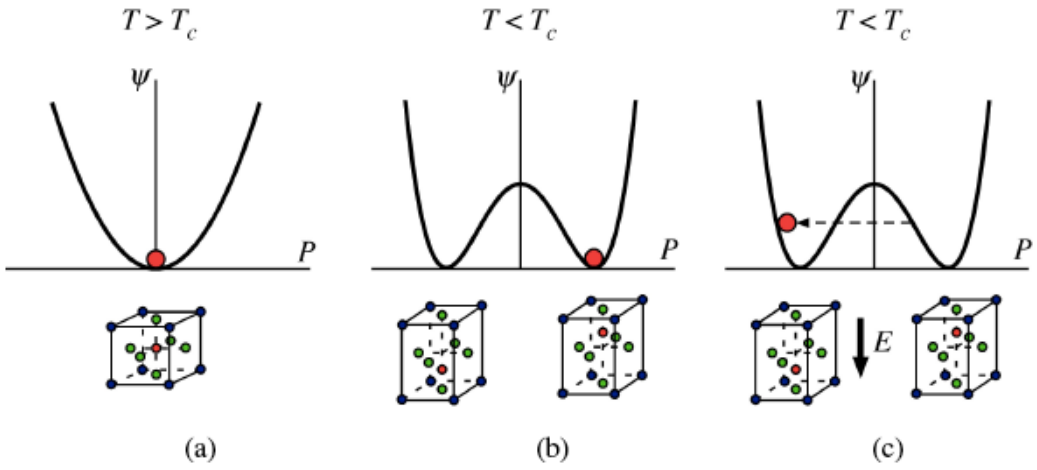

Figure 1.1.2 Schematic of the free energy of the perovskite crystal structure of barium titanate at different temperatures. (a) Above the Curie Temperature T_C the material is in the high temperature cubic phase and the free energy is convex with a single well at zero polarization. (a) Below T_C the low temperature phase is tetragonal and the free energy becomes non-convex with multiple wells associated with the possible spontaneous polarization states. (c) Polarization switching under the application of large electric field.

In terms of free energy $\Psi(P)$, the stable ferroelectric state associated with the spontaneous polarization and 180° switching is depicted in Figure 1.1.2. In Figure 1.1.2(a), above the Curie temperature T_C, the high temperature phase is cubic and the polarization of the unit cell is equal to zero. The material free energy is convex in this case with a single well at zero polarization depicting the stable phase. Below the Curie temperature, a cubic to tetragonal phase transition occurs giving rise to possible spontaneous polarization states along crystallographic planes. The material free energy is non-convex in this case with multiple wells associated with the stable possible spontaneous polarization states as shown Figure 1.1.2(b). The zero-polarization state is still an equilibrium state but it is no longer stable. Under the application of a strong electric field, the energy barrier between equilibrium states can be overcome and the polarization can switch by 180°, switching from one energy well to another as depicted in Figure 1.1.2(c).

Typical idealized constitutive response of the ferroelectric unit cell is shown in Figure 1.1.3. Figure 1.1.3a shows the hysteretic loop between polarization and applied field as derived from the double-well potential characteristic of these materials. The red part is unstable and cannot exist homogeneously throughout the material. The dashed lines intersect the electric field axis at the coercive field value of the unit cell. The blue lines intersect the polarization axis at points corresponding to the spontaneous polarization of the cell. As discussed above the change in polarization also causes straining of the unit cell. This electrostrictive effect also causes a hysteretic behavior, known as butterfly loop, between the strain and the applied field, shown in Figure 1.1.3b. The spontaneous strain in this case and the coercive field can be readily inferred in the graph.

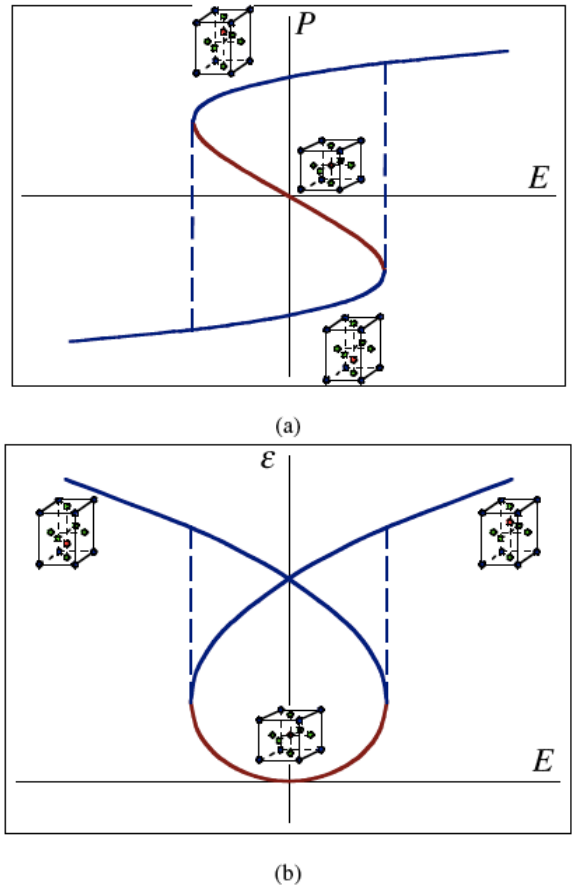

Figure 1.1.3 The (a) polarization and (b) strain as the function of the electric field below the Curie temperature T_c. The red portions of the curves correspond to unstable states, and the crystal jumps directly along the dashed line.

1.1.1 Ferroelastic and Ferroelectric Microstructure

In the previous section, the unit cell of barium titanate was employed to discuss the electromechanical properties of ferroelectric materials. However, the technologically useful form of ferroelectric materials takes advantage of the formation of microstructure in order to enhance the material constitutive response by integrating the properties arising from the unit cell. Unless otherwise fabricated, typical single crystals or polycrystalline

ferroelectric materials break into complex domain structures upon cooling from the Curie temperature.

These low energy configurations are contain domains or twins, which are regions with the individual electric dipoles of the unit cell aligned. Domains form in each grain or in the single crystal in order to accommodate local and global equilibrium and continuity of electromechanical fields along with energy minimization preferences creating a domain structure in the crystal. The interface separating different domains or variants of uniform spontaneous polarization is called a domain wall. Switching takes place by means of the displacement of these boundaries between domains and is the primary mechanism responsible for nonlinear ferroelectric constitutive response.

In the as-cooled state the average strain and polarization of the crystal are zero and mechanical loading will lead to purely ferroelastic response. In fact poling of the material is a necessary step for piezoelectricity to appear in the case of multi-domain single crystals and polycrystalline materials. The permanent spontaneous polarization can then be reduced to zero and 'switched' to a reversed direction under the influence of electric field through domain wall motion as in the ferroelastic case, giving rise to the non-linear and coupled ferroelectric behavior in these crystals. The mobility of the existing twin or domain boundaries will greatly influence the ferroelastic/ferroelectric hysteretic behavior and by manipulating the microstructure the overall response and properties can be enhanced.

The orientation of domain walls in infinite ferroelectric crystals, was theoretically investigated by Fousek and Janovec (1969). Permissible wall orientations that satisfy mechanical compatibility can have arbitrary orientation (W_∞) or prominent crystallographic directions (W_f). It is also possible for the orientation of the permissible domain walls to depend on the electromechanical coefficients and temperature (S).

Between a pair of domains in a given ferroelectric material the domain wall can be either of the W_∞ type, or one of the W_f or S type. The permissible walls can be either charged or neutral. Domain wall orientations, that minimize the crystal free energy, satisfying both the charge and mechanical compatibility have been investigated by Shu and Bhattacharya (2001). Models that take into account strain and charge compatibility across the domain walls have been successfully applied to predict minimum energy lamellar domain structures for a given average strain and polarization (Lu and Liu, 2004, Tsou and Huber, 2010).

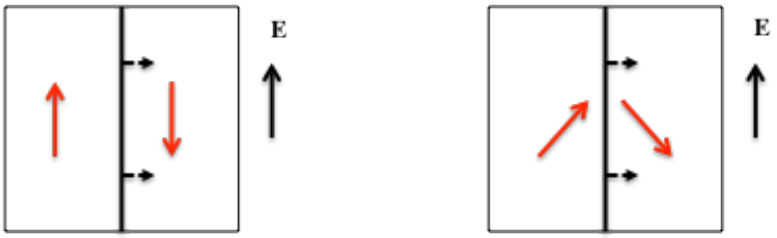

Figure 1.1.4 Schematic of planar 180^0 and 90^0 domain walls. Application of electric field parallel to the domain wall favoring the left variant will cause the domain structure to switch by (a)180^0 and (b) 90^0 by domain wall motion .

Examples of such compatible domain wall orientations in $BaTiO_3$, are the 90^0 walls of the W_f type, along [110] crystallographic orientations and the 180^0 of the W_∞ type, shown in Figure 1.1.4. Application of electric field will cause switching by planar domain wall motion in order for the variant favored by the loading to expand at the expense of the other. Figure 1.1.4(a) and Figure 1.1.4(b) show domain wall motion that causes 180^0 and 90^0 switching respectively. As discussed above, 90^o switching can be caused by the application of mechanical stress in an unpoled ferroelectric crystal. Typical idealized ferroelastic constitutive response of a multi-domain single crystal is shown in the schematic shown in Figure 1.1.5 (Landis, 2003). An interesting feature of ferroelastic

materials is the asymmetry in tension versus compression in the uniaxial stress-strain response. The asymmetry can be realized with a thought experiment described in detail by Landis, (Landis 2003). Assuming three equal volumes of possible tetragonal variants in the crystal and loading along one polar axis in tension, two of the three variants are available to switch to accommodate the loading. On the other hand, loading in compression along a polar axis only one variant can switch to accommodate the loading.

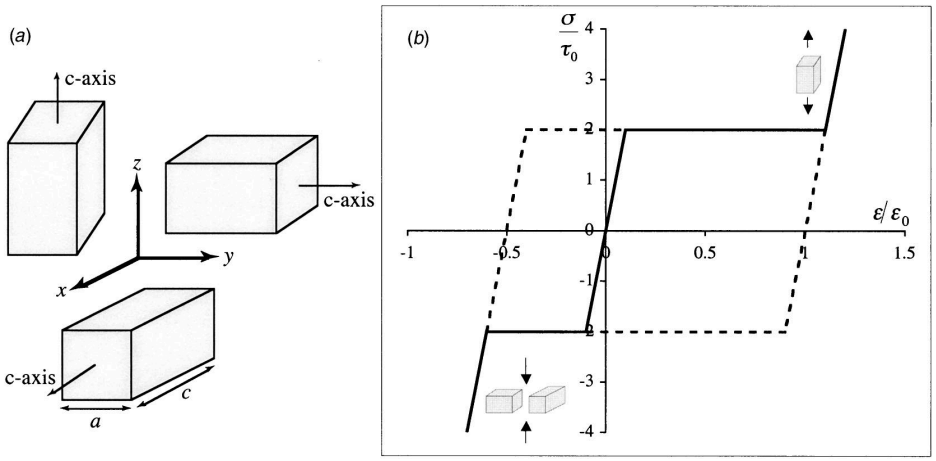

Figure 1.1.5 (a) Three possible orientations of tetragonal variants coexisting within a single crystal separated by a domain wall or twin boundary. (b) The asymmetric in tension versus compression uniaxial stress-strain response of a model single crystal loaded along any of the polar directions (Landis, 2003).

Ferroelectricity is a broad subject and one should only hope to give a brief review. More comprehensive treatments on can be found in many excellent texts and review articles covering the ferroelectric phenomenon (Jona and Shirane, 1962; Jaynes, 1953; Devonshire, 1954; Scott 2000, Damjanovic, 1998; Xu, 1991, Tagantsev et al, 2010, Haertling, 1999).

1.2 Ferroelastic Fracture, Motivation and Background

The first part of this dissertation deals with the understanding of the fracture properties of ferroelastic ceramics. There have been many excellent experimental and theoretical investigations on the fracture properties of ferroelectrics, recently summarized by Schneider (2007) and Kuna (2010). To model the effects of domain switching Yang and Zhu (1998) and Reece and Guiu (2002) followed the approaches of McMeeking and Evans (1982) and Budiansky et al (1983) for transformation toughening in materials undergoing a dilatant phase transformation. These models assume that a given material point consists of a single domain variant and switching between variants is driven by an energetic criterion, e.g. Kessler and Balke (2001). Such a description of the material is physically reasonable, but to fully model a ferroelectric in this manner would require the tracking of the locations and interactions of many domain walls. To carry out such a program for millimeter to centimeter sized samples of material would be computationally intensive.

A second approach taken by Landis (2003b) and Wang and Landis (2004, 2006) is to implement a phenomenological constitutive law to describe ferroelastic/ferroelectric switching within detailed finite element computations of the electromechanical fields around the crack tip. In contrast to the transformation-type switching model, a material point can contain multiple domain variants. To date such calculations have been performed on growing cracks to determine the amount of toughening that is provided by domain switching during crack growth. Some of the successes of this approach include the prediction of switching zones with a gradation of switching strain and similar R-curve toughening enhancements for both unpoled material and the same material poled parallel to the crack front as observed by Hackemann and Pfeiffer (2003) and Jones et al (2007).

In this work a phenomenological constitutive law of Landis (2003b) is used to study the mechanical fields near a stationary crack tip in a ferroelastic material. A brief introduction on some computational aspects of nonlinear fracture mechanics addressed in the dissertation and also applied to elastic-plastic materials will be given next.

1.2 1 Fracture Mechanics Concepts, Crack Tip Fields and the J –integral

The study of the stress and strain fields near cracks plays a central role in theoretical fracture mechanics. For non-linear fracture mechanics one goal is to compute the distributions of stress and strain near a crack tip as a result of nonlinear material behaviors like plasticity, phase transformation, dislocation emission, and the like. For situations where the region of non-linear material response is very small compared to all other specimen dimensions, Rice (1968) introduced the concept of a boundary layer approach to analyze small-scale yielding. Rice's approach is now almost universally adopted for small-scale yielding studies, wherein a semi-infinite crack is analyzed with far-field loading characterized by the linear elastic stress intensity factors. Since the non-linear material response near the crack tip usually requires the finite-element method for the analysis, the common procedure for dealing with the far-field boundary conditions is to mesh a large but finite domain and apply tractions or displacements associated with the *K*-fields to the outer boundary. Clearly modeling errors are introduced when analyzing a finite domain, and the true small-scale yielding assumptions are attained in the limit as the ratio of the size of the non-linear material process zone to the size of the domain tends to zero.

In linear elastic fracture mechanics (LEFM) the objective is to determine the stress intensity factors for a specific specimen shape and loading. In all but the simplest geometrical configurations some type of numerical method is required to solve this

problem. The implementation of standard non-singular finite elements for crack problems leads to issues with convergence associated with the singular stress and strain fields near the crack tip. This issue can be alleviated to some extent by the introduction of a ring of singular finite-elements around the crack tip (Barsoum, 1977; Manu, 1985), but the radial dimension of this ring of elements still needs to be relatively small to obtain accurate results for the stress intensity factors (Shih et al., 1976). Alternatively, the crack tip singularity can be represented by the employment of semi-analytical methods. In linear elastic fracture mechanics, Song and Wolf (2002) applied the scaled boundary finite element method to represent the crack tip singularity in bounded and unbounded domains.

One approach to address both of the infinite domain and crack tip region problems is to couple an analytic series solution to the finite-element solution. The infinite domain problem was solved by Givoli and Keller (1989) in regions without branch cuts, and crack tip and corner problems were solved for the longitudinal shear case by Givoli et al (Givoli et al, 1992; 1993). Givoli and co-workers (Givoli, 1991; 1992; 1999; Givoli et al, 1989; 1992; 1993; 1990; 1994; 1998, Keller et al, 1989) have named their method the *Dirichlet to Neumann map*. Hilton and Hutchinson (1971) applied a very similar approach to study the plastic zones near crack tips in longitudinal shear loading. Landis (2002) combined the approaches of Givoli and Keller (1989) and Givoli et al. (1992) to study switching zones for longitudinal shear and electrical loading in ferroelastic/ferroelectric materials, and found that the method is able to very accurately reproduce closed-form results (Rice, 1967; Landis, 2002). Landis, (2002) used similar boundary conditions to study mode III and analogous electrical mode E crack tip fields, and has shown that this numerical approach provides highly accurate agreement with the analytical results due to Rice (1967).

Absent from the list of problems solved by Givoli and co-workers are elastostatic problems with branch cuts, of which two-dimensional crack problems are of significant interest. Here we adopt this terminology due to the similarity of the approach and a DtN map for two-dimensional cracks is developed.

1.3 THE J INTEGRAL

The J -integral as introduced by Eshelby (1956; 1970) and Rice (1968) is a useful quantity for the analysis of mechanical fields near crack tips in both linear elastic and nonlinear elastic materials. For nonlinear elastic materials, it is well known that the J -integral is equivalent to the energy release rate (Eshelby, 1956; 1970; Rice, 1968). Additionally, J has been used in several studies to characterize the intensity of stress and deformation fields near cracks in power-law hardening materials (Rice, 1968; Rice and Rosengreen, 1968, Hutchinson, 1968; Shih, 1974, Shih, 1981). It is established that J is a path-independent integral when the material is nonlinear elastic (Rice, 1968; 1968). As such, the path-independence of J rigorously holds in elastic-plastic materials when the material response is governed by the deformation theory of plasticity or when flow theory exactly mimics deformation theory, where proportional loading occurs at all points within the domain.

Rice (1967; 1968) demonstrated that, in fact, flow theory plasticity does perfectly mimic deformation theory near a stationary crack tip loaded in mode III in an elastic-power-law hardening material under small-scale yielding conditions. Hence, for mode III, the J -integral is path-independent for small-scale yielding. No such proof of the path-independence of J is available for the in plane loading modes and we will show that J is not path independent in cases with a mode I component. In any situation where a significant amount of non-proportional loading occurs, it is expected that the J -integral

will not be path independent. For example, McMeeking (1977) analyzed the effects of finite deformation near a mode I crack and found that the blunting of the crack tip causes significant non proportional plastic loading, which results in the path-dependence of J. Rice and coworkers (Rise and Rosengreen, 1978; Drugan et al, 1982) showed that for steadily growing cracks, where there is a significant amount of non proportional straining including elastic unloading and plastic reloading, causing the strain singularity in an elastic-perfectly plastic material to be $\ln 1/r$ and, hence, J evaluated around a contour close to the crack tip is zero. In this work, we consider stationary crack tip and the effects of both infinitesimal and finite deformation and J is found to be path dependent. Since proportional loading is not guaranteed for in plane loading modes the finding that J is path-dependent is not entirely unexpected. However, the amount of path-dependence is an unforeseen result.

1.4 Phase Field Modeling of Needle Domains, Motivation and Background

The second part of the dissertation deals with the modeling of the microstructure of ferroelectric single crystals. The behavior of ferroelastic and ferroelectric materials is directly linked to the natural domain patterns occurring at the grain level upon cooling from the Curie temperature and the evolution of the microstructure through domain wall motion upon electromechanical loading. Understanding and modeling the ferroelectric domain structure is a great part of successfully engineering new ferroelectric materials. Reviews of recent developments on the subject can be found in Liu and Lynch (2006) and Pontis et al (2011) and the references therein.

As discussed in section 1.1.2, ferroelectric microstructure is formed to achieve global and local energy minimization within the crystal. The microstructure appears in the form of uniformly polarized regions, domains, which are separated by thin regions of

varying polarization called domain walls. Theoretically the minimization of the elastic and electrostatic energy is favored by the formation of stress free domain configurations with compatible spontaneous strain and charge neutrality between the spontaneously polarized domains.

However, in a finite and imperfect crystal deviations from the predicted orientations are expected and often encountered. Usual domain structures in ferroelectric single crystals that deviate from the predicted orientation are wedge domains or compatible lamellar patterns terminating within the crystal, with needle or wedge like tips. They were first observed and described by Forsbergh (1949) and Little (1954) in $BaTiO_3$ in single crystals and later experimentally investigated by many researchers. Needle and wedge domains, appear in the crystal after cooling in extended regions in the crystal where a domain variant with a polarization direction perpendicular to a parent domain, surrounding phase is exists. The existence of needle or wedge domains causes stresses in the surrounding area in the crystal. The tips can be electrically charged since locally there is deviation from the charge free wall orientation. However, the domains at the tip can be further divided into compatible 180^0 domains such that electric neutrality is approached on average (Tagantsev et al, 2010).

Fousek and Brezina (1961a) using a simple model investigated the conditions for the existence of wedge domains caused by internal defects. Salje and Ishibashi (1996) investigated the pinning of domain walls in ferroelastic crystals due to internal defects and predicted energetically favored needle trajectories, and Salje et al. (1998) compared the predicted results to experimental observations in minerals. Novak et al. (2002) simulated equilibrium shapes of needles with respect to a free surface using a two-dimensional discrete ferroelastic lattice model. Recently, needle configurations were

experimentally examined as possible natural flux closure states in thin barium titanate singe crystals (McGilly et al, 2010).

The existence and evolution of needle and wedge domains has a pronounced effect on the electrical and electromechanical properties of ferroelectric ceramics. The mobility of wedge domains in an electric field, differs from the mobility of planar walls, contributing to the initial permittivity of the material (1961b). Pointis and Huber (2012) used optical microscopy to observe that needle configurations of different spacing and volume fraction, like the ones modeled in this work, respond differently to stress having a influence ferroelastic switching criterion of the $BaTiO_3$ crystal.

Here we employ a phase-field approach to model the equilibrium and evolution of needle-like configurations commonly found in bulk single crystal barium titanate. In contrast with sharp interface models, diffuse interface or phase-field approaches allow for the nucleation of domains naturally without any specific rules, which is accomplished by defining a material free energy that depends on the mechanical strain, the electric field and the electric polarization in the material. Employing the material polarization as the order parameter, the phase-field approach allows for a detailed accounting of the electromechanical processes that occur during the nucleation and growth of domains.

The phase-field modeling approach has been used successfully to study several different features of ferroelectric domain switching behavior including the structure of domain walls (Cao and Cross, 1991), switching of polycrystals and single crystals (Chaudhury et al, 2005; Zhang and Bhattacharya, 2005), the interactions of domain walls with charge defects (Su and Landis, 2007) and dislocations (Kontsos and Landis, 2009), domain switching (Song et al, 2007) and nucleation and growth near crack tips (Li and Landis, 2011). Details on the method will be presented in chapter IV.

1.5 OUTLINE

The remainder of the dissertation is organized as follows. Chapter II presents the method for coupling an analytic series solution to a finite-element solution for two dimensional crack problems. The method is applied to the determination of the stress intensity factors and *T*-stress in a set of problems in linear elastic fracture mechanics. The classic problem of plane strain, stationary crack under of small-scale yielding in a nonlinear elastic is then analyzed in order to create a reliable computational template addressing most aspects associated with the correct representation of crack tip fields and the calculation of the J -integral. Then, interesting results for a crack in an elastic-plastic material are presented.

Chapter III presents computations of the stress and remanent strain fields, the switching zone shape and size, along with results for the path-dependence of the J -integral around stationary cracks in ferroelastic materials. The phenomenological constitutive law, used to describe the constitutive response of the ferroelastic polycrystalline and the results f the analysis are discussed in relation to their steady crack growth counterparts.

Chapter IV is devoted to the phase-field modeling of infinite arrays of domain needles. The domain pattern is modeled via a representative unit cell and the appropriate electrical and mechanical periodic boundary conditions are applied. A theoretical investigation of the generalized loading conditions is carried out to determine the loading states that lead to stationary needle tip locations. The resulting boundary value problems are solved using a non-linear finite element method to determine the details of the needle shape as well as the field distributions around the needle tips.

Chapter II Analysis of 2-D Cracks in Elastic-Plastic Materials

A series of two dimensional crack problems can be studied by employing the Dirichlet-to-Neumann map. For linear elastic fracture mechanics problems, the interior map is used around the crack tip, away from the geometric complexities of the specimen boundary and stress intensity factors are computed. For small-scale yielding problems, the map is used in the infinite region away from the non-linear process zone surrounding the crack tip. In this case, the effect of the far field boundary conditions along with other computational aspects of fracture mechanics are discussed and results for the crack tip fields and the J -integral are presented for elastic-plastic materials.

2.1 The Dirichlet-to-Neumann Map for Two-Dimensional Crack Problems

The two classes of crack problems that can be studied with the Dirichlet to Neumann map by coupling an analytic solution to the finite-element method are shown in Figure 2.1.1. The first class of problems, Figure 2.1.1(b), considers entirely linear elastic domains with irregular external boundaries and/or complex applied loadings. In this case, the Dirichlet-to-Neumann map is used to represent a circular region surrounding the crack tip. The finite-element method is used for the external region and the mixed mode stress intensity factors and the T-stress are retrieved from the map.

The second, shown in Figure 2.1.1(a), considers problems where non-linear constitutive processes occur in a small region near the crack tip and the remotely applied loading can be characterized by the linear elastic K-field and perhaps the T-stress. Here, the finite-element method is applied in a circular region around the crack tip where non-linear constitutive response is occurring, and stiffness contributions associated with the Dirichlet-to-Neumann map are imposed on the circular boundary to account for the large surrounding elastic domain and the remote applied loading. The general theory for

coupling regions described by an analytic solution to regions represented by a numerical solution obtained from the finite-element method will be presented next.

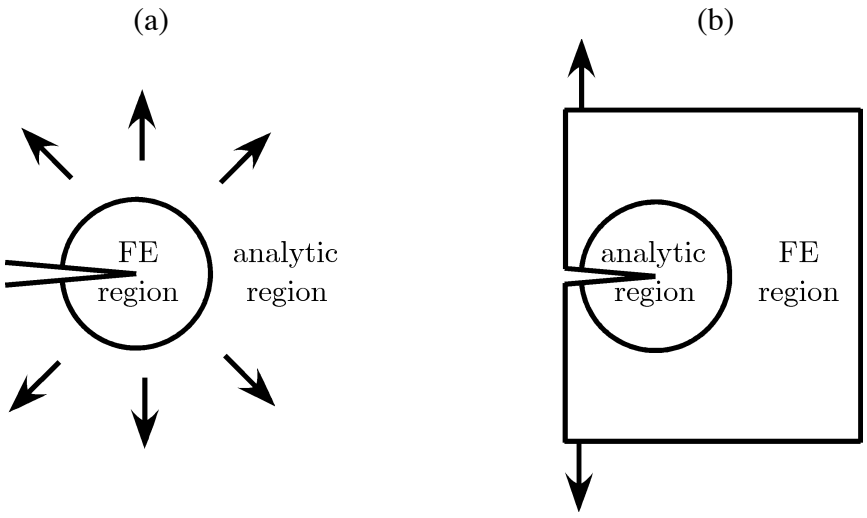

Figure 2.1.1. (a) Semi-infinite crack problems with non-linear material behavior near the crack tip. (b) Linear elastic fracture mechanics problems with complex geometry and loading. The finite-element (FE) and analytic regions of the solution method are illustrated on each figure.

2.1.2 Theory

Consider the principle of virtual work for the entire domain represented by Figure 2.1.1.

$$\int_V \sigma_{ji}\, \delta\varepsilon_{ij}\, dV = \int_S t_i\, \delta u_i\, dS \tag{2.1}$$

In Equation (2.1) σ_{ij}, ε_{ij}, t_i, u_i are the Cartesian components of the stress tensor, infinitesimal strain tensor, traction, and displacement respectively. Standard Einstein notation is used with summation implied over repeated indices. The stress and traction

are equilibrated at the surface S such that $t_i = \sigma_{ji} n_j$ on S, where n_i are the components of the unit normal vector to the surface. Additionally, the strain and displacement are linked kinematically as, $\varepsilon_{ij} = (u_{i,j} + u_{j,i})/2$. The δ indicates that the quantity following it is allowed to undergo an arbitrary variation. The initial step in the formulation is to partition the domain V into two regions, one where the solution is represented numerically via finite-elements V_{FE}, and the remainder of the domain where the solution is represented analytically V_A. The regions V_{FE} and V_A are mutually exclusive, but share a common boundary $S_{A/FE}$. The principle of virtual work is now written as

$$\int_{V_{FE}} \sigma_{ji}^{FE} \delta\varepsilon_{ij}\, dV + \int_{V_A} \sigma_{ji}^{A} \delta\varepsilon_{ij}\, dV = \int_{S_{FE}} t_i^{FE} \delta u_i\, dS + \int_{S_A} t_i^{A} \delta u_i\, dS. \tag{2.2}$$

The superscripts *FE* and *A* have been added to indicate the solutions in the finite-element and analytic regions respectively. S_A is the part of the surface surrounding V_A that is not shared by V_{FE}, and S_{FE} is the part of the surface surrounding V_{FE} that is not shared by V_A. Applying the divergence theorem to the second term on the left-hand side of (2.2) then yields

$$\begin{aligned} \int_{V_{FE}} \sigma_{ji}^{FE} \delta\varepsilon_{ij}\, dV + \int_{S_{A/FE}} t_i^{A} \delta u_i\, dS + \int_{S_A} t_i^{A} \delta u_i\, dS \\ = \int_{S_{FE}} t_i^{FE} \delta u_i\, dS + \int_{S_A} t_i^{A} \delta u_i\, dS. \end{aligned} \tag{2.3}$$

Clearly, the last terms on each side of this equality cancel, and we are left with the form of principle of virtual work that is applied to develop the numerical approach. The method is based upon the realization that the solution in V_A can be represented

analytically, and for linear elastic regions this will be accomplished with an infinite series. Specifically, the displacement field is taken in the form

$$u_i^A = \sum_n C^n g_i^n + g_i^0, \tag{2.4}$$

in which each individual term of the series must satisfy the governing linear elasticity equations within V_A. The functions g_i^0 are associated with prescribed displacements and/or tractions on S_A, whereas the functions g_i^n satisfy homogeneous boundary conditions on S_A. The coefficients C^n are to be linked to the finite-element solution by enforcing, in a weak sense, continuity of displacements and tractions across $S_{A/FE}$. For this purpose the tractions on $S_{A/FE}$ associated with the displacements in (2.4) can be expressed as

$$t_i^A = \sum_n C^n f_i^n + f_i^0. \tag{2.5}$$

Now, weak enforcement of traction continuity across $S_{A/FE}$ is implicit to Equation (2.3), otherwise the term

$$\int_{S_{A/FE}} (t_i^{FE} + t_i^A)\, \delta u_i \, dS = 0, \tag{2.6}$$

would have appeared. Hence, (2.6) is the traction continuity condition, and a weak form of displacement continuity must also be imposed across $S_{A/FE}$.

The procedure proposed by Givoli and co-workers (Givoli and Keller, 1989; Givoli et al., 1992; Givoli and Rivkin, 1993; Keller and Givoli, 1989; Givoli and Keller,

1990; Givoli, 1991; Givoli, 1992;Givoli 1999; Givoli and Vigdergauz, 1994; Givoli et al., 1998) to enforce continuity of displacements is to introduce a Fourier series representation of the displacement on $S_{A/FE}$ and then match the numerical and analytic solutions to this form. This procedure works quite well when the analytic solution itself takes the form of a Fourier series. In other cases, such as in-plane elasticity with branch cuts, this procedure leads to non-symmetric contributions to the finite-element stiffness for a *truncated* series representation of the analytic solution. The weak form of displacement continuity that we are proposing to use leads to symmetric contributions to the finite-element stiffness for any level of truncation to the analytic series solution. The displacement continuity condition is given as

$$\int_{S_{A/FE}} (u_i^{FE} - u_i^A)\, \delta t_i^A \, dS = 0. \tag{2.7}$$

Equation (2.7) will be used to relate the unknown coefficients C^n to the nodal displacements, u_i^J, from the finite-element solution on the boundary $S_{A/FE}$. Note that u_i^{FE} is interpolated from u_i^J through the shape functions N^J as

$$u_i^{FE} = \sum_J N^J u_i^J. \tag{2.8}$$

Applying these interpolations along with (2.4) and (2.5) in (2.7) gives

$$\int_{S_{A/FE}} (\sum_J N^J u_i^J - \sum_n C^n g_i^n - g_i^0)(\sum_m \delta C^m f_i^m)\, dS = 0. \tag{2.9}$$

Rearranging (2.9) and grouping the appropriate terms allows us to define the components of the matrices $[\mathbf{G}]$, $[\mathbf{H}]$, and the vector $[\mathbf{L}]$.

$$\sum_m \sum_n \delta C^m C^n \underbrace{\int_{S_{A/FE}} g_i^n f_i^m \, dS}_{G^{nm}} = \sum_m \sum_J \delta C^m \underbrace{\int_{S_{A/FE}} N^J f_i^m \, dS}_{H^{mJ}} u_i^J + \sum_m \delta C^m \underbrace{\int_{S_{A/FE}} g_i^0 f_i^m \, dS}_{L^m}. \tag{2.10}$$

The proofs that $[\mathbf{G}]$ is symmetric and positive definite are straightforward and relatively trivial. Symmetry is proven by recognizing that g_i^n is a displacement field satisfying the equations of elasticity and f_i^m are the tractions on $S_{A/FE}$ from a second solution. Application of the Rayleigh-Betti reciprocal theorem then demonstrates that the integral on the left-hand side of (2.10) remains the same if *m* and *n* are interchanged. The proof that $[\mathbf{G}]$ is positive definite is performed by recognizing that $\frac{1}{2} C^n G^{nm} C^m$ is the energy stored in V_A for any of the solutions that can be represented by (2.4) and (2.5) in the absence of g_i^0 and f_i^0. Since the stored energy must always be positive in a stable material, $[\mathbf{G}]$ is positive definite for such materials.

Equation (2.10) is valid for arbitrary variations of the C^m coefficients, which then leads to their solution as

$$[\mathbf{G}]\{\mathbf{C}\} = [\mathbf{H}]\{\mathbf{u}^N\} + \{\mathbf{L}\} \quad \rightarrow \quad \{\mathbf{C}\} = [\mathbf{G}]^{-1}[\mathbf{H}]\{\mathbf{u}^N\} + [\mathbf{G}]^{-1}\{\mathbf{L}\}. \tag{2.11}$$

Note that $\{\mathbf{C}\}$ is the vector of unknown coefficients C^n, and $\{\mathbf{u}^N\}$ is the vector of nodal displacements u_i^J, which for (2.11) only contains the nodal quantities on $S_{A/FE}$.

The result from (2.11) can be applied in (2.3). First, we apply the standard finite-element discretization

$$\{\delta\mathbf{u}^N\}^T\{\mathbf{F}^\sigma\} + \sum_n C^n \int_{S_{A/FE}} \sum_J N^J f_i^n \, dS \, \delta u_i^J + \int_{S_{A/FE}} \sum_J N^J f_i^0 \, dS \, \delta u_i^J = \{\delta\mathbf{u}^N\}^T \left\{\mathbf{F}^{FE}\right\}. \tag{2.12}$$

Note that $\{\mathbf{F}^\sigma\}$ is the vector of internal nodal forces associated with the stresses, which may have a non-linear and path-dependent constitutive relationship to the strain history. Next, we apply the result from (2.11) relating the C^n to the u_i^J.

$$\{\delta\mathbf{u}^N\}^T\{\mathbf{F}^\sigma\} + \{\delta\mathbf{u}^N\}^T \underbrace{[\mathbf{H}]^T[\mathbf{G}]^{-1}[\mathbf{H}]}_{[\mathbf{K}^{DtN}]}\{\mathbf{u}^N\} + \{\delta\mathbf{u}^N\}^T \underbrace{[\mathbf{H}]^T[\mathbf{G}]^{-1}\{\mathbf{L}\}}_{\{\mathbf{F}^{DtN}\}} + \{\delta\mathbf{u}^N\}^T\{\mathbf{F}^0\} = \{\delta\mathbf{u}^N\}^T\{\mathbf{F}^{FE}\}. \tag{2.13}$$

Here, we have also defined the stiffness and forces associated with the Dirichlet-to-Neumann map, $[\mathbf{K}^{DtN}]$ and $\{\mathbf{F}^{DtN}\}$. That $[\mathbf{K}^{DtN}]$ is symmetric and positive definite, follows from these same properties of $[\mathbf{G}]$. A standard Newton-Raphson procedure can be used to solve (2.13),

$$\{\delta\mathbf{u}^N\}^T\left[[\mathbf{K}^{FE}] + [\mathbf{K}^{DtN}]\right]\{\Delta\mathbf{u}^N\} = \{\delta\mathbf{u}^N\}^T\left\{\{\mathbf{F}^{FE}\} - \{\mathbf{F}^{DtN}\} - \{\mathbf{F}^0\} - \{\mathbf{F}^{in}\}^{i-1}\right\}, \tag{2.14}$$

where $[\mathbf{K}^{FE}]$ is the standard tangent stiffness matrix for the finite-element region V_{FE}, and

$$\{\mathbf{F}^{in}\}^{i-1} = \{\mathbf{F}^{\sigma}\}^{i-1} + [\mathbf{K}^{DtN}]\{\mathbf{u}^{N}\}^{i-1} \tag{2.15}$$

are the internal forces associated with both the finite-element region and the Dirichlet-to-Neumann map from the prior Newton-Raphson iteration. The vector $\{\Delta\mathbf{u}^{N}\}$ contains the nodal displacement corrections such that

$$\{\mathbf{u}^{N}\}^{i} = \{\mathbf{u}^{N}\}^{i-1} + \{\Delta\mathbf{u}^{N}\}. \tag{2.16}$$

Finally, this equation is valid for arbitrary variations of the nodal displacements, leading to the final system of equations to be solved,

$$\left[[\mathbf{K}^{FE}] + [\mathbf{K}^{DtN}]\right]\{\Delta\mathbf{u}^{N}\} = \{\mathbf{F}^{FE}\} - \{\mathbf{F}^{0}\} - \{\mathbf{F}^{DtN}\} - \{\mathbf{F}^{in}\}^{i-1}, \tag{2.17}$$

concluding the general method for coupling a domain with an analytic solution represented by a truncated series to a finite-element domain. Note that while linearity has been assumed in the analytic region, no assumptions or restrictions associated with isotropy or homogeneity in this region have been made. The primary complications of the method arise from the generation of the analytic solution, and then the evaluation of the integrals in Equation (2.10). In the following sections we will discuss how these issues are addressed for crack problems in homogeneous isotropic regions, and present sets of results that can be obtained from the method.

2.2 INTERIOR MAP

The first class of problems that can be studied with the coupled analytic/finite-element method is on the determination of the linear elastic fracture mechanics parameters in an arbitrarily shaped and loaded specimen. As mentioned above, in this case, the analytic solution is used to represent the linear elastic field within a circular region around the crack tip, with traction free crack faces on $r < R$. The finite-element method is implemented for the remainder of the body, i.e., V_{FE} contains the points on $r \geq R$. The crack faces must be traction free on $r < R$, not necessarily on $r \geq R$. Note that the region being analyzed with finite-elements need not be restricted to homogeneous linear elastic behavior.

The analytic solution in the vicinity of the crack tip is represented by all of the terms in the Williams expansion (1957), that yield non-singular displacements at the crack tip. The specific forms of the displacements are given as

$$\begin{aligned} 2\mu u_x = & \sum_{n=3}^{\infty} A_n r^{n/2} \left[\left(\kappa + (-1)^n + \tfrac{n}{2} \right) \cos\left(\tfrac{n\theta}{2} \right) - \tfrac{n}{2} \cos\left(\tfrac{(4-n)\theta}{2} \right) \right] \\ & + K_{\mathrm{I}} \sqrt{\frac{r}{2\pi}} \left[\left(\kappa - \tfrac{1}{2} \right) \cos\left(\tfrac{\theta}{2} \right) - \tfrac{1}{2} \cos\left(\tfrac{3\theta}{2} \right) \right] \\ & + \sum_{n=3}^{\infty} B_n r^{n/2} \left[\left(\kappa - (-1)^n + \tfrac{n}{2} \right) \sin\left(\tfrac{n\theta}{2} \right) + \tfrac{n}{2} \sin\left(\tfrac{(4-n)\theta}{2} \right) \right] \\ & + K_{\mathrm{II}} \sqrt{\frac{r}{2\pi}} \left[\left(\kappa + \tfrac{3}{2} \right) \sin\left(\tfrac{\theta}{2} \right) + \tfrac{1}{2} \sin\left(\tfrac{3\theta}{2} \right) \right] \\ & + \frac{T}{4} \left(\kappa + 1 \right) r \cos\theta, \end{aligned} \tag{2.18}$$

$$
\begin{aligned}
2\mu u_y = &\sum_{n=3}^{\infty} A_n r^{n/2}\left[\left(\kappa-(-1)^n-\tfrac{n}{2}\right)\sin\left(\tfrac{n\theta}{2}\right)-\tfrac{n}{2}\sin\left(\tfrac{(4-n)\theta}{2}\right)\right]\\
&+K_{\mathrm{I}}\sqrt{\frac{r}{2\pi}}\left[\left(\kappa+\tfrac{1}{2}\right)\sin\left(\tfrac{\theta}{2}\right)-\tfrac{1}{2}\sin\left(\tfrac{3\theta}{2}\right)\right]\\
&+\sum_{n=3}^{\infty} B_n r^{n/2}\left[\left(-\kappa-(-1)^n+\tfrac{n}{2}\right)\cos\left(\tfrac{n\theta}{2}\right)-\tfrac{n}{2}\cos\left(\tfrac{(4-n)\theta}{2}\right)\right]\\
&+K_{\mathrm{II}}\sqrt{\frac{r}{2\pi}}\left[\left(-\kappa+\tfrac{3}{2}\right)\cos\left(\tfrac{\theta}{2}\right)-\tfrac{1}{2}\cos\left(\tfrac{3\theta}{2}\right)\right]\\
&+\frac{T}{4}\left(\kappa-3\right)r\sin\theta,
\end{aligned}
\tag{2.19}
$$

The corresponding tractions are then given as

$$
\begin{aligned}
t_x = &\sum_{n=3}^{\infty} A_n r^{-1+n/2}\,\tfrac{n}{2}\left[\left(\tfrac{n}{2}+1+(-1)^n\right)\cos\left(\tfrac{n\theta}{2}\right)+\tfrac{4-n}{2}\cos\left(\tfrac{(4-n)\theta}{2}\right)\right]\\
&+\frac{K_{\mathrm{I}}}{\sqrt{2\pi r}}\left[\tfrac{1}{4}\cos\left(\tfrac{\theta}{2}\right)+\tfrac{3}{4}\cos\left(\tfrac{3\theta}{2}\right)\right]\\
&+\sum_{n=3}^{\infty} B_n r^{-1+n/2}\,\tfrac{n}{2}\left[\left(\tfrac{n}{2}+1-(-1)^n\right)\sin\left(\tfrac{n\theta}{2}\right)-\tfrac{4-n}{2}\sin\left(\tfrac{(4-n)\theta}{2}\right)\right]\\
&+\frac{K_{\mathrm{II}}}{\sqrt{2\pi r}}\left[\tfrac{5}{4}\sin\left(\tfrac{\theta}{2}\right)-\tfrac{3}{4}\sin\left(\tfrac{3\theta}{2}\right)\right]+T\cos\theta,
\end{aligned}
\tag{2.20}
$$

$$
\begin{aligned}
t_y = &\sum_{n=3}^{\infty} A_n r^{-1+n/2}\,\tfrac{n}{2}\left[\left(-\tfrac{n}{2}+1-(-1)^n\right)\sin\left(\tfrac{n\theta}{2}\right)+\tfrac{4-n}{2}\sin\left(\tfrac{(4-n)\theta}{2}\right)\right]\\
&+\frac{K_{\mathrm{I}}}{\sqrt{2\pi r}}\left[\tfrac{3}{4}\sin\left(\tfrac{\theta}{2}\right)+\tfrac{3}{4}\sin\left(\tfrac{3\theta}{2}\right)\right]\\
&+\sum_{n=3}^{\infty} B_n r^{-1+n/2}\,\tfrac{n}{2}\left[\left(\tfrac{n}{2}-1-(-1)^n\right)\cos\left(\tfrac{n\theta}{2}\right)+\tfrac{4-n}{2}\cos\left(\tfrac{(4-n)\theta}{2}\right)\right]\\
&+\frac{K_{\mathrm{II}}}{\sqrt{2\pi r}}\left[\tfrac{1}{4}\cos\left(\tfrac{\theta}{2}\right)+\tfrac{3}{4}\cos\left(\tfrac{3\theta}{2}\right)\right].
\end{aligned}
\tag{2.21}
$$

In Equations (2.18)-(2.21), μ is the shear modulus, $2\mu = E/(1+\nu)$, and $\kappa = 3-4\nu$ for plane strain or $(3-\nu)/(1+\nu)$ for plane stress. Here the unknown A_n and B_n coefficients are equivalent to the C^n coefficients of Equations (2.5) and (2.6), the functions that they pre-multiply are the f_i^n and g_i^n. With all of these functions explicitly defined, the integrals in (2.10) can be determined analytically with one caveat. In general the shape functions N^J are polynomial functions of the Cartesian coordinates, and do not represent a circular arc exactly. However, in order to evaluate the integrals in (2.10) analytically, the approximation that the N^J can be used to interpolate the angular position along the arc $S_{A/FE}$ is made. For example, for standard 4-noded isoparametric elements the approximations for the shape functions along the boundary would be $N^I = (\theta_J - \theta)/(\theta_J - \theta_I)$ and $N^J = (\theta - \theta_I)/(\theta_J - \theta_I)$, where I and J are the node numbers and θ_I and θ_J are the angular positions along the arc for nodes *I* and *J*.

The tractions from (2.20) and (2.21) are those on a circular boundary of radius *r*, with unit normal pointing away from the origin. Here we emphasize that the fracture parameters of interest, K_{I}, K_{II}, and *T*, are *unknown* quantities that must be determined from the calculation. We will see that this is in contrast to the exterior map, where K_{I}, K_{II}, and *T* were the known amplitudes of the far field loading conditions. Effectively, we have extracted the terms associated with $A_1 = K_{\mathrm{I}}/\sqrt{2\pi}$, $A_2 = T/4$, $B_1 = K_{\mathrm{II}}/\sqrt{2\pi}$, and $B_2 = 0$ from the infinite series in order to explicitly relate these coefficients to the linear elastic fracture mechanics parameters. Note that the B_2 term leads to a rigid body rotation and does not contribute to the DtN stiffnesses or forces. Next, the functions of Equations (2.18)-(2.21) are fed into (2.10) to determine the [**G**] and [**H**] matrices (note that $\{\mathbf{L}\} = \mathbf{0}$ in this case). After the finite-element solution is obtained it is necessary to perform a post-processing step, specifically the calculation of the coefficients via (2.11), in order to recover the stress intensity factors, K_{I} and K_{II}, and the *T*-stress.

2.2.1 Infinite Plate with Center Crack - Accuracy of the Method with Truncation Number

In order to demonstrate the accuracy and convergence of the method we first compare the method to an analytic solution. The problem studied is an infinite plate with a finite crack of length $2a$ on the x-axis along $\left|x\right| < a$. The plate is loaded by remote axial stresses $\sigma_{yy}^{\infty} = \sigma$ and $\sigma_{xx}^{\infty} = \sigma + T_{xx}$ and a remote shear stress $\sigma_{xy}^{\infty} = \tau$. For this problem the stress intensity factors and the T-stress are

$$K_{\mathrm{I}} = \sigma\sqrt{\pi a}\ , K_{\mathrm{II}} = \tau\sqrt{\pi a} \text{ and } T = T_{xx}\,. \tag{2.22}$$

The displacement fields can be obtained from the Westergaard stress functions as

$$\hat{Z}_{\mathrm{I}} = \sigma\sqrt{z^2 - a^2} \text{ and } \hat{Z}_{\mathrm{II}} = \tau\sqrt{z^2 - a^2} \tag{2.23}$$

where $z = x + iy$. The displacements induced by the uniform T-stress are then given as

$$\begin{aligned} 2\mu u_x = {} & \tfrac{1}{2}\left(\kappa - 1\right)\mathrm{Re}\,\hat{Z}_{\mathrm{I}} - y\,\mathrm{Im}\,\hat{Z}'_{\mathrm{I}} + \tfrac{1}{2}\left(\kappa + 1\right)\mathrm{Im}\,\hat{Z}_{\mathrm{II}} \\ & + y\,\mathrm{Re}\,\hat{Z}'_{\mathrm{II}} + \tfrac{1}{4}T_{xx}\left(\kappa + 1\right)r\cos\theta, \end{aligned} \tag{2.24}$$

$$\begin{aligned} 2\mu u_y = {} & \tfrac{1}{2}\left(\kappa + 1\right)\mathrm{Im}\,\hat{Z}_{\mathrm{I}} - y\,\mathrm{Re}\,\hat{Z}'_{\mathrm{I}} - \tfrac{1}{2}\left(\kappa - 1\right)\mathrm{Re}\,\hat{Z}_{\mathrm{II}} \\ & - y\,\mathrm{Im}\,\hat{Z}'_{\mathrm{II}} + \tfrac{1}{4}T_{xx}\left(\kappa - 3\right)r\sin\theta. \end{aligned} \tag{2.25}$$

In order to compare the numerical method to this analytic solution, which is valid for an infinite plate, we consider only the circular region around the right crack tip

defined by $\sqrt{(x-a)^2+y^2} \le a$. The inner circular region $\sqrt{(x-a)^2+y^2} \le a/2$ is represented by the interior DtN map, and the annulus $a/2 < \sqrt{(x-a)^2+y^2} \le a$ is analyzed with 9-noded isoparametric finite-elements, as shown in Figure 2.2.1. The annulus is discretized by a uniform structured mesh with 24, 48, or 96 elements around the arc and 5 or 10 elements along the radial direction. On the outer boundary, $\sqrt{(x-a)^2+y^2} = a$, the displacements from the analytic solution, (2.24) and (2.25), are imposed. The purpose of this study is to investigate the effect that the level of truncation, $N_{\text{truncation}}$, has on the accuracy of the determination of the fracture mechanics parameters.

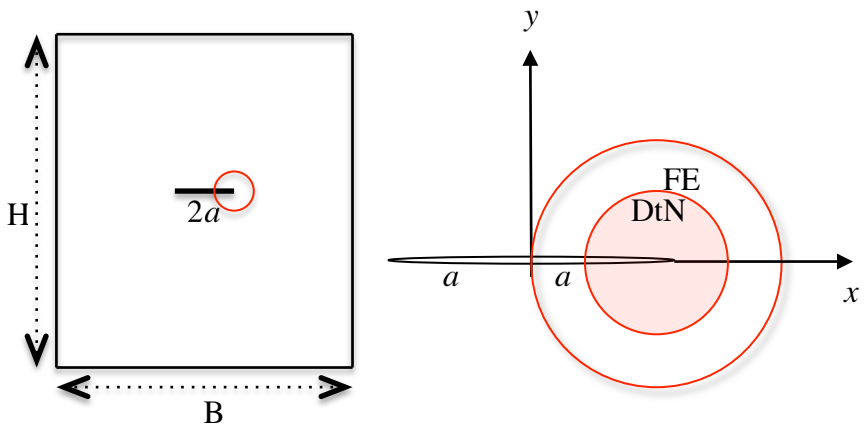

Figure 2.2.1 Schematic of an infinite plate with, ($H, B \to \infty$), with a center crack. The red circle, blown up on the right of the Figure shows the regions represented by the FE method and the interior map. The plate is loaded with the remote stresses $\sigma^{\infty}_{yy} = \sigma$, $\sigma^{\infty}_{xx} = \sigma + T_{xx}$ and $\sigma^{\infty}_{xy} = \tau$.

Figure 2.2.2 plots the error in the mode I stress intensity factor computed using the interior DtN map as a function of the level of truncation for the infinite series in Equations (2.18)-(2.21). Specifically, both the A_n and the B_n series are truncated at

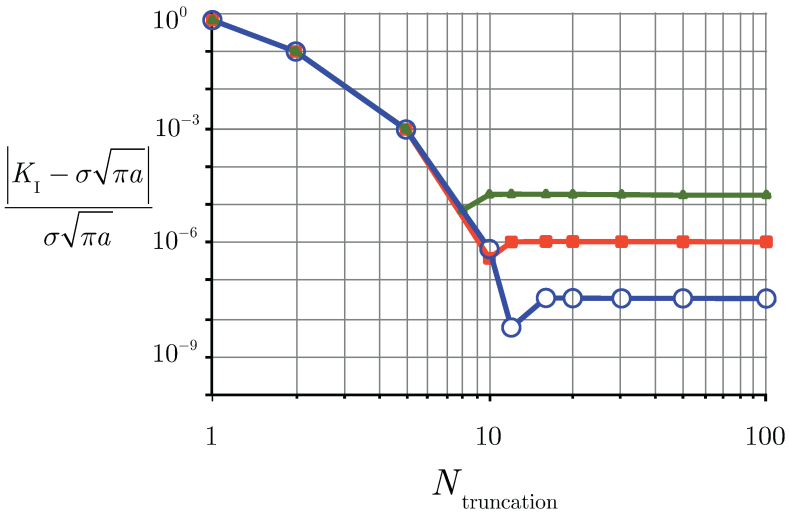

Figure 2.2.2 The error in the calculated mode I stress intensity factor K_{I} as a function of the level of truncation in the DtN map for three different finite-element meshes in the annulus surrounding the map. Green triangles, red squares and blue circles are for 24, 48 and 96 element divisions along the arc. The results using either 5 or 10 element divisions along the radial direction are indistinguishable from one another. The error in the mode II stress intensity factor is very similar to this plot. The *T*-stress also follows the initial curve for $N_{\text{truncation}} < 10$ very closely, but the plateau levels for the error in T are approximately an order of magnitude lower than those for K_{I} and K_{II}.

$N_{\text{truncation}}$. The three curves correspond to different finite-element meshes in the annulus surrounding the DtN map, with green triangles, red squares and blue circles representing 24, 48 and 96 element divisions along the arc. Note that the results for the error using either 5 or 10 element divisions along the radial direction for each of the angular discretization are indistinguishable from one another. What is evident in Figure 2.2.2 is that the accuracy of the DtN map controls the level of the error when $N_{\text{truncation}}$ is low, and the finite-element discretization controls the error for large $N_{\text{truncation}}$. For a given finite-element mesh and a given boundary value problem, there is a level of $N_{\text{truncation}}$

beyond which no additional accuracy can be gained by the method because the errors introduced by the finite-element discretization dominate.

Note that the error values reported in Figure 2.2.2 are problem specific and sensitive to the ratio of the DtN map radius to the crack half-length, which in this case is one half. In every fracture mechanics problem there is a characteristic length scale associated with the geometry and/or loading of the specimen. As the radius of the DtN region is reduced with respect to this length scale, the accuracy associated with each level of $N_{\text{truncation}}$ is improved. However, a benefit of the DtN map is that it can be used to accurately represent the solution in a region that is as large as possible. Furthermore, from a practical standpoint, the stiffness and force contributions from the DtN map for $N_{\text{truncation}}$ in the thousands can be computed rapidly, which in turn will leave the accuracy in the determination of K_{I}, K_{II}, and T to be controlled by the finite-element discretization for most boundary value problems of interest. Finally, we note that the error in the mode II stress intensity factor is very similar to the error in K_{I} shown in Figure 2.2.2 for each case. The error in the *T*-stress also follows the initial part of the curve in Figure 2.2.2 for $N_{\text{truncation}} < 10$ very closely, but the plateau levels for the error in *T* are approximately an order of magnitude lower than those for K_{I} and K_{II}.

2.2.2 Single-Edge Notched Tensile Specimen – Stress Intensity Factor Determination

To further demonstrate the method we solve for the mode I stress intensity factor and the *T*-stress for a single-edge notched tensile (SENT) specimen. Due to symmetry conditions, only the top half of the specimen geometry is analyzed. The coarsest finite-element mesh (264 elements) and the parameters of the specimen geometry, including the crack length *a*, specimen width *w*, and half-height *h*, are illustrated in Figure 2.2.3. The

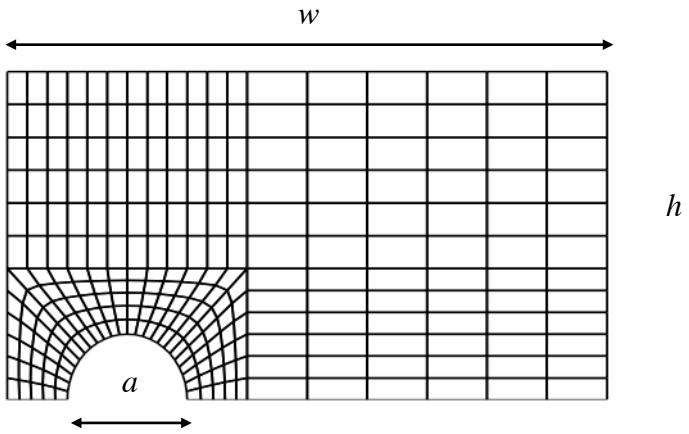

Figure 2.2.3. The finite-element mesh with 264 elements for the single-edge notched tensile specimen. Due to symmetry conditions only the top half of the specimen needs to be analyzed. The circular region around the crack tip is analyzed with the DtN map. A uniform tensile traction σ is applied along the top boundary.

circular region around the crack tip is modeled with the interior DtN map. The loading of the specimen consists of a uniform tensile traction σ applied in the vertical direction along the top boundary. The mesh displayed in Figure 2.2.3 has 24 element divisions along the arc shared by the DtN map. We have also analyzed meshes with 48 and 96 divisions along the arc, corresponding to 4 and 16 times as many elements as the mesh in Figure 2.2.3. The results for K_{I} and T for several specimen geometries are reported in Table 1. The computed values have converged to the number of significant figures shown in Table 1 for all cases, and these values can be obtained from the coarsest mesh studied.

a / w	$K_{\mathrm{I}} / \sigma\sqrt{\pi a}$	T / σ
0.2	1.487 (1.483)	-0.521 (-0.516)
0.3	1.848 (1.841)	-0.301 (-0.295)

0.4	2.324 (2.309)	0.110 (0.114)
0.5	3.009 (3.033)	0.667 (0.673)
0.6	4.149 (4.092)	1.375 (1.386)

$h / w = 1$

a / w	$K_{\mathrm{I}} / \sigma\sqrt{\pi a}$	T / σ
0.2	1.368 (1.380)	-0.589 (-0.583)
0.3	1.661 (1.676)	-0.607 (-0.605)
0.4	2.113 (2.134)	-0.571 (-0.567)
0.5	2.825 (2.858)	-0.410 (-0.405)
0.6	4.033 (4.090)	0.050 (0.057)

Table 2.2.1 Results for K_{I} and T for the SENT specimen geometry shown in Figure 2.2.3. The results in parentheses are due to Yang and Ravi-Chandar (Yang and Ravi-Chandar, 1999).

2.3 EXTERIOR MAP

As previously discussed, the exterior map can be used to investigate problems of planar semi-infinite cracks. The crack tip lies at the origin and the crack flanks are on the negative *x*-axis. At sufficiently remote distances from the crack tip the fields are governed by linear elasticity such that the stresses are dominated by the combined *K*-*T* field given as

$$\begin{Bmatrix}\sigma_{xx}\\ \sigma_{yy}\\ \sigma_{xy}\end{Bmatrix} = \frac{K_{\mathrm{I}}}{\sqrt{2\pi r}}\cos\tfrac{\theta}{2}\begin{Bmatrix}1-\sin\tfrac{\theta}{2}\sin\tfrac{3\theta}{2}\\ 1+\sin\tfrac{\theta}{2}\sin\tfrac{3\theta}{2}\\ \sin\tfrac{\theta}{2}\cos\tfrac{3\theta}{2}\end{Bmatrix} + \frac{K_{\mathrm{II}}}{\sqrt{2\pi r}}\begin{Bmatrix}\sin\tfrac{\theta}{2}(-2+\cos\tfrac{\theta}{2}\cos\tfrac{3\theta}{2})\\ \sin\tfrac{\theta}{2}\cos\tfrac{\theta}{2}\cos\tfrac{3\theta}{2}\\ \cos\tfrac{\theta}{2}(1-\sin\tfrac{\theta}{2}\sin\tfrac{3\theta}{2})\end{Bmatrix} + \begin{Bmatrix}T\\ 0\\ 0\end{Bmatrix}. \tag{2.26}$$

Close to the crack tip we allow for a wide range of situations that are not amenable to analytic solution techniques but can be handled with the finite-element method. Such problems include geometric features like voids or inhomogeneities around the crack, prescribed loading of the crack faces or the material near the crack tip, and perhaps most interestingly plasticity or some other non-linear constitutive response near the crack tip. In all of these cases we must identify a radial distance from the crack tip, R, that surrounds all such features. For $r > R$ the domain is a homogeneous isotropic elastic region with Young's modulus *E* and Poisson's ratio ν. The crack faces must be traction free on $r > R$, but not necessarily on $r \le R$. In relation to Equation (2.2), V_A consists of all points satisfying $r > R$, and V_{FE} contains the points $r < R$. We now need a series representation of the solution in the analytic domain that satisfies the remote loading conditions of (2.26) and the traction-free crack face boundary conditions. This solution contains the standard *K* and *T* terms along with all of the terms from the Williams expansion (Williams, 1957) containing non-singular stresses as $r \to \infty$.

$$
\begin{aligned}
2\mu u_x^A = & \sum_{n=1}^{\infty} A_n r^{-n/2}\left[\left(\kappa + (-1)^n - \tfrac{n}{2}\right)\cos\left(\tfrac{n\theta}{2}\right) + \tfrac{n}{2}\cos\left(\tfrac{(n+4)\theta}{2}\right)\right] \\
& + K_{\mathrm{I}}\sqrt{\frac{r}{2\pi}}\left[\left(\kappa - \tfrac{1}{2}\right)\cos\left(\tfrac{\theta}{2}\right) - \tfrac{1}{2}\cos\left(\tfrac{3\theta}{2}\right)\right] \\
& + \sum_{n=1}^{\infty} B_n r^{-n/2}\left[\left(-\kappa + (-1)^n + \tfrac{n}{2}\right)\sin\left(\tfrac{n\theta}{2}\right) - \tfrac{n}{2}\sin\left(\tfrac{(n+4)\theta}{2}\right)\right] \\
& + K_{\mathrm{II}}\sqrt{\frac{r}{2\pi}}\left[\left(\kappa + \tfrac{3}{2}\right)\sin\left(\tfrac{\theta}{2}\right) + \tfrac{1}{2}\sin\left(\tfrac{3\theta}{2}\right)\right] \\
& + \frac{T}{4}\left(\kappa + 1\right) r\cos\theta,
\end{aligned}
\tag{2.27}
$$

$$
\begin{aligned}
2\mu u_y^A = &\sum_{n=1}^{\infty} A_n r^{-n/2}\left[\left(-\kappa+(-1)^n-\tfrac{n}{2}\right)\sin\left(\tfrac{n\theta}{2}\right)+\tfrac{n}{2}\sin\left(\tfrac{(n+4)\theta}{2}\right)\right]\\
&+K_{\mathrm{I}}\sqrt{\frac{r}{2\pi}}\left[\left(\kappa+\tfrac{1}{2}\right)\sin\left(\tfrac{\theta}{2}\right)-\tfrac{1}{2}\sin\left(\tfrac{3\theta}{2}\right)\right]\\
&+\sum_{n=1}^{\infty} B_n r^{-n/2}\left[\left(-\kappa-(-1)^n-\tfrac{n}{2}\right)\cos\left(\tfrac{n\theta}{2}\right)+\tfrac{n}{2}\cos\left(\tfrac{(n+4)\theta}{2}\right)\right]\\
&+K_{\mathrm{II}}\sqrt{\frac{r}{2\pi}}\left[\left(-\kappa+\tfrac{3}{2}\right)\cos\left(\tfrac{\theta}{2}\right)-\tfrac{1}{2}\cos\left(\tfrac{3\theta}{2}\right)\right]\\
&+\frac{T}{4}\left(\kappa-3\right)r\sin\theta,
\end{aligned}
\tag{2.28}
$$

$$
\begin{aligned}
t_x^A = &-\sum_{n=1}^{\infty} A_n r^{-1-n/2}\,\tfrac{n}{2}\left[\left(\tfrac{n}{2}-1-(-1)^n\right)\cos\left(\tfrac{n\theta}{2}\right)-\tfrac{n+4}{2}\cos\left(\tfrac{(n+4)\theta}{2}\right)\right]\\
&-\frac{K_{\mathrm{I}}}{\sqrt{2\pi r}}\left[\tfrac{1}{4}\cos\left(\tfrac{\theta}{2}\right)+\tfrac{3}{4}\cos\left(\tfrac{3\theta}{2}\right)\right]\\
&-\sum_{n=1}^{\infty} B_n r^{-1-n/2}\,\tfrac{n}{2}\left[\left(-\tfrac{n}{2}+1-(-1)^n\right)\sin\left(\tfrac{n\theta}{2}\right)+\tfrac{n+4}{2}\sin\left(\tfrac{(n+4)\theta}{2}\right)\right]\\
&-\frac{K_{\mathrm{II}}}{\sqrt{2\pi r}}\left[\tfrac{5}{4}\sin\left(\tfrac{\theta}{2}\right)-\tfrac{3}{4}\sin\left(\tfrac{3\theta}{2}\right)\right]-T\cos\theta,
\end{aligned}
\tag{2.29}
$$

$$
\begin{aligned}
t_y^A = &-\sum_{n=1}^{\infty} A_n r^{-1-n/2}\,\tfrac{n}{2}\left[\left(\tfrac{n}{2}+1-(-1)^n\right)\sin\left(\tfrac{n\theta}{2}\right)-\tfrac{n+4}{2}\sin\left(\tfrac{(n+4)\theta}{2}\right)\right]\\
&-\frac{K_{\mathrm{I}}}{\sqrt{2\pi r}}\left[\tfrac{3}{4}\sin\left(\tfrac{\theta}{2}\right)+\tfrac{3}{4}\sin\left(\tfrac{3\theta}{2}\right)\right]\\
&-\sum_{n=1}^{\infty} B_n r^{-1-n/2}\,\tfrac{n}{2}\left[\left(\tfrac{n}{2}+1+(-1)^n\right)\cos\left(\tfrac{n\theta}{2}\right)-\tfrac{n+4}{2}\cos\left(\tfrac{(n+4)\theta}{2}\right)\right]\\
&-\frac{K_{\mathrm{II}}}{\sqrt{2\pi r}}\left[\tfrac{1}{4}\cos\left(\tfrac{\theta}{2}\right)+\tfrac{3}{4}\cos\left(\tfrac{3\theta}{2}\right)\right].
\end{aligned}
\tag{2.30}
$$

Here the unknown A_n and B_n coefficients are equivalent to the C^n coefficients of Equations (2.5) and (2.6), the functions that they pre-multiply are the f_i^n and g_i^n as in the case of the interior map. The known in this case loading terms associated with K_{I}, K_{II}, and T are the f_i^0 and g_i^0 functions. Note that the tractions from (2.29) and (2.30) are

those on a circular boundary of radius r, with unit normal pointing towards the origin. Then, the integrals in (2.12) can be determined analytically as described above for the interior map.

2.3.1 Semi-Infinite Crack Terminating in an Inclusion – Combination of the Interior and Exterior Map

Before proceeding to the application of the exterior map to the small-scale yielding problem, we analyze the problem of a semi-infinite crack terminating in a circular inclusion of radius R by combining both the interior and exterior DtN maps. In this case, no finite-element mesh is needed at all aside from a discretization of the circular boundary shared by the inclusion and the matrix. In general the DtN maps can be thought of as super-elements for the region that they represent. The interior DtN map is a super-element for a circular disk containing a straight crack terminating at its center. The exterior map is a super-element for an infinite region with a circular cutout around the origin and a semi-infinite crack. In either case the super-element stiffness is a fully dense matrix with interactions between each nodal degree of freedom along the discretized circular boundary. For the crack terminating in the inclusion the exterior DtN map associated with the discretization of the inclusion boundary is used to create the far-field loading and stiffness contributions for the matrix material, and the internal map associated with the same boundary nodes is used to create the stiffness contributions for the inclusion.

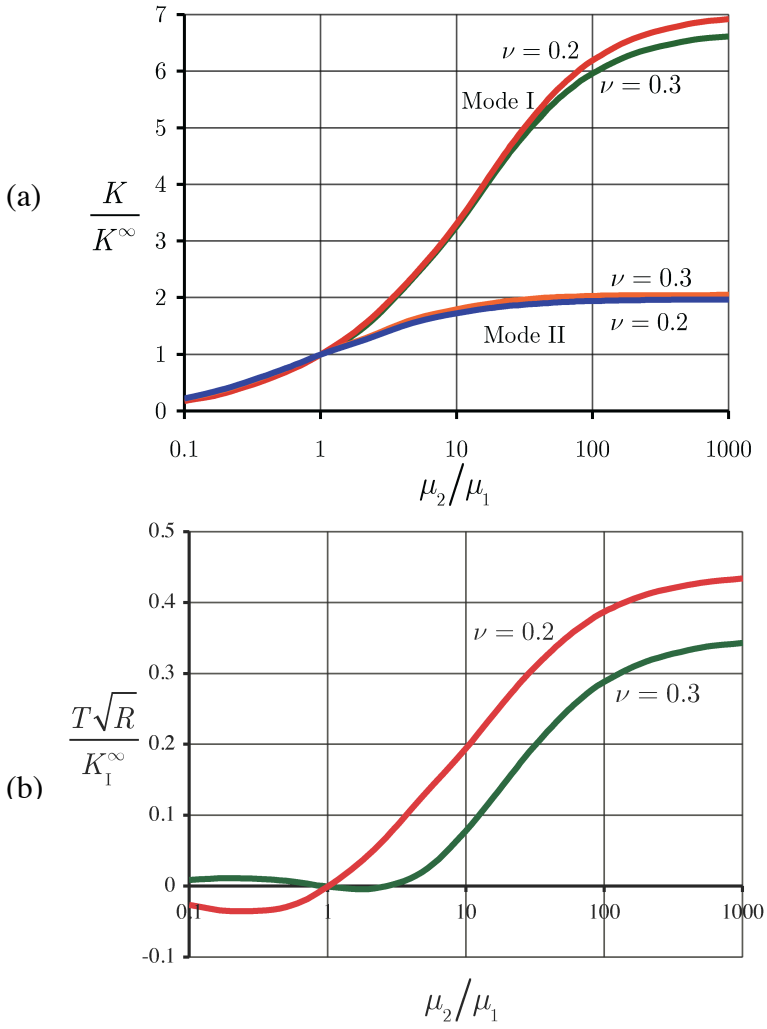

Figure 2.3.1. (a) The mode I and mode II crack-tip stress intensity factors for a semi-infinite crack terminating in the center of a circular inclusion (material 1) of radius *R* with far-field loading in the surrounding matrix material (material 2) characterized by either pure mode I or pure mode II. Curves are plotted as a function of the shear modulus ratio for two values of Poisson's ratio, which is assumed to be equal in both phases. (b) The *T*-stress induced within the inclusion for pure mode I loading. Due to symmetry, no *T*-stress is induced for mode II loading.

The matrix material with shear modulus, μ_1, and Poisson's ratio, ν_1, occupies the region $r > R$, and is loaded in the far-field as described by Equation (2.26). The

inclusion with shear modulus, μ_2, and Poisson's ratio, ν_2, occupies the region $r \le R$, and contains the crack tip which is located at $r = 0$. This problem can be studied over the full range of Dundurs parameters (1969), as has been done by Steif (1987) and Wang and Ballarini (2003). Here we demonstrate the DtN map method for a wide range of shear modulus ratios and two values for the Poisson's ratios with $\nu_1 = \nu_2 = \nu$. The results for pure mode I loading, are in excellent agreement with Steif's results. Specifically, for $\nu_1 = \nu_2 = 0.2$, and $\mu_2 / \mu_1 = 0.1$ our result for $K_{\mathrm{I}} / K_{\mathrm{I}}^{\infty}$ is 0.17804, and Steif's result is 0.17806 (which appears to be converging from above). Figure 2.3.1a plots the ratio of the crack-tip stress intensity factor in the inclusion to the far-field stress intensity factor applied to the matrix for either pure mode I, K_{I}^{∞}, or pure mode II, K_{II}^{∞}, loading. Interestingly, the magnification of the stress intensity factor by a stiff inclusion is significantly larger in mode I than in mode II. Figure 2.3.1b plots the *T*-stress that develops in the inclusion during pure mode I loading of the matrix. Note that due to symmetry, no *T*-stress develops in the inclusion for pure mode II loading of the matrix.

2.4 EXTERIOR MAP – THE SMALL SCALE YIELDING PROBLEM

A semi-infinite crack, with crack flanks along the negative x-axis and crack tip located at the origin is studied numerically, within the context of the small scale yielding boundary layer approach as described by Rice (1968a, 1968b, 1974), employing the exterior Dirichlet-to-Neumann map. Details of the crack tip field for a stationary crack in elastic plastic material that have been computed previously by others, including the existence of an elastic sector in mode I loading, are confirmed.

The path-dependence of the J-integral is investigated numerically, via the finite element method, for a range of loadings, Poisson's ratios, and hardening exponents within the context of J_2-flow plasticity. The somewhat unexpected result is that J for a contour

approaching zero radius around the crack tip is approximately 18% lower than the far-field value for Mode I loading for Poisson's ratios characteristic of metals. In contrast, practically no path-dependence is found for mode II. The applications of T- or S-stresses, whether applied proportionally with the K-field or prior to K, have only a modest effect on the path-dependence.

2.4.1 Problem Description and Constitutive Response of the Material

Material with a power-law hardening constitutive response as described by Rice and Rosengren (1968) are studied such that the uniaxial stress-strain behavior is described by

$$\frac{\sigma}{\sigma_0} = \frac{\varepsilon}{\varepsilon_0} \text{ for } \varepsilon \le \varepsilon_0 \tag{2.31}$$

and

$$\frac{\sigma}{\sigma_0} = \left(\frac{\varepsilon}{\varepsilon_0}\right)^N \text{ for } \varepsilon > \varepsilon_0. \tag{2.32}$$

The initial yield strength is σ_0, and the uniaxial strain at initial yield is ε_0. These material parameters are related through the Young's modulus, E, as $\sigma_0 = E\varepsilon_0$. The strain-hardening exponent is N, with $N = 0$ representing perfect plasticity and $N = 1$ linear elasticity. The J_2-flow theory of plasticity is used for the multi-axial generalization of the material constitutive response such that the increments of the Cartesian stress tensor components, $d\sigma_{ij}$, are given as

$$d\sigma_{ij} = \frac{E\nu}{(1+\nu)(1-2\nu)} d\varepsilon_{kk}\delta_{ij} + \frac{E}{(1+\nu)}\left(d\varepsilon_{ij} - d\varepsilon_{ij}^{p}\right) \tag{2.33}$$

Here, the Poisson's ratio is ν and δ_{ij} is the Kronecker delta, and the Cartesian components of the total strain and plastic strain increments are $d\varepsilon_{ij}$ and $d\varepsilon_{ij}^{p}$. Within the context of J_2-flow theory, the plastic strain increments are proportional to the stress deviator components, $s_{ij} = \sigma_{ij} - \sigma_{kk}\delta_{ij}/3$,

$$d\varepsilon_{ij}^{p} = \frac{3}{2}\frac{d\bar{\varepsilon}^{p}}{\bar{\sigma}} s_{ij}, \tag{2.34}$$

where the effective uniaxial stress is $\bar{\sigma} = \sqrt{\frac{3}{2} s_{ij} s_{ij}}$, and the effective uniaxial strain increment is $d\bar{\varepsilon}^{p} = \sqrt{\frac{2}{3} d\varepsilon_{ij}^{p} d\varepsilon_{ij}^{p}}$. During continued plastic deformation the stress state is constrained to reside on the yield surface given by

$$\frac{3}{2} s_{ij} s_{ij} = \sigma_y^2 \tag{2.35}$$

The current level of the yield strength, σ_y, satisfies the following nonlinear equation in order to be consistent with the uniaxial behavior described by Equation (2.1),

$$\frac{\bar{\varepsilon}^{p}}{\varepsilon_0} = \left(\frac{\sigma_y}{\sigma_0}\right)^{1/N} - \frac{\sigma_y}{\sigma_0} \tag{2.36}$$

where the total effective plastic strain is simply the sum of all increments, $\bar{\varepsilon}^{p} = \int d\bar{\varepsilon}^{p}$, throughout the history of loading.

Deformation theory of plasticity is also employed for comparison when necessary. In this case the stresses are derived from the strain energy density as,

$\sigma_{ij} = \partial W / \partial \varepsilon_{ij}$. An example of strain energy density, W, for elastic-perfectly plastic materials described by deformation theory is given as

$$W = \begin{cases} \mu e_{ij} e_{ij} + \dfrac{E}{6(1-2\nu)} \varepsilon_{mm} \varepsilon_{nn} & \text{if} \quad 6\mu^2 e_{ij} e_{ij} \le \sigma_0^2 \\ \sigma_0 \sqrt{\frac{2}{3} e_{ij} e_{ij}} + \dfrac{E}{6(1-2\nu)} \varepsilon_{mm} \varepsilon_{nn} - \dfrac{\sigma_0^2}{6\mu} & \text{if} \quad 6\mu^2 e_{ij} e_{ij} > \sigma_0^2 \end{cases} \tag{2.37}$$

The yield strength σ_0 has been introduced, and e_{ij} are the components of the deviatoric strain, $e_{ij} = \varepsilon_{ij} - \delta_{ij} \varepsilon_{kk} / 3$. The solution to this problem is characterized by the development and self-similar growth of a plastic zone around the crack tip. Note that self-similar growth of the plastic zone only occurs if the mode I and mode II stress intensity factors are applied proportionally. At sufficiently remote distances from the crack tip, the fields are governed by linear elasticity and the stresses approach the combined $K-T$ field given in the previous section by Equation (2.26).

In the out-of-plane direction generalized plane strain is imposed such that the out-of-plane axial strain is constant throughout the domain and given by

$$\varepsilon_{zz} = \frac{1}{E}(S - \nu T) \tag{2.38}$$

with S as the far field out-of-plane axial stress σ_{zz}.

Neglecting the S- and T-stresses, the characteristic size of the plastic zone around the crack tip is approximated as,

$$R_p = \frac{1}{3\pi}\frac{K_{\mathrm{I}}^2 + \frac{25}{4}K_{\mathrm{II}}^2}{\sigma_0^2} \tag{2.39}$$

Using this mixed-mode definition of the plastic zone size, the maximum radial distance from the crack tip to the perimeter of the yielded region in an elastic-perfectly-plastic material is $R_{\max} \approx 1.4R_P$ for all combinations of K_I and K_{II}. Details of the shapes of the plastic zones will follow soon. The next sections are devoted to the numerical solution procedure applied for the calculation of the fields and the J-integral.

2.4.2 The J-integral

Following the successful solution of the mechanical fields for a given combination of applied loading and material properties, the J-integral can be computed along several circular arcs of different radii. The J-integral is calculated with the domain integral method of Li et al (1985). The derivation by Li et al (1985), is strictly valid only for non-linear elastic materials where the J-integral is path-independent, and not for materials obeying flow theory where non-proportional loading is present and J is path-dependent. However, the domain integral method is still valid for obtaining the radial average of J over the domain. The proof of this statement is as follows. First, the definition of J for a counterclockwise path Γ encircling the crack tip is (Rice, 1968, 1968),

$$J = \int_{\Gamma}\left(Wn_1 - \sigma_{ji}n_j u_{i,1}\right)d\Gamma \tag{2.40}$$

where n_i are the Cartesian components of the outward unit normal to the path, u_i are the Cartesian components of the displacement gradient, and W is the integrated material

work density, $W = \int \sigma_{ij}\, d\varepsilon_{ij}$. Consider the associated domain integral introduced by Li et al (1985).

$$J = -\int_A \left(W q_{,1} - \sigma_{ji} q_{,j} u_{i,1} \right) dA \tag{2.41}$$

where A is an area that contains both the top and bottom crack faces as part of its boundary. For our specific calculations A will be a circular annulus with inner radius R_i and outer radius R_o. For nonlinear elastic materials J is path-independent and $J_A = J$ for any q that is unity along the inner boundary of A and zero along its outer boundary. For the present radial average proof the function q must be,

$$q = \frac{r - R_o}{R_i - R_o} \rightarrow q_{,j} = \frac{r_j}{R_i - R_o} = \frac{n_j}{R_i - R_o} \tag{2.42}$$

Substituting (2.3) into (2.2) we obtain,

$$J_A = -\int_A \left(W q_{,1} - \sigma_{ji} q_{,j} u_{i,1} \right) dA = \frac{1}{R_0 - R_i} \int_{R_i}^{R_0} \left[\int_{-\pi}^{\pi} \left(W n_1 - \sigma_{ji} n_j u_{i,1} \right) r\, d\theta \right] dr \tag{2.43}$$

and hence J_A is the radial average of J over all circular paths between R_i and R_0. Therefore, when $J(r)$ is reported using a domain integral, r is taken as the average of R_i and R_0.

For any path Γ that does not pass through any part of the plastic zone it can be proven that the J-integral is equal to

$$J_\infty = \frac{1 - \nu^2}{E} \left(K_I^2 + K_{II}^2 \right) \tag{2.44}$$

2.4.3 Finite Element Implementation and Computational Aspects

The calculation of the crack tip fields and the J-integral is carried out by separating the $x-y$ plane into two regions, a small circular region of radius R that must encompass the entire plastic zone and the remainder of the plane composed of linear elastic material.

The inner circular region is represented by a radial focused mesh of nine-node isoparametric elements as shown on the left of Figure 2.4.1. The arc subtended by each element is $\pi/25$, and the radial length of the elements varies from $R/400$ for the first ring of elements around the crack tip to $R/20$ for the last ring. In order to assure that the plastic zone is always contained within the finite-element region we take the location of the analytic/finite-element interface to be twice the characteristic size of the plastic zone.

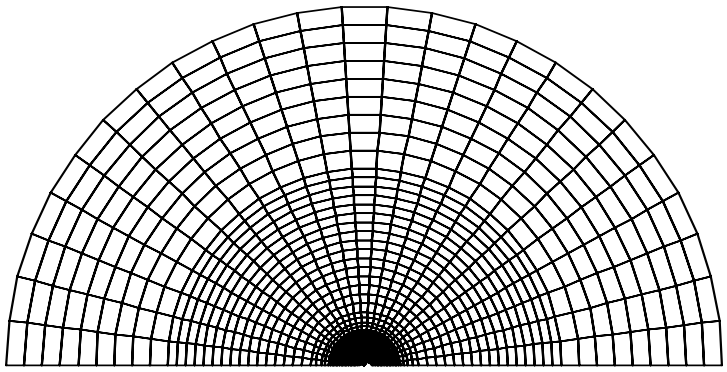

Figure 2.4.1 Circular, radially focused mesh used in the calculations for mode I loading. The radius of the mesh is $R = 1 = 2R_P$.

Along the boundary region r > R, represented by the Dirichlet to Neumann map, we have both stiffness contributions and forces associated with the $K-T$ field to the boundary of the finite element mesh. The finite element connectivity of the infinite region

stiffness mimics a super-element with stiffness interactions between each of the degrees of freedom on the arc $r = R$. However, if the node numbering of the finite element region proceeds first in the angular coordinate and then in the radial coordinate, the overall bandwidth of the full stiffness matrix is not increased by the fully dense contribution of the infinite region stiffness. The number of terms retained in the A and B series of Equations (2.27)-(2.30) used to generate the contributions to the forces and stiffness from the analytic region is 1000. We have seen that accurate solutions can be obtained with far fewer terms, but the cost associated with computing this number of terms is minor.

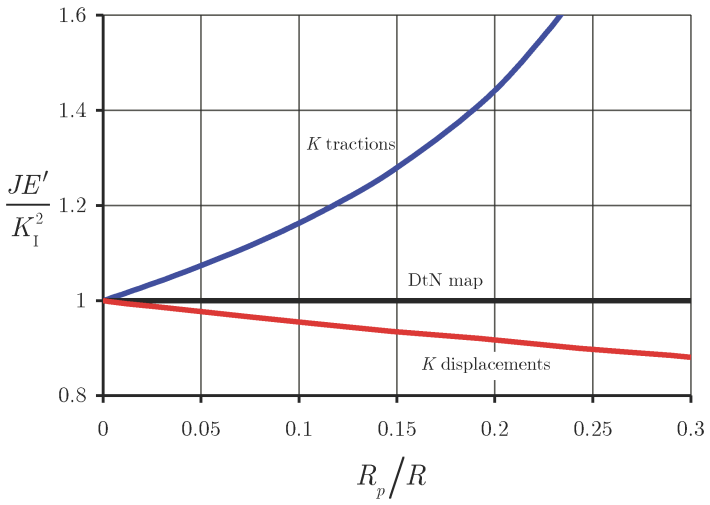

Figure 2.4.2 The J-integral as a function of the characteristic plastic zone size (Eq. ()) for a crack extending to the center of an elastic-perfectly plastic circular region of radius R for three sets of boundary conditions; applied tractions associated with a K-field, applied displacements associated with a K-field, and the DtN map boundary conditions. The parameter $E' = E/(1-\nu^2)$.

Ultimately these boundary conditions allow for a very dense mesh in the plastic zone with no degrees of freedom expended by attempting to model the infinite region with a large but finite domain. Furthermore, no finite size approximation, imposed by

applying either traction or displacement boundary conditions at a finite radial distance, is needed to represent the far-field loading since the true infinite boundary conditions are enforced to within the same accuracy as the angular discretization on the arc $r = R$ allows. In order to demonstrate and quantify how errors are generated by implementing a finite region, Figure 2.4.2 plots the *J*-integral (Rice, 1968), computed by the domain integral method (Li et al, 1985), as a function of R_p / R for three sets of boundary conditions: displacements corresponding to the K_I-field on $r = R$, tractions corresponding to the K_I-field on $r = R$, and the DtN-map conditions.

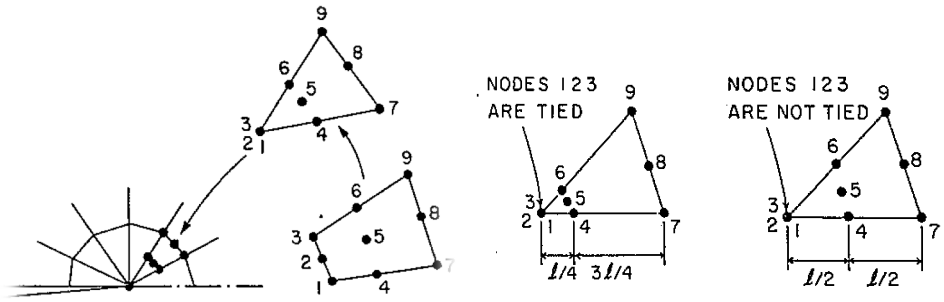

Figure 2.4.3 Crack tip elements formed by collapsing the nine-node elements, for the linear elastic and elastic-perfectly plastic case respectively.

The DtN boundary conditions are able to recreate the small-scale yielding limit as long as plastic zone does not intersect the boundary of the circular finite-element region. In contrast, the *K*-field traction and displacement boundary conditions show significant differences between the actual value of *J* and its effective applied value as the plastic zone grows towards the boundary of the finite domain.

Since we are interested in the computation of fields well contained in the plastic zone, to avoid phenomena of volumetric locking due to the plastic incompressibility the selective reduced four-point integration (Fried, 1974; Nagtegaal et al, 1974), is used to

'penalize, the volumetric part and full nine-point integration for the deviatoric part of the element stiffness matrix, i.e.

$$K_{ab} = \underbrace{\int_{V^{ele}} B_a^T C^{dev} B_b \, dV}_{3\times 3 \text{ Gauss integration}} + \underbrace{\int_{V^{ele}} B_a^T C^{vol} B_b \, dV}_{2\times 2 \text{ Gauss integration}} \tag{2.45}$$

Another computational aspect of importance is the correct representation of the crack tip singularity. For perfect plasticity, when $N = 0$ and where the desired strain singularity is $1/r$, the crack tip elements are triangular elements created by collapsing one side of the nine-node quadrilaterals and giving each of the crack tip nodes separate degrees of freedom, Figure 2.4.3. We have found that for perfect plasticity, moving the mid-side nodes along the rays to the quarter-points as suggested by Barsoum (1977), is inferior to keeping them at the midpoint. This is likely due to the fact that the $1/\sqrt{r}$ strain field that exists in the quarter-point elements corrupts the $1/r$ singular strain field. In fact, we were not able to obtain mode II solutions for perfect plasticity with the quarter-point elements. The quarter-point elements are used, and provide very accurate results, for the linear elastic cases, (Manu, 1985). In this case the nodes at the tip are constrained and not allowed to move. The former case of the collapsed the quarter-point elements with separate degrees freedom for the tip nodes is usually used to approximate singularities with some strain hardening.

Here, however for the strain hardening cases the special six-node singular triangular elements developed by Stern (1979) are implemented around the crack tip. These elements conform perfectly on the rest of the nine-node elements of the rest of the

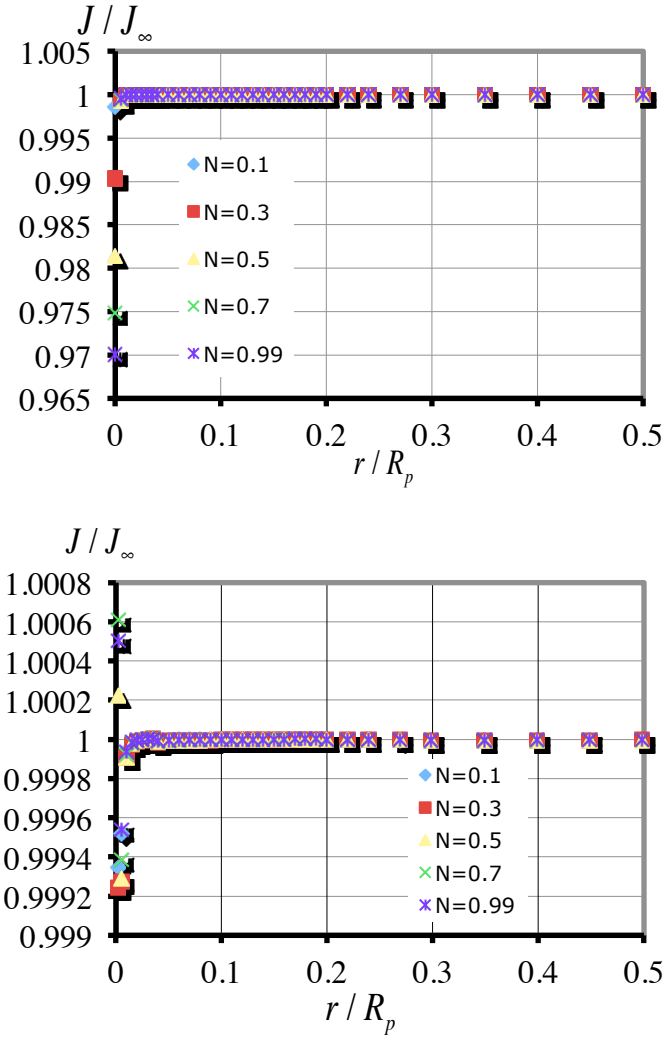

Figure 2.4.4 J-integral using deformation theory and different values of the hardening exponent N. The upper Figure corresponds to the collapsed quarter point element tied at the tip and the lower to the triangular elements (Stern, 1979).

mesh and any strain singularity of the form $1/r^{\frac{1}{1+N}}$ is captured exactly. Details on the shape functions are shown in Appendix. A The effect of the crack tip singularity on the J-integral value close to the crack tip for these two cases is shown in Figure 2.4.4 for deformation theory and different values of the hardening exponent N. It can be seen that the approximation of the crack tip singularity on the strain field, can lead to variations of

up to 3% of the J -integral from the far field value. Details on the J -integral calculation are presented shortly.

In the following section results will be reported for the shapes of the plastic zones, the stresses near the crack tip, and for the radial variation of the J -integral. Dimensional analysis can be used to prove that normalized quantities like σ_{ij}/σ_0, $\varepsilon_{ij}/\varepsilon_0$ and J/J_∞ are independent of the ratio of σ_0/E, and hence the path-dependence of J only needs to be investigated over the following parameter space,

$$\frac{J\left(r/R_P\right)}{J_\infty} = f\left(\nu, N, \psi, \frac{T}{\sigma_0}, \frac{S}{\sigma_0}\right) \tag{2.46}$$

where

$$\psi = \arctan\left(\frac{K_{II}}{K_I}\right) \tag{2.47}$$

Results over a range of these parameters are presented next.

2.4.4 Results

The first set of results presented in Figure 2.4.5 are the shapes of the plastic zones for mode I, mode II, and mixed mode loading with $K_I = K_{II}$ for an elastic-perfectly-plastic material with $\nu = 0.3$, and $S = T = 0$. The size of the plastic zones is dictated by the magnitudes of the intensity factors and is given specifically by Equation (2.39). Note that the factor of $25/4$ multiplying the K_{II} contribution to R_p indicates that the mode II plastic zone size is significantly larger than the mode I zone for equivalent levels of the intensity factors.

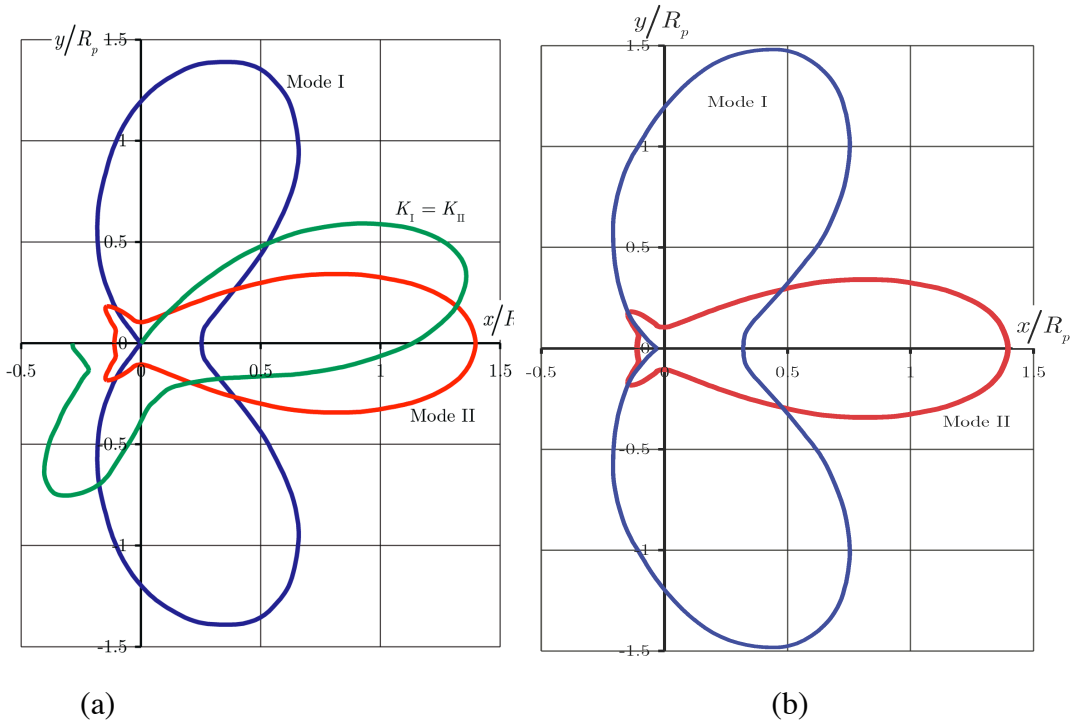

Figure 2.4.5 (a) Plastic zone shapes for mode I (blue), mode II (red) and mixed-mode loading with $K_I = K_{II}$ (green) for an elastic-perfectly plastic material with $\nu = 0.3$ and $S = T = 0$. (b) The corresponding plastic zones using deformation theory plasticity.

Also note that the addition of hardening to the calculations does change the size and shape of the plastic zones. Our numerical results for the effect of N on the plastic zone are very similar to those shown by Shih (1974). As observed by Rice and Tracey (1973) and Du and Hancock (1991), the mode I plastic zone does not entirely surround the crack tip. Our calculations indicate that the elastic sectors extend from $-180^o \le \theta < 148^o$ and $148^o \le \theta < 180^o$. Given the differences in mesh density, this result is in agreement with these prior studies (recall that the arc covered by each element is 7.2^o in this work). Comparing with the plastic zones for the J_2-deformation theory of plasticity presented in the previous section we see that while the overall shape of the

plastic zone is similar to that from flow theory, the elastic sector on the crack flanks does not exist. Computations for pure Mode II indicate that the plastic zones predicted from the flow and deformation theories are nearly indistinguishable from one another.

An additional comparison between flow theory and deformation theory is shown in Figure 2.4.6. Figure 2.4.6 plots the angular distribution of stresses near the crack tip for the same cases studied in Figure 2.4.5. In each of these figures the solid lines correspond to flow theory and the dashed lines to deformation theory. Figure 2.4.6(a) shows that for mode I the deformation theory results follow the Prandtl crack tip field perfectly, while the flow theory results differ from the Prandtl field throughout the entire angular range. We find that the flow theory results for the axial stress in the constant stress sector ahead of the crack tip is $\sigma_{yy} = 2.85\sigma_0$ when $\nu = 0.3$ and $\sigma_{yy} = 2.89\sigma_0$ when $\nu = 0.49$, as compared to the values of $2.96\sigma_0$ and $2.90\sigma_0$ when $\nu = 0.3$ computed by Rice and Tracey (1973) and Du and Hancock (1991) respectively. For deformation theory our computed result for stress ahead of the crack tip is $\sigma_{yy} = 2.97\sigma_0$, which is in nearly perfect agreement with the Prandtl slip-line field prediction. In contrast, the flow and deformation theory results for mode II are practically identical to one another, as the dashed lines for the deformation theory results are hidden by the solid flow theory curves. Finally, as for the mode I result, the mixed mode case shows a difference between the flow and deformation theories. Note however, that for this case the two theories are coincident near the crack flank that bounds the plastic zone. Given that the J-integral is path-independent for flow theory plasticity only in the cases where it mimics deformation theory, i.e. for proportional loading at all points in the plastic zone, these results suggest that the most significant cases of path-dependence should occur under predominantly mode I loading.

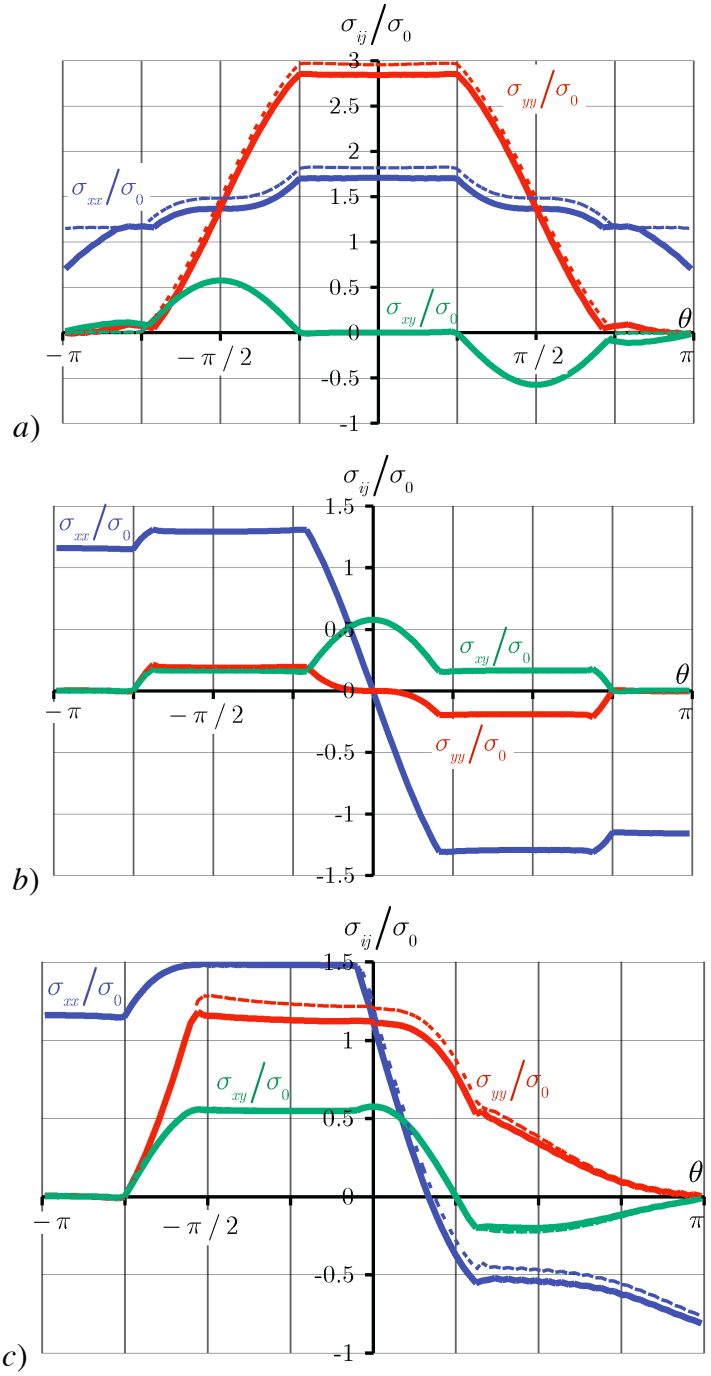

Figure 2.4.6 Angular variations in the Cartesian components of the stress around a crack tip in an elastic-perfectly plastic material with $\nu = 0.3$ and $S = T = 0$ for *a*) mode I, *b*) mode II and *c*) $K_I = K_{II}$. Solid lines are the solutions for flow theory and dashed lines are for deformation theory.

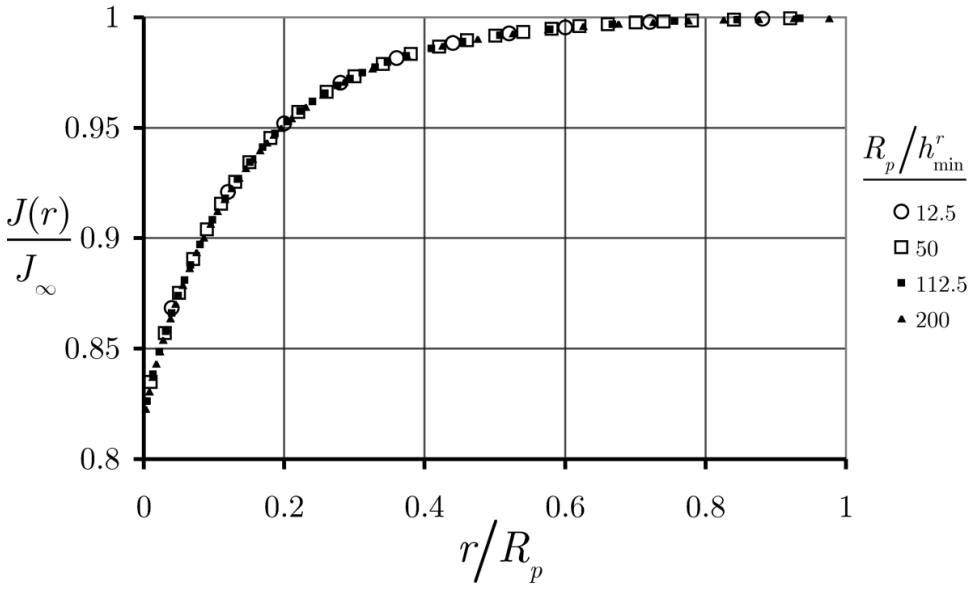

Figure 2.4.7 Values for the J-integral for a circular contour of radius r computed by the domain integral method near a crack tip under mode I loading in an elastic-perfectly plastic material with $\nu = 0.3$. The markers correspond to different points along the load history and different sizes of the plastic zone relative to the minimum radial dimension of the elements surrounding the crack tip.

Figure 2.4.7 illustrates the primary and perhaps the most intriguing result of this Chapter. Here, the path-dependence of the J-integral for mode I loading on an elastic-perfectly plastic material with $\nu = 0.3$, and $S = T = 0$ is demonstrated. Included on this plot are results from four different K_I levels from the same simulation corresponding to plastic zone sizes that are 12.5, 50, 112.5, and 200 times the radial dimension of the first ring of elements surrounding the crack tip, $h_{\min}$. The loading to the final K_I level is broken into 400 equal increments, such that these plastic zone sizes result from 100, 200, 300 and 400 load steps respectively. The results in Figure 2.4.7 demonstrate several features of the present numerical solution. First, self-similarity of the solution is achieved even when the plastic zone is relatively small compared to the finite element mesh size. A second test of the self-similarity of the solution is on the normalized crack tip opening

displacement, $\delta_t \sigma_0 / J_\infty$. For this calculation with $\nu = 0.3$, we find that $\delta_t \sigma_0 / J_\infty = 0.61$ after the full 400 load steps, and that this normalized quantity is larger than 0.61 by 10% and 1% after 14 and 81 load steps respectively. Hence again, self-similarity of the numerical solution is achieved after approximately 100 of the 400 load steps to within a 1% level of convergence. For comparison, the numerical results obtained by Rice and Tracey (1973) and Levy et al. (1971) are $\delta_t \sigma_0 / J_\infty = 0.54$ and 0.47 respectively, and an approximation due to Rice, (1968), is $\delta_t \sigma_0 / J_\infty = 0.67$. Note that the quality of the self-similarity of the present results is a testament to the utility and accuracy of the infinite boundary conditions that have been implemented. The second feature of the numerical solution displayed in Figure 2.4.7 is the convergence of the results with respect to both mesh density and load increment refinement. Here, both mesh density with respect to the plastic zone size and the load increments are effectively refined as the loading progresses. We have also studied the convergence of the solution by fixing the mesh density and increasing the number of load increments, and by fixing the number of load increments and increasing the mesh density. In both cases we find the same features that are shown in Figure 2.4.7. Specifically, increasing either the mesh density or the number of load increments increases the computed level of J path-dependence, i.e. the J / J_∞ results converge to their final results from above. The linearly extrapolated J / J_∞ values at $r = 0$ are 0.842, 0.824, 0.820, and 0.819 for $R_P / h_{\min}$ equal to 12.5, 50, 112.5, and 400 respectively. Finally, note that since the largest radial extent of the plastic zone is approximately $1.4R_P$ the J contour on $r = R_P$ actually passes through the plastic zone. At $r = R_P$ these calculations show that $J = 0.9997 J_\infty$. For all of the contours outside of the plastic zone the calculated J is less than 0.01% above the theoretical value of Equation (2.44). We find that for $\nu = 0.3$, J evaluated along a contour of zero radius about the crack tip is 18% lower than its far field value. The next sets of results illustrate

the effects of the hardening exponent and the mode-mix on the path-dependence of J, again for $\nu = 0.3$ and $S = T = 0$.

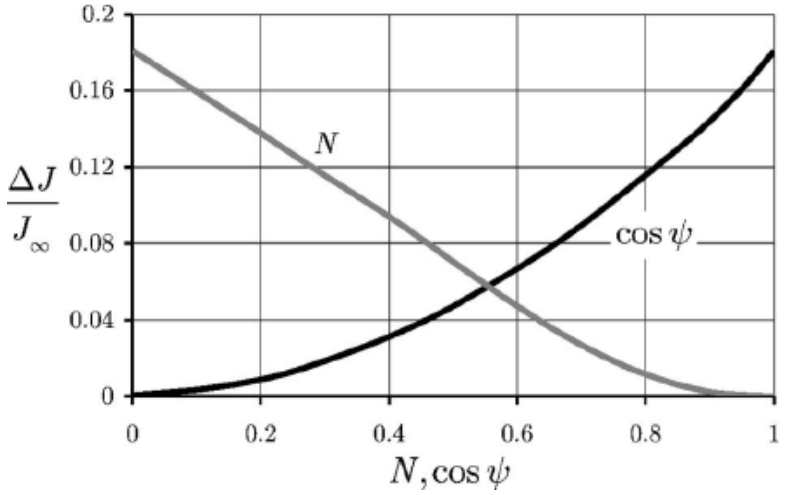

Figure 2.4.8 The effects of the strain hardening exponent in mode I and the mode mix for the perfect plasticity on the relative decrease in J at the crack tip. As for the previous results $\nu = 0.3$ and $S = T = 0$

With regard to the hardening exponent it is well known that J must be path-independent for $N = 1$, which corresponds to a linear elastic material.

This is in fact what the numerical results presented in Figure 2.4.8 show, with $\Delta J / J_\infty$ decreasing monotonically from 18% for perfect plasticity to zero for linear elastic behavior. Also displayed on Figure 2.4.8 is the effect of mode-mix on the path-dependence. Here $\cos\psi = 0$ corresponds to pure mode II and $\cos\psi = 1$ is pure mode I. The stress and strain fields for pure mode II have been analyzed to determine if proportional loading occurs at all points in the plastic zone, and this was found not to be the case. Hence, this finding does not suggest that $\Delta J / J_\infty$ should be zero in this case, however, at least to within the accuracy of the present numerical results, it is not possible to claim that $\Delta J / J_\infty$ is not equal to zero for mode II loading. In addition to the circular integration paths studied with the domain integral method, $\Delta J / J_\infty$ was also computed

using a trapezoidal rule along non-circular and asymmetric contours connecting adjacent integration station for mode II loading and the result that $\Delta J / J_\infty$ is very close to zero persists.

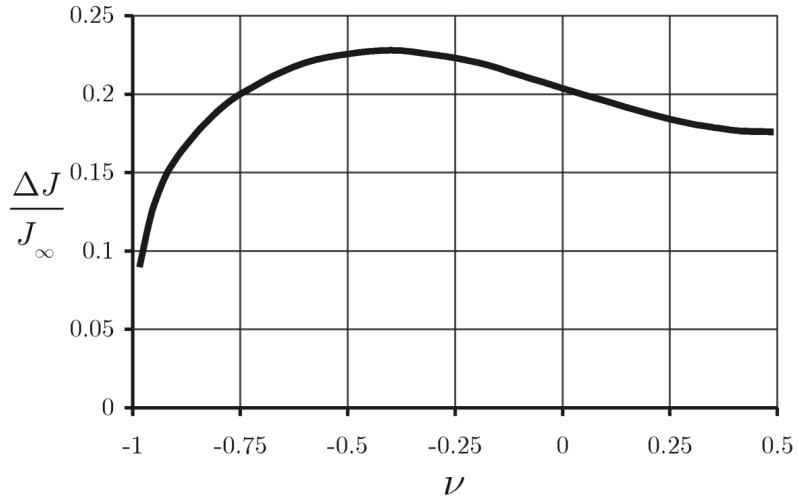

Figure 2.4.9 The effect of Poisson's ratio on the relative decrease in J at the crack tip for pure mode I loading in an elastic-perfectly plastic material.

As mentioned previously, it is possible to prove through dimensional analysis that the ratio σ_0 / E has no effect on the results for the path-dependence of J, and this has been verified numerically as well. However, the Poisson's ratio does have a mild effect on $\Delta J / J_\infty$ for $\nu > 0$ and a much more marked effect for $\nu < 0$.

Figure 2.4.10 plots the relative decrease in J at the crack tip with respect to the far field value for mode I loading and $S = T = 0$ over the full range of Poisson's ratios in an elastic-perfectly plastic material. $\Delta J / J_\infty$ ranges from 17.5% when $\nu = 0.49$, to 20.5% at $\nu = 0$, and finally to 39.5% at $\nu = -0.99$. Therefore, for properties characteristic of most ductile metals, Poisson's ratio has little effect on the value of $\Delta J / J_\infty$ which is close to 18% for $0.1 < \nu < 0.4$.

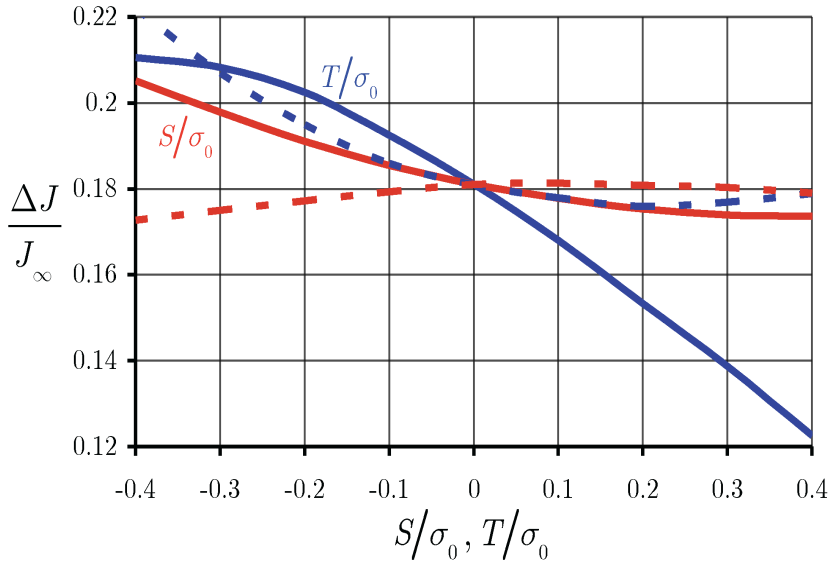

Figure 2.4.10 The effects of the nonsingular S- and T-stresses on the relative decrease in J at the crack tip for pure mode I loading in an elastic-perfectly plastic material. The red curves correspond to the existence of S with $T=0$, and the blue to the existence of T with $S=0$. The dashed lines represent solutions when the nonsingular stresses are applied proportionally with K_I and the solid curves are for when S or T is applied prior to K_I.

The final investigation to be presented is on the effects of the T- and S-stresses. Du and Hancock (1991) performed a detailed study of the effects of the T-stress on the crack tip constraint, and Rice (1974) has commented on issues associated with neglecting T-stresses. Overall, our computations confirm Du and Hancock's results about the effects of T on the extent of the elastic sector and the sizes and shapes of the plastic zones. Here, we also investigate the effects of the nonsingular S-stress (the far field σ_{zz} component of the stress tensor), and again our focus is on the path dependence of J. Note that for the mixed-mode loadings shown in Figure 2.4.8, K_I and K_{II} were applied proportionally. For the T- and S-stresses, we have studied both a proportional application of the transverse stresses with the K-field, as well as applying the transverse stress prior to the application of K_I. The proportional loading study is motivated by a

monotonic loading of a specimen with an arbitrary three-dimensional geometry and loading with mode I symmetry. In such cases T, S and K_I are each proportional to the loading parameter and thus, are proportional to one another throughout the loading. One issue that results from this type of loading is that the solution for the fields is not self-similar. For very small, applied loadings the nonsingular stresses are close to zero, but the K-field persists and produces a plastic zone like the one illustrated in Figure 2.4.5. However, as the load is increased the S and T stresses grow and have a significant and ever-changing impact upon the plastic zone size and shape, the overall field distributions, and the path-dependence of the J-integral. In contrast, if the non-singular stresses are applied prior to the K-field loading, then self-similarity is maintained with the plastic zone and associated fields growing into an unvarying loaded environment. The results for the path-dependence of J for either S or T acting in the absence of the other are shown in Figure 2.4.10. Overall the effect of the non-singular stresses is relatively mild with compressive/tensile stresses tending to increase/decrease the amount of path-dependence (although the reverse occurs in the case of a proportionally applied S-stress).

2.5 DISCUSSION

In this chapter we have presented what Givoli and co-workers have called the Dirichlet-to-Neumann map, which is a method that couples an analytic series solution to a finite-element solution. The method is able to handle two types of singularities that arise in the analysis of fracture mechanics problems. The first type of problem is on the analysis of small-scale yielding situations where a non-linear material process is occurring near the crack tip. Here, Rice's boundary layer formulation (1968), calls for the analysis of an infinite region, leading to unbounded displacements in the limit as $r \to \infty$. In this case the DtN method uses an analytic solution to describe the elastic behavior

outside of the process zone, and finite-elements to compute the details of the non-linear material response near the crack tip. The DtN map allows for no degrees of freedom to be wasted by modeling an infinite region with a large but finite domain. The second class of problems is concerned with recovering the stress intensity factors and *T*-stress for a crack in a linear elastic body. In this case, the stresses and strains are singular at the crack tip. Here, the analytic solution describes the fields near the crack tip and finite-elements are used in the remainder of the object where the geometry and loading may be complex, but the mechanical fields are well behaved.

The primary drawback of the method is that the computation of the DtN map contributions to the finite-element stiffness and forces is not trivial in comparison to say collapsing the side of an isoparametric quadrilateral and moving the mid-side nodes to the quarter-points, (Barsoum, 1977). However, once $[\mathbf{K}^{DtN}]$ and $\{\mathbf{F}^{DtN}\}$ are determined for a given finite-element discretization of the arc surrounding the crack tip, these quantities can be saved and ported to solve any number of problems. The benefits of the DtN map include significant savings in finite-element degrees of freedom, accuracy in the determination of fracture parameters, and simplicity in the deconvolution of K_{I}, K_{II}, and *T*. The savings in degrees of freedom stems from the fact that the DtN map can be used to represent the largest possible circular region that is described by the analytic solution. For the small-scale yielding problems this means making *R* as small as possible to surround any non-linear material behavior, and for linear elastic problems this means making *R* as large as possible without making the circle intersect other boundaries in the specimen geometry. That K_{I}, K_{II}, and *T* are determined directly from the method implies that there is no need to attempt to decouple modes by computing the components of the *J*-integral J_k, or by matching the stress fields around the crack or the crack opening/sliding displacement profiles to their asymptotic counterparts.

Furthermore, the specific examples studied here are for homogeneous isotropic elastic behavior. However, the method presented in Section 2.1 is not restricted as such and can be used for anisotropic and, when analytic solutions can be generated, inhomogeneous or functionally graded elasticity (see for example (Kim and Paulino, 2002) and references therein). In fact, the extension of the method to linear piezoelectric behavior is straightforward as well. In the anisotropic and piezoelectric cases, the terms in the analytic series solutions can be generated using the Stroh formalism (Stroh, 1958; Ting, 1996; Sou et al., 1992).

It is noteworthy that several pioneering researchers in the field of non-linear fracture mechanics have made very careful remarks about the path-independence of the J-integral in the context of flow theory plasticity, (Rice, 1968; Rice and Rosengren, 1968; Hutchinson, 1968; Shih, 1981; Rice, 1967; Li et al., 1985; Rice and Tracey, 1973; Du and Hancock, 1991). However, a quantitative determination of the path-dependence of J under in-plane loading conditions has not appeared. This manuscript has attempted to fill that gap with accurate numerical analyses. Several of the results presented in this work are in rough quantitative agreement with prior works. Additionally, in all of the cases presented here for flow theory, we have also performed the corresponding deformation theory calculations and have found J to be in agreement with the theoretical value of Equation (2.44) to within 0.1% for all paths, including the ring of elements in contact with the crack tip. Hence, our numerical methods yield accurate results for J in the case of deformation theory where path-independence is a rigorously proven result. there are two other studies that support the findings presented here. Levy et al (1971) noticed that the strength of the strain singularity near the crack tip was smaller than approximations based upon deformation theory plasticity. Their rough approximation of the effect on the crack tip value of J was a 25% reduction, which is certainly in

qualitative agreement with the present result of 18%. Kuang and Chen (1996) also studied J within the plastic zone in a compact tension specimen and found similar path-dependence in mode I.

Chapter III Crack Tip Fields in Ferroelastic Materials

In this chapter the stress and strain fields for a stationary plane strain crack in a ferroelastic material are presented using the previous computational framework for the application of the far field boundary loading. The constitutive behavior of the material is taken to be characteristic of a polycrystalline sample assembled from randomly oriented tetragonal single crystal grains. The constitutive law accounts for the strain saturation, asymmetry in tension versus compression, Bauschinger effects, reverse switching, and strain reorientation that can occur in these materials due to the non-proportional loading that can arise near a crack tip. Detailed finite element calculations are carried out to determine the stress and strain fields in the vicinity of the crack tip, and to compute values for the J -integral on various integration paths around the tip. The results of the calculations are discussed in relation to results for growing cracks and for stationary cracks in standard elastic–plastic materials.

3.1 Constitutive Law for Ferroelastic Switching

The nonlinear constitutive response of ferroelastic ceramics is a result of the mechanism of domain switching, which is also thought to be responsible for other intrinsic features of the ferroelastic behavior, that is, the characteristic hysteresis loop in the stress-stain relation and the asymmetry in tension and compression. A more detailed discussion of domain switching and the constitutive behavior of ferroelectric and ferroelastic materials can be found in Huber et al., (1999), Kamlah (2001), or Landis (2004). Here we are interested in the behavior of ferroelastic polycrystals and a phenomenological constitutive description that can be readily implemented within finite element computations. Such a model has been developed by Landis (2003a) and is a special case of the more general model for ferroelectrics, Landis (2002). For

completeness the constitutive equations are reviewed here. Assuming linear kinematics, the total strain tensor is decomposed in an elastic part and the permanent remanent or plastic strain as usual, i.e. $\varepsilon_{ij} = \varepsilon_{ij}^{e} + \varepsilon_{ij}^{r}$, and isotropic elastic response is assumed such that the stress–strain relations are written as

$$\varepsilon_{ij} = \frac{1+\nu}{E}\sigma_{ij} - \frac{\nu}{E}\sigma_{kk}\delta_{ij} + \varepsilon_{ij}^{r} \tag{3.1}$$

Here, ε_{ij}, ε_{ij}^{r} and σ_{ij} are the Cartesian components of the infinitesimal strain tensor, the remanent strain tensor and the Cauchy stress tensor, ν is the Poisson's ratio and E is the Young's modulus. In all cases discussed in this chapter, the datum for remanent strain is the state of the material as cooled from above the Curie temperature.

The purpose of the nonlinear constitutive law is to provide the evolution of the remanent strain history given the stress or total strain history. Consistent with the fact that domain switching gives rise to deviatoric strains and ferroelastic ceramics exhibit kinematic hardening effects, it is assumed that the material responds elastically within a switching surface in the modified stress space $\hat{s}_{ij} = s_{ij} - s_{ij}^{B}$ to be given as

$$\Phi = \frac{3}{2}\hat{s}_{ij}\hat{s}_{ij} - \sigma_0^2 = 0 \tag{3.2}$$

where $s_{ij} = \sigma_{ij} - \sigma_{kk}\delta_{ij}/3$ is the deviatoric part of the Cauchy stress tensor and s_{ij}^{B} is the deviatoric part of the back stress and σ_0 is the initial switching (yield) strength of the material in tension or compression. If the stress state is on the switching surface and the load increment induces remanent straining, then the remanent strain increment is normal to the switching surface such that

$$\dot{\varepsilon}_{ij}^{r} = \lambda\left(s_{ij} - s_{ij}^{B}\right) \tag{3.3}$$

where λ is the plastic multiplier.

The back stress tensor leads to kinematic hardening and must be used to enforce the remanent strain saturation conditions. The approach used to determine the back stresses is based on the assumption that the internal state of the ferroelastic material is completely characterized by the components of the remanent strain tensor (Cocks and McMeeking, 1999; Landis, 2002). This assumption leads to the identification of a remanent potential, $\Psi^{r}\left(\varepsilon_{ij}^{r}\right)$, such that the back stresses are derived from the potential by the following formula

$$\sigma_{ij}^{B} = \frac{\partial \Psi^{r}}{\partial \varepsilon_{ij}^{r}} \tag{3.4}$$

In order to complete the constitutive theory, the form of the remanent potential $\Psi^{r}\left(\varepsilon_{ij}^{r}\right)$ must be specified. As previously noted, ferroelectric ceramics exhibit an asymmetry in the attainable levels of remanent strain in tension versus compression. The micromechanical simulations of Frolich (2001), Landis (2003a), and Landis et al (2004) suggest that in random polycrystals with underlying tetragonal crystal structure, the ratio of remanent strain possible in tension to that possible in compression is 1.37:1. This theoretical value is in the same range as the ratio of the maximum poling remanent strain to the maximum compressive remanent strain due to stress depolarization measured in PLZT by Lynch (1996) and in PZT by Fang and Li (1999). By implementing the micromechanical model of Huber et al. (1999), Landis (2003a), determined the full range of remanent strain saturation states. The following procedure is used to determine when

saturation is approached. First, since the remanent strain due to domain switching is volume conserving, the following two remanent strain invariants are used to describe any multi-axial remanent strain state.

$$J_2^e = \left(\frac{2}{3} e_{ij}^r e_{ij}^r \right)^{1/2} \text{ and } J_3^e = \left(\frac{4}{3} e_{ij}^r e_{jk}^r e_{ki}^r \right)^{1/3} \tag{3.5}$$

Here, e_{ij}^r is the remanent strain deviator, $e_{ij}^r = \varepsilon_{ij}^r - \varepsilon_{kk}^r \delta_{ij} / 3$. With the definition of these two invariants, a full range of remanent strain saturation states can be probed by allowing the ratio of J_3^e / J_2^e to vary from -1 (axisymmetric contraction) to 0 (pure shear) to 1 (axisymmetric extension).

Next, the strain-like variable $\bar{\varepsilon}$ is defined as

$$\bar{\varepsilon} = J_2^e f\left(\frac{J_3^e}{J_2^e} \right) \tag{3.6}$$

where

$$f\left(\frac{J_3^e}{J_2^e} \right) = -0.0965 \left(\frac{J_3^e}{J_2^e} \right)^3 + 0.01 \left(\frac{J_3^e}{J_2^e} \right)^6 + 0.8935 \quad \text{for} \quad \left(\frac{J_3^e}{J_2^e} \right) < 0 \tag{3.7}$$

and

$$f\left(\frac{J_3^e}{J_2^e} \right) = -0.1075 \left(\frac{J_3^e}{J_2^e} \right)^3 - 0.027 \left(\frac{J_3^e}{J_2^e} \right)^6 - 0.028 \left(\frac{J_3^e}{J_2^e} \right)^{21} + 0.8935 \quad \text{for} \quad \left(\frac{J_3^e}{J_2^e} \right) \geq 0 \tag{3.8}$$

Here, f is a functional fit to the numerical results obtained from micromechanical computations. When the remanent strain level characterized by $\bar{\varepsilon}$ reaches the compressive saturation level, ε_c, the remanent strain will be saturated. In other words, the only possible remanent strain states in the material are those that satisfy $\bar{\varepsilon} \le \varepsilon_c$. In order to prohibit remanent strain states characterized by $\bar{\varepsilon} > \varepsilon_c$, the remanent potential $\Psi^r\left(\varepsilon_{ij}^r\right)$ is constructed to increase without bound as $\bar{\varepsilon} \to \varepsilon_c$.

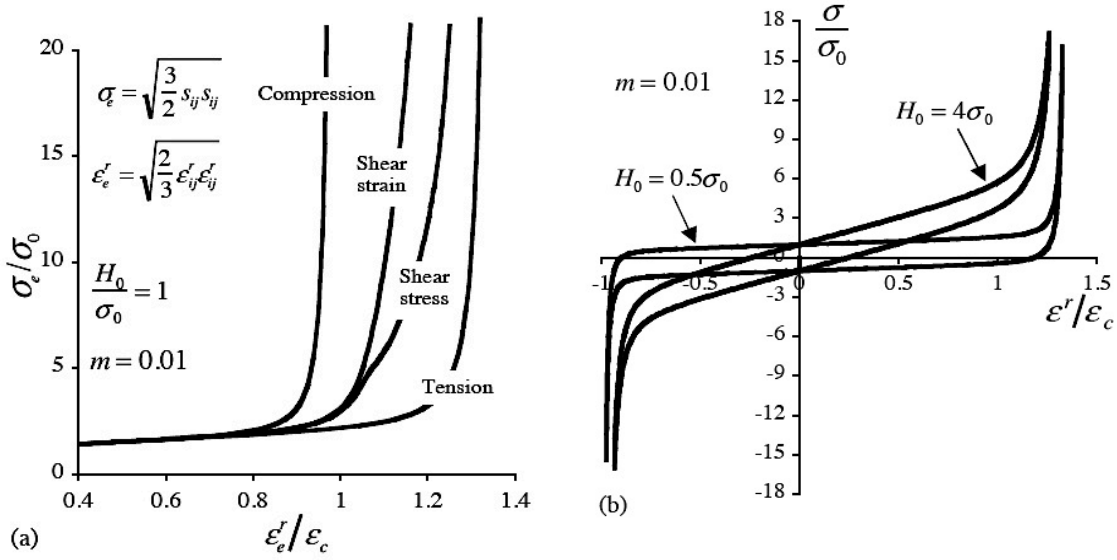

Figure 3.1.1 (a) Effective stress versus effective remanent strain curves for the model material described in uniaxial compression, pure shear strain, pure shear stress and uniaxial tension tests. (b) Uniaxial stress versus remanent strain hysteresis loops for the model material illustrating the effect of the hardening parameter H_0. In both cases notice the asymmetry in the remanent strains that can be achieved in tension versus compression.

The simple functional form of the remanent potential that has been chosen for this fracture study is,

$$\Psi^r = \frac{1}{2} H_0 \varepsilon_c \left[\frac{J_2^e}{\varepsilon_c} \exp\left(\frac{m}{1 - \bar{\varepsilon} / \varepsilon_c} \right) \right]^2 \tag{3.9}$$

H_0 is a characteristic level of back stress that primarily affects the initial slope of the uniaxial stress versus remanent strain curve, and *m* is another hardening parameter that controls how abruptly the strain saturation conditions are reached.

Figure 3.1.1(a) illustrates the predictions of the effective stress versus the effective remanent strain from the constitutive law for uniaxial compression, pure shear strain, pure shear stress and uniaxial tension. Note that the shear strain and shear stress curves do not coincide. This behavior is due to the fact that the material can strain more in tension than in compression, and has been confirmed in micromechanical simulations. This feature of the constitutive behavior also has consequences for the remanent strain fields near crack tips in mode II loading. Figure 3.1.1(b) illustrates the uniaxial stress versus remanent strain hysteresis curves for a few different sets of the material parameters H_0 and *m*. The constitutive model is now completely specified, and can be used to compute remanent strain histories.

3.2 FINITE ELEMENT IMPLEMENTATION

The finite element implementation of the problem of a stationary, plane strain crack in a ferroelastic material under pure Mode I and Mode II loadings is presented in this section along with details of the numerical integration of the constitutive equations. The derivation of the algorithmic tangent modulus consistent with the aforementioned integration is discussed.

3.2.1 Integration of Constitutive Equations and the Algorithmic Tangent Matrix

The stress state is updated by the integration of the non-linear constitutive equations using a Backward Euler scheme. At every iteration, the remanent strain increments have to satisfy the following set of non-linear equations.

$$\Delta\varepsilon_{ij}^{r} - \frac{3\Delta\varepsilon^{r}}{2\sigma_0}\left[2\mu\left(e_{ij}^{t+\Delta t} - \varepsilon_{ij}^{r,t} - \Delta\varepsilon_{ij}^{r}\right) - s_{ij}^{B}\right] = r_{ij} = 0 \tag{3.14}$$

where $\Delta\varepsilon^{r} = \sqrt{\frac{2}{3}\Delta\varepsilon_{kl}^{r}\Delta\varepsilon_{kl}^{r}}$. The above equations are solved iteratively using the Newton-Raphson method. The strain increments update is written to first order as $\Delta\varepsilon_{ij}^{r,i+1} = \Delta\varepsilon_{ij}^{r,i} + d\varepsilon_{ij}^{r}$ where $d\varepsilon_{ij}^{r}$ is computed by the linear equations

$$J_{ijkl}\, d\varepsilon_{ij}^{r} = -r_{ij}^{i} \tag{3.15}$$

where J_{ijkl} is the Jacobian of the system.

Once the remanent strain state is determined the algorithmic tangent modulus is computed by varying the strain in (3.14) and noting that at the converged solution we have $\Delta\varepsilon_{ij}^{r} = 3\lambda\left(s_{ij}^{I+1} - s_{ij}^{B}\right)$. Substituting in the incremental stress-strain constitutive relation we then have

$$d\sigma_{ij} = \left(\lambda_e + 2\mu\right)\delta_{ij}\, d\varepsilon_{kk} + 2\mu\left(\delta_{ik}\delta_{jl} - 6\lambda\mu A_{ijkl}\right) de_{kl} \tag{3.16}$$

where λ_e is the *Lame* constant and δ_{ij} the Kronecker delta. Details on the computation and specific forms of the matrices are given in Appendix B.

3.2.2 Numerical Method

Consider a semi-infinite crack lying on a polycrystalline ferroelastic material, with faces on the negative x- axis and the crack tip at the origin of the coordinate system. For the computations of the crack tip fields, it is assumed that the applied loading is small such that the maximum radial dimension of the switching zone around the crack is much smaller than the length of the crack or any other specimen length dimension. As discussed by Rice (1968), under these conditions a small scale switching analysis can be performed on a semi-infinite crack with the remote applied stress field being that of the asymptotic elastic *K*-fields,

$$\begin{Bmatrix} 2\mu u_x \\ 2\mu u_y \end{Bmatrix} = K_{\mathrm{I}}\sqrt{\frac{r}{2\pi}} \begin{Bmatrix} \left(\kappa - \frac{1}{2}\right)\cos\left(\frac{\theta}{2}\right) - \frac{1}{2}\cos\left(\frac{3\theta}{2}\right) \\ \left(\kappa + \frac{1}{2}\right)\sin\left(\frac{\theta}{2}\right) - \frac{1}{2}\sin\left(\frac{3\theta}{2}\right) \end{Bmatrix} + K_{\mathrm{II}}\sqrt{\frac{r}{2\pi}} \begin{Bmatrix} \left(\kappa + \frac{3}{2}\right)\sin\left(\frac{\theta}{2}\right) + \frac{1}{2}\sin\left(\frac{3\theta}{2}\right) \\ \left(-\kappa + \frac{3}{2}\right)\cos\left(\frac{\theta}{2}\right) - \frac{1}{2}\cos\left(\frac{3\theta}{2}\right) \end{Bmatrix} as \; r \to \infty. \tag{3.17}$$

Here K_I and K_{II} are the remote applied mode I and mode II stress intensities and r and θ are polar coordinates centered on the crack tip. In order to apply these remote boundary conditions the Dirichlet to Neumann (DtN) map technique is used as described in Chapter I and Carka et al., (2011). The DtN map allows for the exact application of the remote boundary conditions, and it also allows for all of the finite element degrees of freedom to be used solely in the vicinity of the crack tip where the interesting constitutive processes are occurring without wasting any computational effort by attempting to model an infinite region with a large but finite domain. Under plane strain conditions an approximation for the characteristic size of this switching zone, R_S, is given as

$$R_S = \frac{1}{3\pi} \frac{K_I^2 + \frac{25}{4} K_{II}^2}{\sigma_0^2} \tag{3.18}$$

In the following a more detailed discussion of the size and shape of the plastic zone in both mode I and mode II loadings will be presented. In addition to the stress, strain and remanent strain fields near the crack tip, values for the J -integral, Rice (1968), are also computed on several circular contours centered on the crack tip. Here again, the J -integral is computed using the domain integral technique of Li et al. (1985)

$$J = -\int_A \left(W q_{,1} - \sigma_{ji} q_{,j} u_{i,1} \right) dA \tag{3.19}$$

where J is a counterclockwise directed contour encircling the crack tip, u_i are the components of the displacement vector, and W is the strain-history-dependent stress work density at a material point defined by

$$W = \int_0^{\varepsilon_{ij}} \sigma_{ij} \, d\varepsilon_{ij} \tag{3.20}$$

Furthermore, the area A contains both the top and bottom crack faces as part of its boundary and is that of circular rings of elements surrounding the crack tip and $q_{,i}$ are the derivatives of a smooth function taking the values one and zero on the inner and outer circular boundary. For nonlinear elastic materials J is path-independent and $J_A = J$ for any q that is unity along the inner boundary of A and zero along its outer boundary. We showed that, for cases where J is path-dependent, by selecting the function q as

$$q = \frac{r - R_o}{R_i - R_o} \rightarrow q_{,j} = \frac{r_j}{R_i - R_o} = \frac{n_j}{R_i - R_o} \tag{3.21}$$

then J_A is equal to the radial average of J for all circular paths in A. Here R_i and R_o are the inner and outer radius of the circular annulus.

Within this model dimensional analysis dictates that all field quantities, for example the stresses will be of the form

$$\frac{\sigma_{ij}}{\sigma_0} = \bar{\sigma}_{ij}\left(\frac{x}{R_S}, \frac{y}{R_S}; \frac{\varepsilon_c E}{\sigma_0}, \frac{H_0}{\sigma_0}, m, \nu\right) \tag{3.21}$$

where $\bar{\sigma}_{ij}$ are dimensionless functions of the normalized spatial coordinates parameterized by the normalized material quantities. Also note that R_S is the characteristic size of the switching zone given by Eq. (3.18). Additionally the J-integral will only depend on the dimensionless material parameters and the radial size of the integration contour, $r = \frac{R_i + R_0}{2}$ as

$$\frac{J}{J_\infty} = \bar{J}\left(\frac{r}{R_S}, ; \frac{\varepsilon_c E}{\sigma_0}, \frac{H_0}{\sigma_0}, m, \nu\right) \tag{3.23}$$

Finally, a circular region of radius $R = 1$ surrounding the crack tip is modeled using a radial focused mesh of 9-noded isoparametric elements with radial length varying from $R/400$ for the tip ring to $R/100$ on the boundary. The constant angular variation is equal to $\pi/25$. The volumetric part of the strains is integrated using a reduced integration scheme whereas the deviatoric part uses the full 9- point integration. In anticipation of high stresses close to the crack tip assuming that the material surrounding it is in a fully

saturated state, the crack tip stress singularity of $1/\sqrt{r}$ is taken into account by collapsing and constraining the quarter point 9-node element at the tip.

3.3 RESULTS

The numerical calculations for a plane strain stationary crack presented in this section are performed employing a full circular mesh for the Mode II loading. Taking into consideration the symmetry in Mode I, only half of the mesh is considered. For all of the calculations to be presented the Poisson's ratio is taken to be $v = 0.3$ and the hardening exponent parameter is $m = 0.01$.

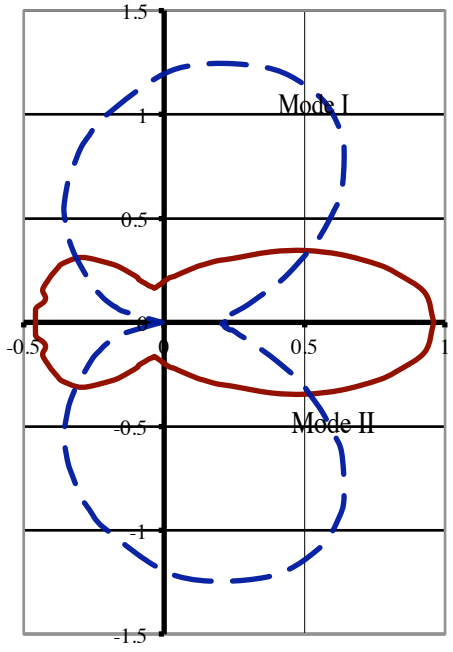

Figure 3.3.1 Plastic zone shapes for pure Mode I and Mode II loading

Figure 3.3.1 shows the shapes of the plastic zones for Mode I and Mode II loading for $\frac{H}{\sigma_0} = 1$ and $\frac{E\varepsilon_c}{\sigma_0} = 5$. The K-field loading, specifying the size of the zone is given by (3.24) and for all calculations is equal to 0.5. The effect of the parameter $\frac{H}{\sigma_0}$ to the

shape of the zones is similar to the effect the hardening exponent has on the shape of plastic zones for power law hardening materials, Hutchinson (1968) and Carka and Landis (2011). As $\frac{H}{\sigma_0}$ increases, the Mode I zone shape becomes more and more symmetric with respect to the y-axis. The Mode II zone shrinks ahead of the crack tip and expands on the crack faces. The effect of $\frac{E\varepsilon_c}{\sigma_0}$ to the shape of the zones much less pronounced but increasing the value of the ratio leads to overall smaller size of the plastic zone. It is also worth noting that compared to the elastic-perfectly plastic case the overall size of the switching zones is smaller. This is because part of the zones is in the saturation limit and stresses rise higher with the linear elastic slope for the ferroelastic material.

Figures 3.3.2 and 3.3.3 show the angular variation of the remanent strain components very close to crack tip for Mode II and Mode I loading respectively. All the quantities plotted are normalized with the compressive saturation strain. The variable $\bar{\varepsilon}$, controlling the ability of the material to respond to a multiaxial deformation is very close to the saturation limit ε_c, implying that further switching cannot be sustained by the material. Notice in Figure 3.3.3 that the axial remanent strain components are not equal to zero on the plane ahead of the crack tip even though, due to considerations of the mode II symmetry, the axial stresses on this plane are zero. This is a consequence of the tension–compression asymmetry in the strain saturation that is manifested in Figure 3.1.1 as a difference in the constitutive responses in pure shear stress versus pure shear strain.

The stress variation is very similar to the findings in Landis (2003b). The angular variation of the stresses close to the crack tip for the two modes of loading is plotted with the marker lines in Figure 3.3.4 (a) and (b) respectively. The solid lines correspond to the asymptotic stress distribution in a linear elastic material. Note that the stresses are normalized with the elastic asymptotic singularity.

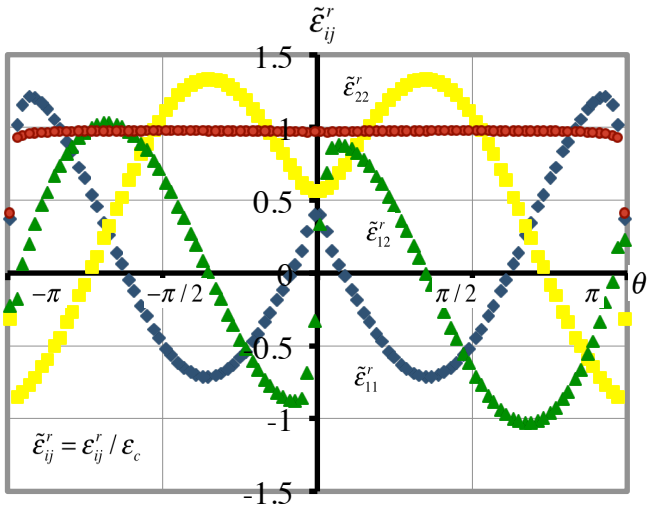

Figure 3.3.2 Angular variation of the remanent strains close to the crack tip for Mode I loading and for material parameters $H/\sigma_0 = 1$, $E\varepsilon_c/\sigma_0 = 5$, $\nu = 0.3$.

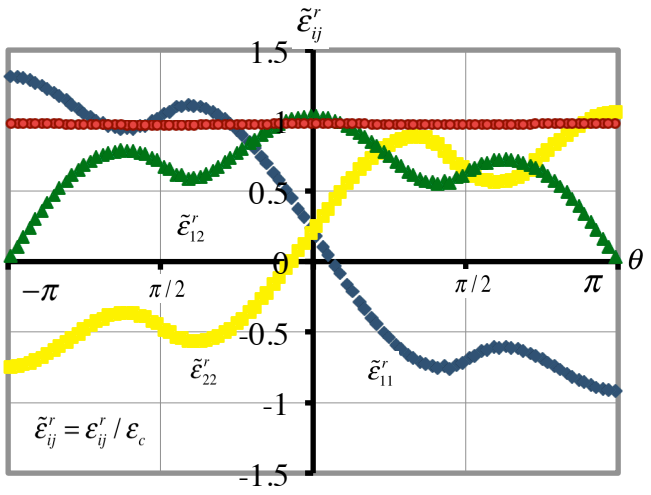

Figure 3.3.3 Angular variation of the remanent strains close to the crack tip for Mode II loading and the same material parameters as in Figure 2.3.2.

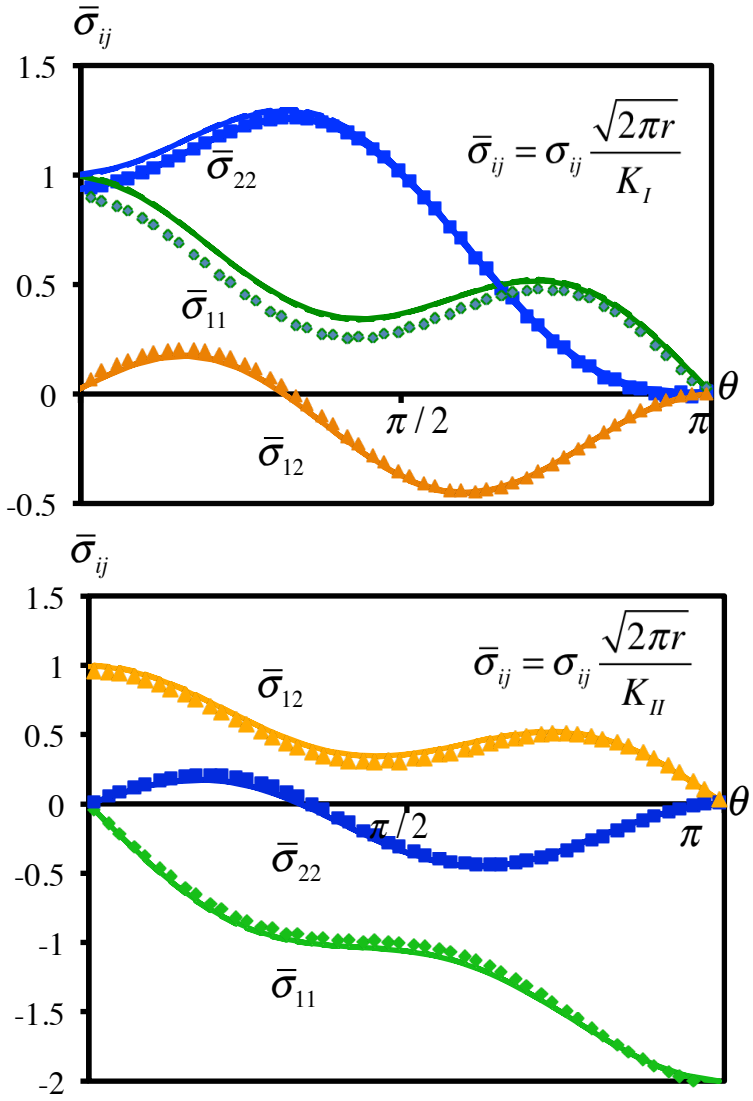

Figure 3.3.4 (a) Angular variation of the stresses close to the crack tip for Mode I loading and for material parameters $H/\sigma_0 = 1$, $E\varepsilon_c/\sigma_0 = 5$, $\nu = 0.3$. (b) Angular variation of the stresses close to the crack tip for Mode II loading for the same material parameters.

Due to strain saturation the stresses close to the tip have a rapid increase and we see that the elastic $1/\sqrt{r}$ singularity is recovered at the crack tip as the region close to the tip is very close to saturation, but the angular variation differs from the elastic asymptotic field.

Next, we proceed in the presentation of a quite interesting feature of the path-dependence of the J-integral in ferroelastic materials. The J-integral, calculated on paths that do not intersect the switching zone is related to the applied far field K loading through where E is the Young's modulus.

$$J_{\infty} = \frac{1-\nu^2}{E}\left(K_I^2 + K_{II}^2\right) \tag{3.31}$$

Figure 3.3.6 shows the variation of the J-integral, shows the variation of the J-integral normalized by the far field applied J_{∞} for different circular paths around the crack tip at different levels of the applied mode I loading. The far-field loading is applied in 400 increments and the J-integral is computed along all circular paths at every 100 increments. These four loading levels correspond to sizes of the switching zones which are 12.5, 50, 112.5 and 200 times larger than the radial extend of the crack tip ring of elements $h_{\min}$, indicating the amount of numerical refinement that exists at each of these load levels. Figure 3.3.6 indicates that the self-similarity of the solution is well established after 200 increments.

Note that all of the integration paths reported in the figure lie either entirely within or at least intersect the switching the zone.

It is interesting to note that for r/R_S between 0.2 and 1, the J-integral follows the behavior of an elastic–perfectly plastic material without saturation, although the actual amount of the path-dependence differs by approximately 3% compared with similar calculation given in Carka and Landis (2011). It can be argued that the path-dependence in this region is not significant, but it does contrast the rising behavior as the integration contour becomes more deeply embedded within the switching zone where the

material surrounding the tip is strain saturated. The rising value of the J-integral eventually reaches approximately 9% above the applied value at the crack tip for $H/\sigma_0 = 1$ and $\varepsilon_c E/\sigma_0 = 5$.

Figures 3.3.7(a) and (b) illustrate the effects of the saturation strain $\varepsilon_c E/\sigma_0$ and the hardening parameter H/σ_0 on the path-dependence of the J-integral in mode I loading. As discussed in Landis (2003b), the material parameters H/σ_0 and $\varepsilon_c E/\sigma_0$ have a strong effect on the fracture toughness enhancement in ferroelastic ceramics during steady crack growth. These parameters also affect the path-dependence of J presented in this work for stationary cracks.

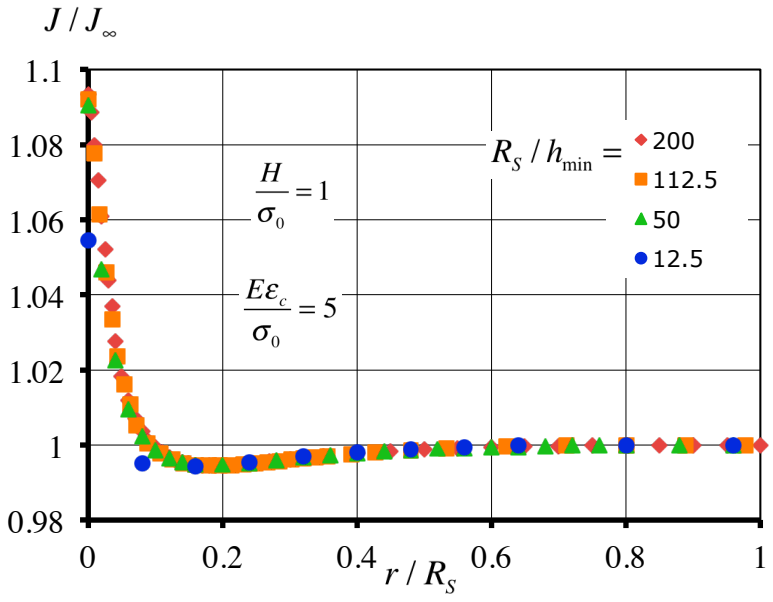

Figure 3.3.6 The J-integral versus the radius of the circular integration contour for mode I loading. The different markers refer to different applied loading levels from the same simulation illustrating the self-similarity of the solution.

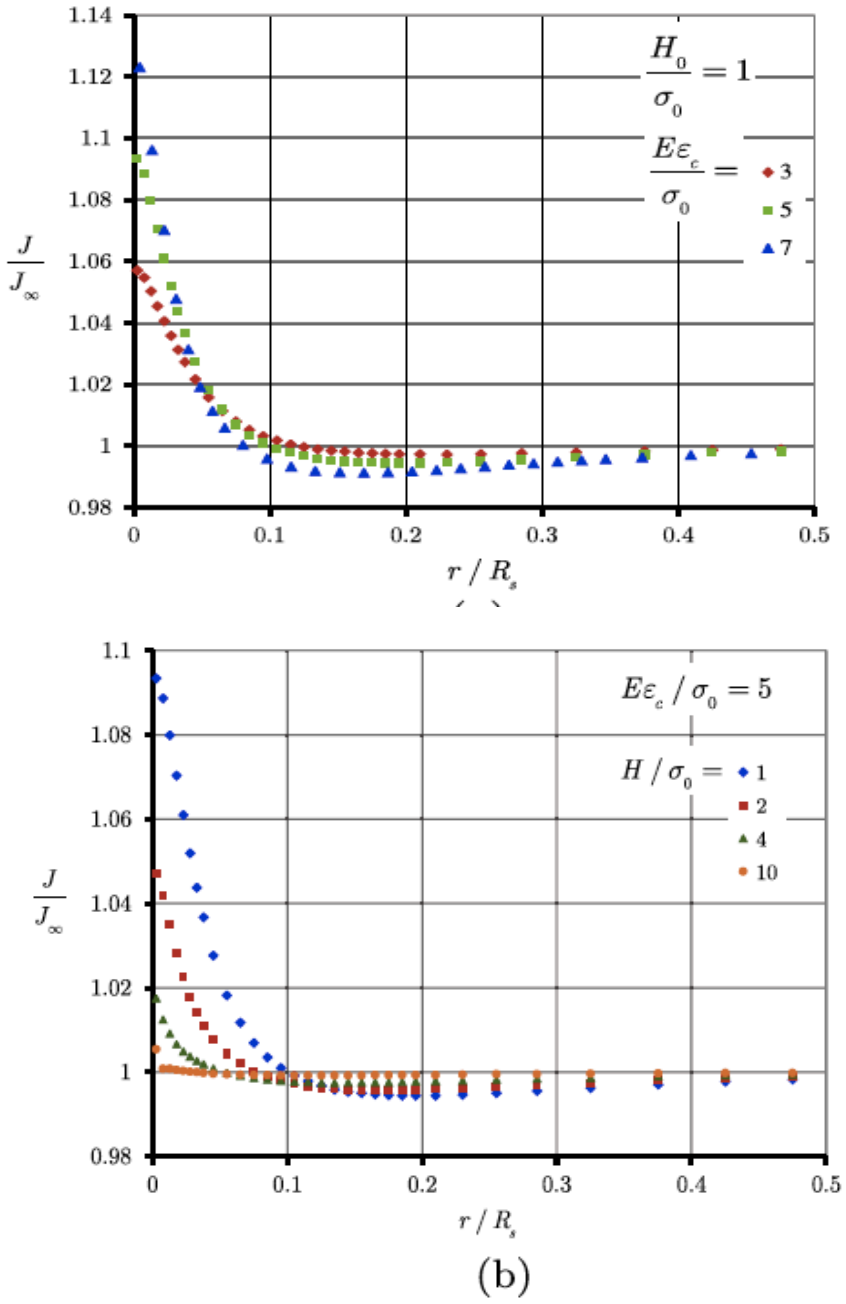

Figure 3.3.7 The J -integral versus the radius of the circular integration contour for mode I loading for (a) different levels of the saturation strain $\varepsilon_c E / \sigma_0$ and (b) different levels of the hardening parameter H / σ_0.

The stress required to create a specific amount of remanent strain increases with increasing H/σ_0. On the other hand increasing values of $\varepsilon_c E/\sigma_0$ implies stress relaxation since the material is able to accommodate more irreversible strain. Increasing values of $E\varepsilon_c/\sigma_0$ seem to increase mostly the near tip J integral value and show little effect on the decreasing part of the J-integral as well as the slope of the rising portion of the plot. Figure 3.3.8 presents the effect of these parameters on the value of the J-integral at the crack tip for mode I loading. The difference between the J-integral at the tip and the far-field applied value is most pronounced for low values of H/σ_0 and increases with increasing $\varepsilon_c E/\sigma_0$. For $H/\sigma_0 = 1$, the deviation from the far-field value is about 5% when $\varepsilon_c E/\sigma_0 = 3$ and 12% for $\varepsilon_c E/\sigma_0 = 7$. The path-dependence of the J-integral becomes less significant for high values of H/σ_0 and the effect of $\varepsilon_c E/\sigma_0$ on J is reduced for large H/σ_0.

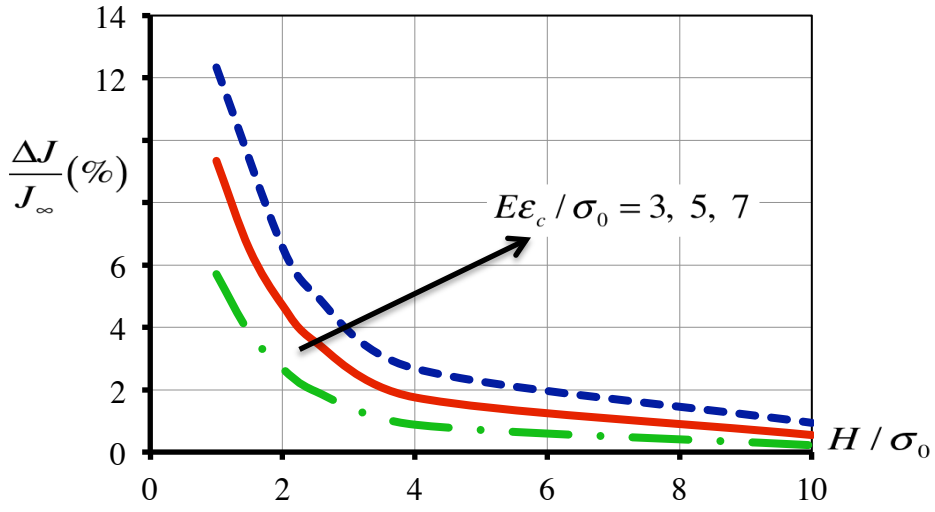

Figure 3 3.8 Dependence of the crack tip J-integral on H/σ_0 and $\varepsilon_c E/\sigma_0$ for Mode I loading.

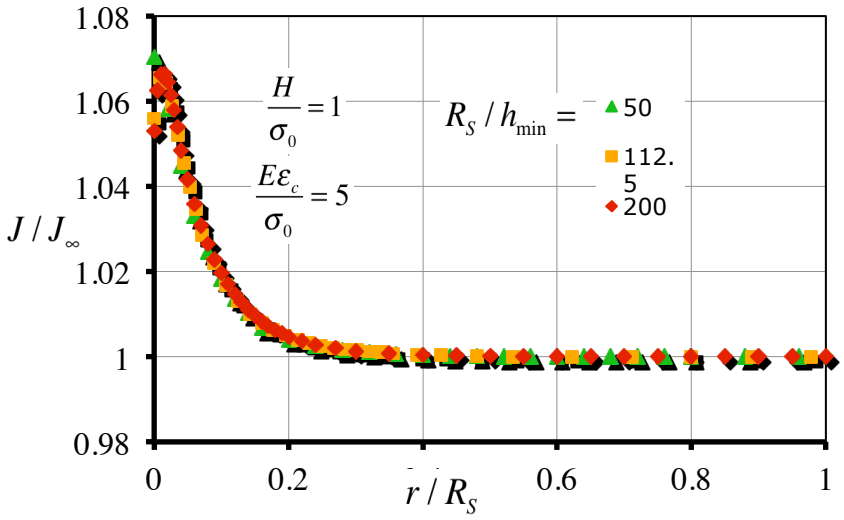

Figure 3.3.9 The J-integral versus the radius of the circular integration contour for mode II loading. The different markers refer to different applied loading levels from the same simulation illustrating the self-similarity of the solution.

Also of interest is the behavior of the path-dependence for pure mode II loading especially when compared to elastic–perfectly plastic case. The calculations in Carka and Landis (2011) demonstrate that the significant path-dependence of the J-integral in mode I practically disappears for mode II loading of a crack in an elastic–perfectly plastic material. Figure 3.3.9 shows that this is not the case for ferroelastic materials. It can be seen that for $r / R_S > 0.3$ the J-integral mimics the path-independent behavior of the elastic–perfectly plastic case. However, as the crack tip is approached the increase of J as seen in the mode I case appears with the J-integral at the tip being about 5% more than the far-field value. Note that for mode II the tip value is not the maximum value of the J-integral which occurs away from the tip. This effect can be attributed to the fact that close to the crack tip the axial remanent strains are non-zero indicating a mode mix at

the saturation region despite the pure mode II loading conditions.

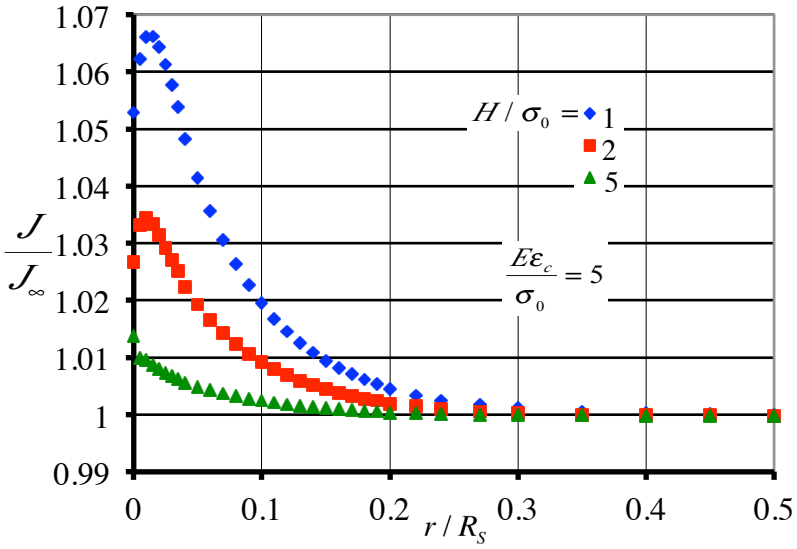

Figure 3.3.10 J-integral versus the radius of the circular paths for Mode II loading and different values of H/σ_0.

Finally, Figure 3.3.10 shows the path-dependence of the J-integral for $\varepsilon_c E/\sigma_0 = 5$ and three different hardening parameters for mode II loading along paths of varying radial distance from the tip. The effect is the same to the Mode I crack. The slope of the rising portion of the plot gradually decreases and the path dependence becomes less pronounced and shrinks deeper into the switching zone. For $H/\sigma_0 = 1$ the deviation from the far field value is about 5% when $E\varepsilon_c/\sigma_0 = 3$ and 12% for $E\varepsilon_c/\sigma_0 = 7$. The difference of the J-integral at the tip from the applied value is pronounced for low values of H/σ_0 and increases with increasing $E\varepsilon_c/\sigma_0$.

3.4 DISCUSSION

In this work we have refrained from explicitly stating a fracture criterion for ferroelastic material. One physically rational criterion for crack growth initiation from a

stationary crack would be that crack growth begins when the crack tip energy release rate is equal to a material specific critical energy release rate, i.e. $G_{tip} = G_c$. Note that due to the path-dependence of the J-integral it is necessary to identify the crack tip energy release rate $G_{tip} = J_{tip}$ since this quantity will not be equal. In fact, our calculations have demonstrated that, with respect to the energy release rate, the domain switching zone around the crack tip causes anti-shielding. This is in contrast to transformation-type switching models, which predict neither shielding nor anti-shielding due to switching near a stationary crack. It is also interesting to note that the material parameters that lead to the greatest levels of anti-shielding around a stationary crack, small H / σ_0 and large $E\varepsilon_c / \sigma_0$, cause the greatest amount of shielding for a growing crack, see Landis (2003b). However, it should be realized that the anti-shielding around a stationary crack is on the order of 10%, while the shielding around a steadily growing crack is 100%–200%. Nevertheless, the crack growth initiation toughness can have a marked effect on fracture loads depending on the initial slope of the R-curve. The point fracture criterion $G_{tip} = G_c$ should be used with considerable caution. While reasonable on the surface this criterion does come with certain embedded assumptions. Specifically, this criterion assumes that the material can sustain a singularity such that the constitutive law being used is valid in the entire domain. Clearly this assumption must break down at some point, but this alone does not invalidate the point fracture criterion. A more realistic fracture criterion would be to introduce a fracture process or cohesive zone to represent the actual material separation mechanics. Typically such cohesive traction separation laws are characterized by a cohesive strength σ_c and a cohesive energy G_c. On can imagine that these parameters can be vastly different depending on the separation mechanics with atomic cleavage having a high σ_c and low G_c and grain pullout having a smaller σ_c but larger G_c. A rough calculation of the distance ahead of the crack where cohesive tractions play

an important role is $R_c = G_c E / \sigma_c^2$. Now if this cohesive length scale is small compared to the strain saturation region predicted by the present model $\left(R_{sat} \approx R_{sat} / 10\right)$ then a point fracture criterion is valid. If the region where cohesive tractions play a role is comparable to the size of the strain saturation zone, then the point fracture criterion can no longer be valid because the reduction in stresses ahead of the crack tip due to the weak separation process will not allow the stresses to increase to the levels required for full strain saturation. This in turn will change the crack tip fields and the overall energy flux into the fracture process zone. For weak fracture processes, like grain pullout, the present results suggest that a more detailed fracture model incorporating a cohesive zone are needed to gain a deeper understanding of ferroelastic fracture.

Chapter IV Phase Field Modeling of Domain Needle Arrays

In-situ microstructural observations of ferroelectric single crystals often reveal highly ordered multi-domain configurations. A common pattern, observed in $BaTiO_3$ single crystal, is that of periodic arrays of needle or wedge-shaped domains coexisting in a parent domain variant. In this chapter we examine the far field electromechanical loading conditions that favor the existence, formation and evolution of compatible and stable needle domain array patterns using a phase-field modeling approach. The infinite arrays of needles are modeled via a representative unit cell and the appropriate electrical and mechanical periodic boundary conditions are applied. The resulting boundary value problems are solved using a non-linear finite element method to determine the details of the needle structure as well as the field distributions around the needle tips. We proceed with a brief introduction on the phase-field formulation and the finite element implementation. Next, we present details on the needle domain structures and their modeling, along with results of the calculations.

4.1. The Phase-Field Model

Su and Landis (2007), working along the lines of Fried and Gurtin (1993, 1994, 1996), developed a continuum mechanics, non-equilibrium, thermodynamic framework for ferroelectrics that distinguishes the fundamental balance laws, which are universal, from the material constitutive response. The balance laws include a balance of micro-forces, which are conjugate to the order parameter describing the evolution of microstructure, in addition to the usual electromechanical balance laws. The material response is established by the analysis of the second law of thermodynamics through a specific form of the Helmholtz free energy chosen to fit the properties of crystals that undergo a ferroelectric phase transition near the spontaneous state. For completeness, the

main points of the theory and the set of the governing equations of the phase-field model for domain structure evolution in ferroelectrics are reviewed next.

4.1.1 Theory Formulation

The phase-field theory along with the electromechanical balance laws considered here are formulated assuming small deformations and rotations. For a body of volume V, bounded by a surface S, the balance of linear and angular momentum of the mechanical fields implies that,

$$\sigma_{ij,j} + b_i = \rho \ddot{u}_i \text{ in V}, \tag{4.1}$$

$$\sigma_{ij} = \sigma_{ji} \text{ in V}, \tag{4.2}$$

$$\sigma_{ij} n_j = t_i \text{ on } S. \tag{4.3}$$

Here, σ_{ij} are the components of the Cauchy stress tensor, ρ is the mass density, b_i are the components of the body force per unit volume, and t_i and n_i are the components of the traction vector and the unit normal on the surface element respectively.

Linear kinematics implies that the infinitesimal strain tensor ε_{ij} is related to the components of the displacement vector u_i by,

$$\varepsilon_{ij} = \frac{1}{2}\left(u_{i,j} + u_{j,i}\right) \text{ in V}. \tag{4.4}$$

For actuator and sensor applications velocities are usually less than the speed of sound, well bellow the speed of light. Therefore the appropriate quasi-electrostatic form of Maxwell's equations, governing the electrical quantities reads:

$$D_{i,i} = q \text{ in V}, \tag{4.5}$$

$$D_i n_i = -\omega \text{ on } S, \tag{4.6}$$

$$E_i = -\phi_{,i} \text{ in V}, \tag{4.7}$$

where D_i and E_i are the components of the electric displacement and electric field, ϕ is the electric potential, q is the volume charge density and ω is the surface charge density respectively.

Within the linear piezoelectricity theory, the solution of a boundary value problem requires the introduction of the appropriate boundary conditions along with the constitutive equations required to connect the field quantities satisfying the fundamental balance laws to the kinematical fields describing the configuration of the body. While the boundary conditions are tailored to the specific problem the constitutive equations describing the material behavior can be derived by introducing a free energy that depends on the configurational quantities, the strain and the electric displacements in this case, via thermodynamic considerations.

In the phase-field setting however, we are not only interested in the distribution of the fields, but also in how these fields cause the domain structure to evolve. The theory now must incorporate internal material interfaces separating domain variants, the domain walls, and additionally the location of these boundaries must be determined as part of the

solution. The free energy of the material combined with the micro-force balance laws, must be able to represent the spatial distribution and temporal evolution of these internal interfaces within the ferroelectric crystal. Hence, the free energy depends on the order parameter identifying the phases and its spatial gradient.

The dependence of the free energy on the gradient of the order parameter will result in a phase interface of finite width where the order parameter varies continuously. This departure from the sharp interface not only provides a computational benefit to the phase-field theory, since the interface is not being tracked explicitly, but also results in a more realistic representation of the structure and energy of domain walls. The natural order parameter for ferroelectrics is the polarization vector. The relationship between the polarization vector, the electric displacement and the electric field in V is given as

$$D_i = P_i + \kappa_o E_i, \tag{4.8}$$

where κ_o is the permittivity of free space.

Given that the free energy is permitted to depend on a new order parameter, a set of micro-forces are introduced that are work-conjugate to the order parameter. The set of forces postulated are: (a) a micro-force tensor ξ_{ji} such that $\xi_{ji} n_j \dot{P}_i$ represents the power density expended across surfaces by neighboring configurations (b) an internal micro-force vector π_i such that $\pi_i \dot{P}_i$ is the power density expended by the material internally, which also accounts for dissipation in the material, e.g. in the ordering of atoms within unit cells of the lattice, and (c) an external micro-force vector γ_i such that $\gamma_i \dot{P}_i$ is the power density expended by external sources. This micro-force is akin to the mechanical body force b_i and the electrical charge density q. A balance of this set of micro-forces is postulated as,

$$\int_S \xi_{ji} n_j \, dS + \int_V (\pi_i + \gamma_i) dV = 0 \tag{4.9}$$

which leads to the differential balance law for the micro forces given as,

$$\xi_{ji,j} + \pi_i + \gamma_i = 0 \ in \ V. \tag{4.10}$$

The first law of thermodynamics accounting for the thermal, electromechanical and domain wall energy conversion of the continuum is given as:

$$\frac{d}{dt}\left(\int_V \rho \dot{u}_i \dot{u}_i \, dV + \int_V e \, dV \right) = \int_V \left(b_i \dot{u}_i + \varphi \dot{q} + \gamma_i \dot{P}_i \right) dV + \int_S \left(t_i \dot{u}_i + \varphi \dot{\omega} + \xi_{ji} n_j \dot{P}_i \right) dS + \int_V r \, dV + \int_S -c_i n_i \, dS \tag{4.11}$$

where e is the internal energy density, c_i are the components of the inward heat flux vector per unit area and r is the supply of heat per unit volume from external source. Using the traction and surface charge definition equations (4.4) and (4.6) respectively in the second term of the right hand side of equation (4.11), applying the divergence theorem and eliminating terms that satisfy the balance equations (4.2), (4.5) and (4.10) we are left with the rate of change of internal energy:

$$\frac{de}{dt} = \dot{e} = \sigma_{ij} \dot{\varepsilon}_{ij} + E_i \dot{D}_i - \pi_i \dot{P}_i + \xi_{ji} \dot{P}_{i,j} - c_{i,i} + r. \tag{4.12}$$

Here note that anticipating the dissipative nature of domain wall motion, the internal micro-force vector π_i enters the balance of the micro-forces but does not contribute to the external power.

The constraint of the second law of thermodynamics in the entropy production is given through the pointwise local Clausius-Duhem dissipation inequality as

$$\theta \dot{s} \geq -c_{i,i} + \frac{c_i \theta_{,i}}{\theta} \tag{4.13}$$

where s is the total entropy and θ the absolute temperature.

Using equation (4.12) to eliminate the divergence of the heat flux vector we have

$$\theta \dot{s} \geq \dot{e} - \sigma_{ij}\dot{\varepsilon}_{ij} - E_i \dot{D}_i + \pi_i \dot{P}_i - \xi_{ji}\dot{P}_{i,j} + \frac{c_i \theta_{,i}}{\theta}. \tag{4.14}$$

In terms of the free energy $\psi = e - \theta s$ the second law can be written as

$$\dot{\psi} \leq \sigma_{ij}\dot{\varepsilon}_{ij} + E_i \dot{D}_i - \pi_i \dot{P}_i + \xi_{ji}\dot{P}_{i,j} + \frac{c_i \theta_{,i}}{\theta} - \dot{\theta} s. \tag{4.15}$$

In this thesis we are concerned with spatially homogeneous, temperature independent microstructural evolution, below the Curie temperature. Therefore under isothermal conditions $\left(\dot{\theta} = 0,\ \theta_{,i} = 0\right)$ the dissipation inequality reads

$$\dot{\psi} \leq \sigma_{ij}\dot{\varepsilon}_{ij} + E_i \dot{D}_i - \pi_i \dot{P}_i + \xi_{ji}\dot{P}_{i,j}. \tag{4.16}$$

From (4.1)-(4.3) and (4.10), an equivalent integral of the above equation can be written as

$$\int_V \dot{\psi}\, dV + \frac{d}{dt}\int_V \frac{1}{2}\rho \dot{u}_i \dot{u}_i\, dV \le \int_V \left(b_i \dot{u}_i + \phi \dot{q} + \gamma_i \dot{P}_i\right) dV + \int_S \left(t_i \dot{u}_i + \phi \dot{\omega} + \xi_{ji} n_j \dot{P}_i\right) dS. \tag{4.17}$$

Finally, the independent state variables on which the thermodynamic functional and the thermodynamic conjugate forces, i.e. stresses, electric field micro-force tensor and internal micro-force vector can depend on, is specified next.

For isothermal behavior, below the Curie temperature the thermodynamic functional is the Helmholtz free energy and the independent configurational/state variables are components of strain, electric displacement, polarization vector, polarization vector gradients and possibly polarization rate. The constitutive response is then written as

$$\begin{aligned}
\psi &= \psi\left(\varepsilon_{ij}, D_i; P_i, P_{i,j}, \dot{P}_i\right) \\
\sigma_{ij} &= \sigma_{ij}\left(\varepsilon_{ij}, D_i; P_i, P_{i,j}, \dot{P}_i\right) \\
E_i &= E_i\left(\varepsilon_{ij}, D_i; P_i, P_{i,j}, \dot{P}_i\right) \\
\xi_{ij} &= \xi_{ij}\left(\varepsilon_{ij}, D_i; P_i, P_{i,j}, \dot{P}_i\right) \\
\pi_i &= \pi_i\left(\varepsilon_{ij}, D_i; P_i, P_{i,j}, \dot{P}_i\right)
\end{aligned} \tag{4.18}$$

The question can be raised as to why the free energy must be allowed to depend on $\dot{P}_i$. Since it is anticipated that the internal dissipative part of the micro-force π_i should depend on $\dot{P}_i$, then the axiom of equi-presence demands that all constitutive functionals must be expressed in terms of the same list of state variables at the onset until the

contrary is deduced. It will be shown that the second law inequality ultimately allows only π_i to depend on $\dot{P}_i$. Using the functional form of the Helmholtz free energy given in equation (4.18) we have

$$\frac{\partial \psi}{\partial \varepsilon_{ij}}\dot{\varepsilon}_{ij} + \frac{\partial \psi}{\partial D_i}\dot{D}_i + \frac{\partial \psi}{\partial P_i}\dot{P}_i + \frac{\partial \psi}{\partial P_{i,j}}\dot{P}_{i,j} + \frac{\partial \psi}{\partial \dot{P}_i}\ddot{P}_i \leq \sigma_{ij}\dot{\varepsilon}_{ij} + E_i\dot{D}_i - \pi_i\dot{P}_i + \xi_{ij}\dot{P}_{i,j}, \tag{4.19}$$

or equivalently,

$$\left(\sigma_{ij} - \frac{\partial \psi}{\partial \varepsilon_{ij}}\right)\dot{\varepsilon}_{ij} + \left(E_i - \frac{\partial \psi}{\partial D_i}\right)\dot{D}_i - \left(\pi_i + \frac{\partial \psi}{\partial P_i}\right)\dot{P}_i + \left(\xi_{ij} - \frac{\partial \psi}{\partial P_{i,j}}\right)\dot{P}_{i,j} - \frac{\partial \psi}{\partial \dot{P}_i}\ddot{P}_i \geq 0. \tag{4.20}$$

The inequality (4.20) must hold for any permissible thermodynamic process for arbitrary levels of $\dot{\varepsilon}_{ij}$, $\dot{D}_i$, $\dot{P}_i$, $\dot{P}_{i,j}$ and $\ddot{P}_i$ through the appropriate control of the external sources b_i, q, and γ_i. Since (4.20) is linear in $\dot{\varepsilon}_{ij}$, $\dot{D}_i$, $\dot{P}_i$, $\dot{P}_{i,j}$ and $\ddot{P}_i$ the coefficients of these terms must be zero in order for the inequality to be satisfied for any permissible process The remaining term should satisfy $\left(\pi_i + \frac{\partial \psi}{\partial P_i}\right)\dot{P}_i \leq 0$.

Therefore we have

$$\frac{\partial \psi}{\partial \dot{P}_i}\ddot{P}_i = 0 \rightarrow \psi = \psi\left(\varepsilon_{ij}, D_i, P_i, P_{i,j}\right) \tag{4.21}$$

and

$$\sigma_{ij} = \frac{\partial \psi}{\partial \varepsilon_{ij}},\ E_i = \frac{\partial \psi}{\partial D_i},\ and\ \xi_{ji} = \frac{\partial \psi}{\partial P_{i,j}}. \tag{4.22}$$

Finally setting the internal micro-force equal to $\pi_i = -\frac{\partial \psi}{\partial P_i} - \beta_{ij}\dot{P}_j$, the inequality $-\beta_{ij}\dot{P}_i\dot{P}_j \leq 0$ is satisfied for any level of $\dot{P}_i$ and for β_{ij} positive definite, where β_{ij} can be interpreted as the components of the mobility tensor which carries the dependence of the state variables, i.e. $\beta_{ij} = \beta_{ij}\left(\varepsilon_{kl}, D_k, P_k, P_{k,l}, \dot{P}_k\right)$. For constant β_{ij} and a cubic high-temperature phase the mobility tensor is usually taken to be $\beta_{ij} = \beta\delta_{ij}$, where $\beta > 0$. Substitution of the definitions of internal micro-force vector and tensor, $\pi_i = -\frac{\partial \psi}{\partial P_i} - \beta_{ij}\dot{P}_j$, and $\xi_{ji} = \frac{\partial \psi}{\partial P_{i,j}}$ into the micro-force balance given in equation (4.9) yields:

$$\left(\frac{\partial \psi}{\partial P_{i,j}}\right)_{,j} - \frac{\partial \psi}{\partial P_i} + \gamma_i = \beta_{ij}\dot{P}_j \ \ in\ V. \tag{4.23}$$

Equation (4.23) is generalized form of the Ginzburg-Landau equation governing the evolution of the material polarization in a ferroelectric material as a direct consequence of the postulated micro-force balance introduced earlier in the analysis

4.1.2 The Helmholtz Free Energy Functional

The Helmholtz free energy introduced in (4.18) and further constrained in (4.21) includes both the energy stored in the material and the energy stored in the free space occupied by the material. Specifically, the free energy is decomposed into the free energy of the material and the free energy of the free space such that

$$\psi\left(\varepsilon_{ij}, D_i, P_i, P_{i,j}\right) = \bar{\psi}\left(\varepsilon_{ij}, D_i, P_i, P_{i,j}\right) + \frac{1}{2\kappa_0}\left(D_i - P_i\right)\left(D_i - P_i\right) \tag{4.24}$$

We now proceed to the detailed specification of the free energy. The goal for this task is that the general form of the free energy must contain a sufficient set of parameters such that for a given material these parameters can be fit to the spontaneous polarization, spontaneous strain, dielectric permittivity, piezoelectric coefficients and the elastic properties near the zero stress and zero electric field free spontaneous polarization and strain states. To accomplish this task, Su and Landis (Su and Landis, 2007) introduced the following form for the free energy,

$$\begin{aligned}\psi = & \frac{1}{2}a_{ijkl}P_{i,j}P_{k,l} \\ & + \frac{1}{2}\overline{a}_{ij}P_iP_j + \frac{1}{2}\overline{\overline{a}}_{ijkl}P_iP_jP_kP_l + \frac{1}{2}\overline{\overline{\overline{a}}}_{ijklmn}P_iP_jP_kP_lP_mP_n \\ & + \frac{1}{8}\overline{\overline{\overline{a}}}_{ijklmnrs}P_iP_jP_kP_lP_mP_nP_rP_s \\ & + b_{ijkl}\varepsilon_{ij}P_kP_l + \frac{1}{2}c_{ijkl}\varepsilon_{ij}\varepsilon_{kl} + f_{ijklmn}\varepsilon_{ij}\varepsilon_{kl}P_mP_n + g_{ijklmn}\varepsilon_{ij}P_kP_lP_mP_n \\ & + \frac{1}{2\kappa_o}\left(D_i - P_i\right)\left(D_i - P_i\right)\end{aligned} \tag{4.25}$$

First, note that each of the newly introduced material tensors must contain the symmetry of the high temperature phase, which for most ferroelectrics of interest is cubic. The first term of the free energy penalizes large gradients of polarization and gives domain walls thickness and energy within the model. The four terms on the second and third lines are used to create the non-convex energy landscape of the free energy with minima located at the spontaneous polarization states. The four terms on the fourth line are then used to fit the material's spontaneous strain along with the dielectric, elastic and piezoelectric properties about the spontaneous state. Note that the elastic, dielectric and piezoelectric properties are nonlinear, and therefore the tensor components are fit to the

tangent material properties at the spontaneously polarized state. The final term represents the energy stored within the free space occupied by the material, and according to equation (4.17) is equivalent to $\kappa_o E_i E_i / 2$.

The eighth rank term on the third line was introduced in order to allow for adjustments of the dielectric properties and the energy barriers for 90° switching (Zhang and Bhattacharya, 2005). The sixth rank terms introduced on the fourth line allow us to fit the elastic, piezoelectric and dielectric properties of the low symmetry phase at the spontaneous state. Without these terms the elastic properties of the material arise only from the c_{ijkl} tensor, which must have the symmetry of the high temperature phase. Hence, the phase field modeling that has been performed to date assumes that the elastic properties of tetragonal phase perovskites are both cubic and homogeneous, when in fact the elastic properties have tetragonal symmetry and can have different orientations across a 90° domain wall, i.e. they are inhomogeneous throughout a domain structure. With regard to the piezoelectric coefficients, b_{ijkl} is used to fit the spontaneous strain components associated with the stress and electric field free spontaneous polarization state and by introducing the f_{ijklmn} and g_{ijklmn} tensors the full tetragonal structure of the piezoelectric tensor can be matched. This general form of the free energy is able to fit the magnitudes of the spontaneous polarization, strain components, and the elastic, piezoelectric and dielectric constants near the spontaneous state. This allows for a relatively accurate representation of material properties and comparison of the behaviors of different material compositions.

4.2 Finite Element Implementation

The governing equations for the phase-field model include Equations (4.1)-(4.8), (4.11), (4.22)-(4.23) and (4.25). When formulating a finite element method to solve these

equations we must first identify the field quantities that will be used as nodal degrees of freedom. The simplest formulation would implement the components of mechanical displacement from which strain is derived, the components of electric polarization from which the polarization gradient is derived, and the electric potential or voltage from which electric field is derived. In order to implement such a formulation, the constitutive equations must take ε_{ij} , P_i , $P_{i,j}$ and E_i as the independent variables.

However, the Helmholtz free energy has D_i instead of E_i as the independent variable. To address this issue, the following Legendre transformation is required to derive the electrical enthalpy h ,

$$\begin{aligned} & h\left(\varepsilon_{ij}, P_i, P_{i,j}, E_i\right) = \psi - E_i D_i \\ & = \frac{1}{2} a_{ijkl} P_{i,j} P_{k,l} \\ & + \frac{1}{2} \bar{a}_{ij} P_i P_j + \frac{1}{2} \bar{\bar{a}}_{ijkl} P_i P_j P_k P_l + \frac{1}{2} \bar{\bar{\bar{a}}}_{ijklmn} P_i P_j P_k P_l P_m P_n \\ & + \frac{1}{8} \bar{\bar{\bar{a}}}_{ijklmnrs} P_i P_j P_k P_l P_m P_n P_r P_s \\ & + b_{ijkl} \varepsilon_{ij} P_k P_l + \frac{1}{2} c_{ijkl} \varepsilon_{ij} \varepsilon_{kl} + f_{ijklmn} \varepsilon_{ij} \varepsilon_{kl} P_m P_n + g_{ijklmn} \varepsilon_{ij} P_k P_l P_m P_n \\ & - \frac{1}{2} \kappa_o E_i E_i - E_i P_i \end{aligned} \tag{4.26}$$

where the stresses, electric displacements and micro-forces are derived as

$$\sigma_{ij} = \frac{\partial h}{\partial \varepsilon_{ij}},\ D_i = -\frac{\partial h}{\partial E_i},\ \xi_{ij} = \frac{\partial h}{\partial P_{i,j}} \ and \ \eta_i = \frac{\partial h}{\partial P_i}. \tag{4.27}$$

Then given all the above equations a variational statement of the principle of virtual work can be written as

$$\int_V \beta_{ij}\dot{P}_j\,\delta P_i\,dV + \int_V \rho\ddot{u}_i\,\delta u_i\,dV + \int_V \sigma_{ij}\,\delta\varepsilon_{ij} - D_i\,\delta E_i + \eta_i\,\delta P_i + \xi_{ij}\,\delta P_{i,j}\,dV = \int_V b_i\,\delta u_i - q\,\delta\phi + \gamma_i\,\delta P_i\,dV + \int_S t_i\,\delta u_i - \omega\,\delta\phi + \xi_{ji}n_j\,\delta P_i\,dS \tag{4.28}$$

Equation (4.28) is the foundation for the derivation of the finite element equations for the phase-field model. Again, the components of mechanical displacement, electric polarization and the electric potential are used as nodal degrees of freedom. The strain, electric field and polarization gradient are derived within the elements, and finally the stress, electric displacement and micro-forces are computed via Equation (4.27). We note that even though polarization gradient appears in the free energy, C^o continuous elements are in fact suitable for the solution. This is a fortuitous consequence of Equation (4.8), given that both electric field and polarization can be taken as independent variables. Therefore, the polarization components take the same status as mechanical displacement and electric potential and the polarization gradient takes the same status as strain and electric field. If, for example, the electric field were the order parameter, then higher order elements would be required in the formulation.

Again, each node in the finite element mesh has mechanical displacement, polarization and electric potential degrees of freedom. Then, defining the array of degrees of freedom as $\mathbf{d}$, each of the field quantities are interpolated from the nodal quantities with the same set of shape functions such that

$$\begin{Bmatrix} u_i \\ \phi \\ P_i \end{Bmatrix} = [N]\{d\} \tag{4.29}$$

The shape function matrix **N** must meet all of the requirements for standard C^o continuous elements. Hence, the displacements, electric potential and polarization components are approximated by continuous functions throughout the mesh, but strains, electric fields, and polarization gradients will have jumps in certain components along element boundaries. The discretized formulas for the polarization rates and the basic solution fields during a given time step are as follows,

$$\dot{P}_i = \frac{P_i^{t+\Delta t} - P_i^t}{\Delta t}, \tag{4.30}$$

and

$$\begin{aligned} u_i &= \alpha u_i^{t+\Delta t} + (1-\alpha) u_i^t, \\ \phi &= \alpha \phi^{t+\Delta t} + (1-\alpha) \phi^t, \\ P_i &= \alpha P_i^{t+\Delta t} + (1-\alpha) P_i^t. \end{aligned} \tag{4.31}$$

Here, the superscript indicates the time step at which the field is evaluated and α is a parameter between 0 and 1 that describes how the solution fields are interpolated in time during a given time step. When $\alpha = 0$ the first order accurate forward Euler integration scheme is recovered, $\alpha = 1$ represents the first order accurate backward Euler scheme that allows for enhanced numerical stability with larger time increments, and $\alpha = 0.5$ is the second order accurate Crank-Nicholson method.

Given a known set of nodal degrees of freedom at time t, when the finite element interpolations of Equation (4.29) and the time integration approximations of Equations (4.30) and (4.31) are substituted into Equation (4.28), a set of nonlinear algebraic equations results for the nodal degrees of freedom at $t+\Delta t$ that can be written in the form

$$\mathbf{B}\left(\mathbf{d}^{t+\Delta t}\right)=\mathbf{F}. \tag{4.32}$$

These equations are solved with the Newton-Raphson method:

$$\left.\frac{\partial \mathbf{B}}{\partial \mathbf{d}}\right|_{\mathbf{d}_i^{t+\Delta t}} \Delta \mathbf{d}_i = \mathbf{F}-\mathbf{B}\left(\mathbf{d}_i^{t+\Delta t}\right), \tag{4.33}$$

where i is the current step counter in the Newton-Raphson sequence and $\Delta \mathbf{d}_i$ is the increment computed for $\mathbf{d}_i^{t+\Delta t}$ such that $\mathbf{d}_i^{t+\Delta t}=\mathbf{d}_i^{t+\Delta t}+\Delta \mathbf{d}_i$. The Newton-Raphson procedure is carried out until a suitable level of convergence is obtained yielding a solution for the displacement, electric potential, and polarization fields at time step $t+\Delta t$. With this new set of known nodal degrees of freedom in hand, the next time increment is computed by solving the updated form of Equation (4.32).

Local incompatibilities in the strain and polarization across the needle tips require relaxation before the equilibrium spatial distribution of the order parameter is reached. In our calculations the first term in (4.28) is initially nonzero, allowing the structure to evolve along non-equilibrium paths and is gradually reduced and set to zero at equilibrium.

4.3. NEEDLE DOMAINS IN $BaTiO_3$ SINGLE CRYSTALS

As discussed in chapter one, ferroelectric behavior is directly linked to the formation of domain patterns upon cooling through the Curie temperature. Different domains have different polarization and strain orientations with respect to the applied loading and the evolution of the favored domains through domain wall motion plays an important role in the polarization reversal process. Domain formation and evolution is linked to energy minimization of the crystal under global and local mechanical and electric compatibility constraints between the regions of homogeneous spontaneous polarization.

Experimental imaging of freestanding ferroelectric single crystals often reveals wedge or needle shaped domains of a compatible polarization variant coexisting within a larger parent domain variant. Such domain patterns for a $BaTiO_3$ single crystal plate are shown in Figure 4.3.1 where ordered arrays of compatible 90^0 laminar domains terminate within the crystal. The shape of the domain at the point of termination in the homogeneous parent phase is needle-like. Figure 4.3.1a shows closely spaced needle domains with polarization perpendicular to the parent variant with tips aligned at 45^0 with respect to the crystallographic axes. In Figure 4.3.1b another hierarchical pattern is presented where widely separated needles with polarization perpendicular to the parent phase meet with needles of perpendicular orientation and opposite polarization. The needle tips in this case are aligned along the direction of the polarization of the parent phase. Another pattern analyzed in this chapter is the case where 90^0 needle domains meet at 180^0 creating an antiparallel array of needles with the same polarization as shown on the bottom right corner of Figure 4.3.1b.

To model such patterns we consider an infinite array of needle domains of equal size and volume fraction under generalized plane strain conditions. Due to similarities in

their properties and analysis the needle domains meeting at 90^0 and 180^0 will be considered in a separate section from the single needle domain comb. Details on the modeling and the results of the simulations are presented next.

(a)

(b)

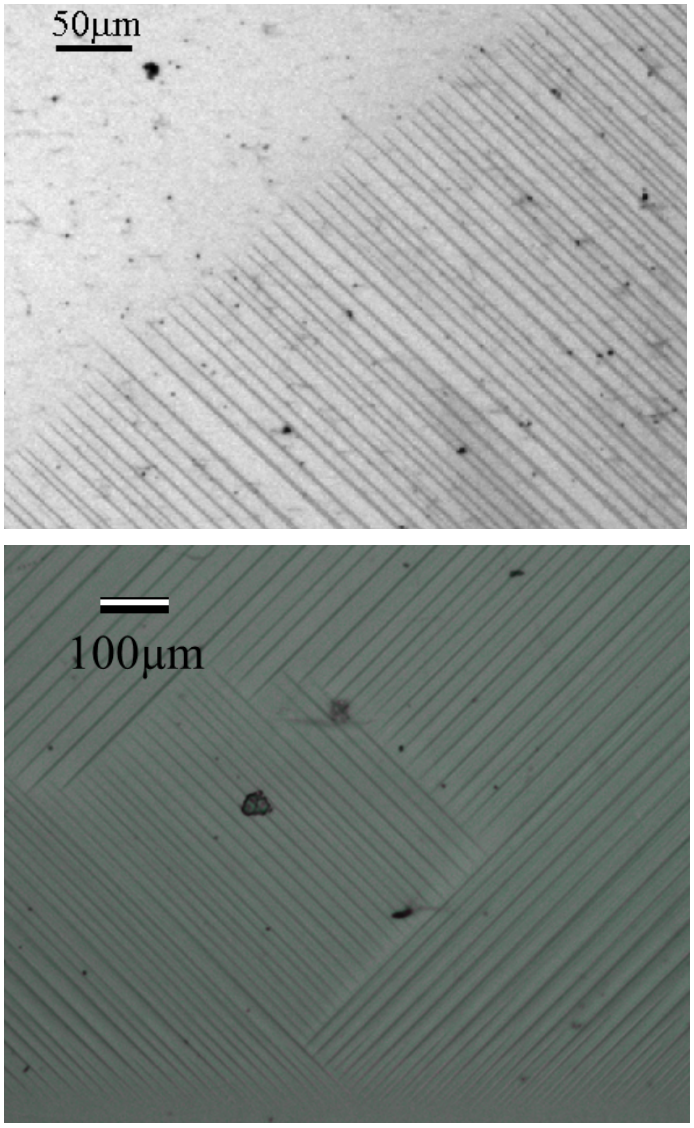

Figure 4.3.1 Optical micrographs of different magnification of a $BaTiO_3$ single crystal showing ordered 90^0 needle domain patterns. a) Closely packed parallel needles tips aligned at 45^0 with respect to the crystallographic axes. b) Widely separated perpendicular and anti-parallel needles with tips aligned along the crystallographic axes (Courtesy of John Huber).

4.4 BALANCED NET CHARGE NEEDLE ARRAYS

We first analyze needle array patterns observed in $BaTiO_3$ single crystals that form balanced net charge configurations. One case of such a pattern is formed by perpendicular 90^0 needle domains of opposite polarization and was introduced in Figure 4.3.1b. A second configuration found in the crystal is that of anti-parallel needle domains, formed by 90^0 domains of the same polarization with needle tips in opposite directions. Schematics of the idealized configurations are shown in Figure 4.4.1.

For both cases the domain structure consists of a parent phase polarized along the negative vertical axis and an array of equally spaced and sized needle domains. The sides of the needle domains are nominally compatible 90^o domain walls. The shape of the 90^o domains at the point of termination in the homogeneous phase is needle-like. The coordinate system introduced in the schematic, to represent the polarization orientation of the domains, is aligned with the crystallographic axes along which the material properties used to fit the enthalpy functional are measured. The parent phase is uniformly polarized along the $-y$-direction and the needle domains along the positive and negative x-direction creating 90^o domain walls along the straight parts of the needle domain.

Figure 4.4.1a shows the antiparallel needles polarized along the positive x-axis with tips aligned along the y-direction or at 45^o with respect to the 90^o domain wall orientation. The perpendicular needle array shown in Figure 4.4.1b consists of needles of opposite polarization, with the top needle polarized along the positive x-axis and the bottom needle polarized along the negative x-axis respectively. In this case the needle tips are aligned along the horizontal axis. Both configurations can be analyzed by considering a two-needle periodic unit cell of balanced net charge. The electromechanical conditions imposed to model the representative unit cell of the perpendicular and the anti-parallel needle arrays have many similarities and will be presented in the next section.

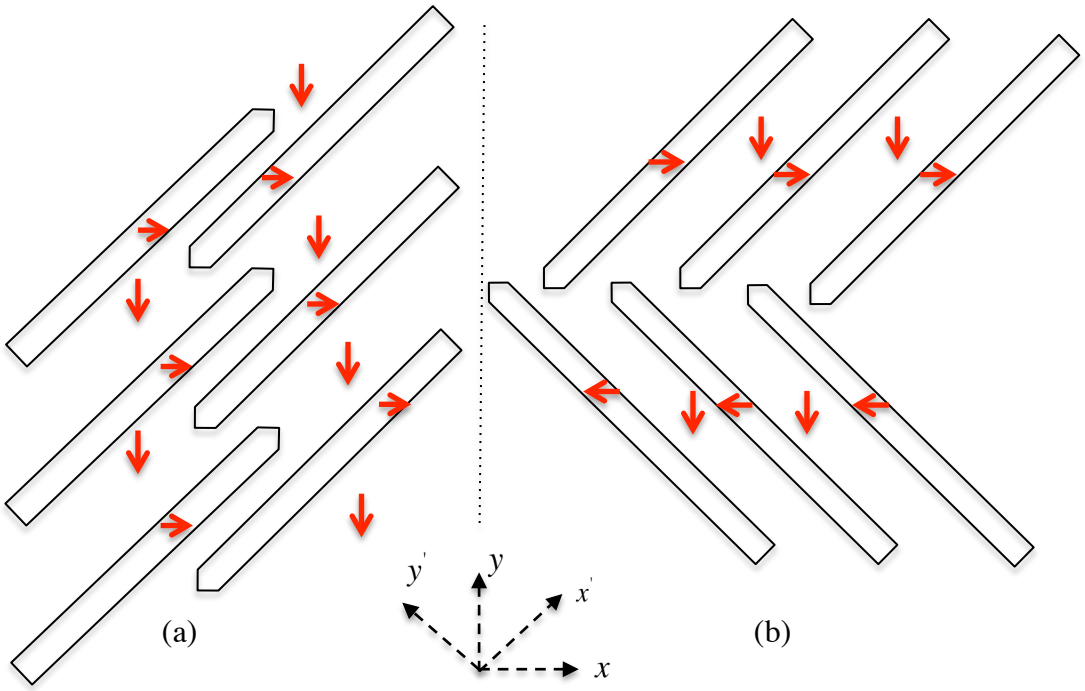

Figure 4.4.1 Schematic of the model of infinite array of equally spaced, perpendicular and antiparallel domain needles of equal volume fraction in uniformly polarized parent phase.

4.4.1 The Periodic Unit Cell

Invoking periodicity of the domain structure of the above configurations, Figure 4.4.2 presents a schematic of the representative cells used to model the infinite arrays of antiparallel and perpendicular pairs of needle domains respectively. In both cases, it is assumed that the unit cell is the result of the electromechanical fitting of the two incompatible domain structures of equal volume also shown in the figure. The total dimensions $b \times h$ of the anti-parallel and the perpendicular unit cells are taken as $800/\sqrt{2}l_0 \times 160\sqrt{2}l_0$ and $400l_0 \times 160l_0$ respectively. Here $l_0 = \sqrt{a_0 P_0 / E_0}$ is the characteristic length scale of the phase-field theory.

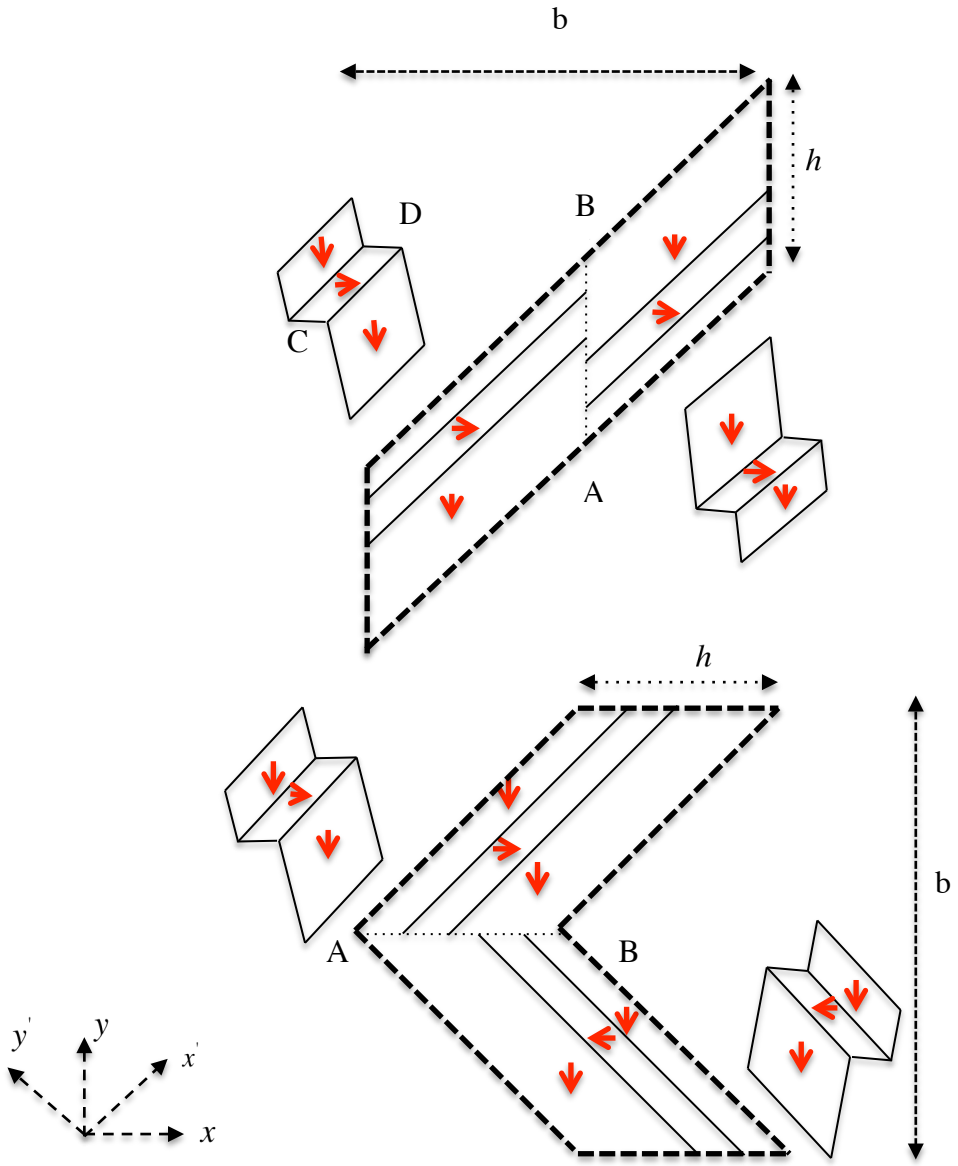

Figure 4.4.2 Schematic of the unit representative cells used to model infinite arrays of a) anti-parallel and b) perpendicular needles. The figure also shows the spontaneous deformation of the two regions fitted together to form the cell.

The corresponding average deformation of the constituent parts can be calculated in terms of the spontaneous strain in the $x-y$ coordinate system. The parent domain on both the left and the right hand side region for the anti parallel needle domains and the

top and bottom for the perpendicular pattern, has a spontaneous polarization $P_x^P = 0,\ P_y^P = -P_o$ and a corresponding spontaneous strain:

$$\begin{aligned} \varepsilon_{xx}^P &= \varepsilon_a, \\ \varepsilon_{yy}^P &= \varepsilon_c, \\ \varepsilon_{xy}^P &= 0. \end{aligned} \tag{4.34}$$

The needle domain has a spontaneous polarization $P_x^N = \pm P_o,\ P_y^N = 0$, with the positive sign referring to the polarization of the top needle of the perpendicular configuration and the negative to the polarization of bottom perpendicular needle. In both cases the spontaneous polarization is accompanied by a deformation field $\varepsilon_{xx}^N = \varepsilon_c,\ \varepsilon_{yy}^N = \varepsilon_a$ and $\varepsilon_{xy}^N = 0$. Then assuming a volume fraction f for the needle domain the average deformation field for the left-right or top-bottom constituent configurations can be written as:

$$\begin{aligned} \varepsilon_{xx}^{av} &= f\varepsilon_c + (1-f)\varepsilon_a, \\ \varepsilon_{yy}^{av} &= f\varepsilon_a + (1-f)\varepsilon_c, \\ \varepsilon_{xy}^{av} &= 0. \end{aligned} \tag{4.35}$$

Here ε_c is the spontaneous deformation of the unit cell due to a spontaneous polarization P_o along the polar, long tetragonal axis and ε_a the corresponding transverse spontaneous stain. For $BaTiO_3$ the strain and polarization values of the spontaneous state are taken as $\varepsilon_c = 0.0082$, $\varepsilon_a = -0.0027$ and $P_o = 0.26 C/m^2$ (Li et al, 1991). Note that mechanical compatibility in terms of the deformation fields is established in an average sense and not pointwise along the common boundary, marked with a doted line along points A and B. Furthermore, the initial polarization distribution is not compatible along the region where

the polarization vectors meet head to head. To allow the fields to evolve towards an electrically and mechanically compatible configuration with lower energy the initially non-zero mobility constant β is gradually reduced until the final stable equilibrium state is reached.

For a coordinate system $x-y$ as shown in Figure 4.4.2, with the origin placed at the midpoint along the common boundary marked with a dashed line between the points A and B, the periodicity of the fields across the points A and B on the bottom and the top surfaces for the antiparallel pattern dictates that:

$$\begin{aligned} u^B &= u^A + \frac{\partial u}{\partial y} h, \\ v^B &= v^A + \frac{\partial v}{\partial y} h, \\ P_x^B &= P_x^A, \\ P_y^B &= P_y^A, \\ \phi^B &= \phi^A + \frac{\partial \phi}{\partial y} h. \end{aligned} \tag{4.36a}$$

Similarly, across the points A and B on the left and right surfaces for the perpendicular pattern we have that:

$$\begin{aligned} u^B &= u^A + \frac{\partial u}{\partial x} h, \\ v^B &= v^A + \frac{\partial v}{\partial x} h, \\ P_x^B &= P_x^A, \\ P_y^B &= P_y^A, \\ \phi^B &= \phi^A + \frac{\partial \phi}{\partial x} h. \end{aligned} \tag{4.36b}$$

Assuming that no overall electric field is applied, the gradient of the electric potential is taken equal to zero. The displacement gradients are computed from the average deformation field of Equation (4.35), setting the rotations equal to zero as $u(x,y)=\varepsilon_{xx}^{av}x$ and $v(x,y)=\varepsilon_{yy}^{av}y$. The periodic boundary conditions of Equations (4.36a) and (4.36b) can then be written as

$$\begin{aligned} &u^B = u^A,\ v^B = v^A + \varepsilon_{yy}^{av}h, \\ &P_x^B = P_x^A,\ P_y^B = P_y^A,\ \phi^B = \phi^A \end{aligned} \tag{4.37a}$$

and

$$\begin{aligned} &u^B = u^A + \varepsilon_{xx}^{av}h,\ v^B = v^A, \\ &P_x^B = P_x^A,\ P_y^B = P_y^A,\ \phi^B = \phi^A. \end{aligned} \tag{4.37b}$$

Given the $x-y$ coordinate system with its origin at the midpoint of the common boundary, the initial conditions for the displacement and the electric potential degrees of freedom, for both the anti-parallel and perpendicular cases can be written as

$$u(x,y)=\varepsilon_{xx}^{av}x,\ v(x,y)=\varepsilon_{yy}^{av}y \text{ and } \phi=0\ \forall\ x,y \tag{4.38}$$

in the unit cell. The polarization initial conditions are better realized on a rotated the coordinate system $x'-y'$ with the x'-coordinate parallel to the 90^0 domain walls or the needle axis. In the rotated system the common boundary for the antiparallel needle array is the line $y'=x'$. Then we have:

$$For\ x' \geq y' \begin{cases} P_x = P_o,\ P_y = 0 \quad for - 50l_0 < y' < -30l_0 \\ P_x = 0,\ P_y = -P_o\ for - 80l_0 < y' < -50l_0\ and\ -30l_0 < y' < 80l_0. \end{cases}$$

$$For\ x' < y' \begin{cases} P_x = P_o,\ P_y = 0 \quad for \quad 30l_0 < y' < 50l_0 \\ P_x = 0,\ P_y = -P_o\ for\ -80l_0 < y' < 30l_0\ and\ 50l_0 < y' < 80l_0. \end{cases} \tag{4.39}$$

Similarly, for the perpendicular case the common boundary in the rotated coordinate system is the line $y' = -x'$ and the initial conditions for the polarization degrees of freedom are written as:

$$For\ x' \geq -y' \begin{cases} P_x = P_o,\ P_y = 0 \quad for \quad 30l_0 < y' < 50l_0 \\ P_x = 0,\ P_y = -P_o\ for\ -80l_0 < y' < 30l_0\ and\ 50l_0 < y' < 80l_0. \end{cases}$$

$$For\ x' < -y' \begin{cases} P_x = P_o,\ P_y = 0 \quad for - 50l_0 < x' < -30l_0 \\ P_x = 0,\ P_y = -P_o\ for - 80l_0 < x' < -50l_0\ and\ -30l_0 < x' < 80l_0. \end{cases} \tag{4.40}$$

Note that the displacements of Equations (4.37a) and (4.37b) corresponding to the spontaneous state of the constituent parts does not account for the domain wall thickness. In order to apply realistic boundary conditions on the side surfaces, we first consider the stress free configurations of the constituent parts of full 90^0 domains shown in Figure 4.4.2. Along the corresponding periodic surfaces the periodic boundary conditions of Equations (4.36a) and (4.36b) are applied. Periodicity is also enforced across the remaining boundaries. These conditions are better realized in a rotated coordinate system with the horizontal axis along the 90^0 domain walls, as shown in Figure 4.4.2. For points C and D on the side surfaces we have:

$$
\begin{aligned}
u^{'D} &= u^{'D} + \frac{\partial u^{'}}{\partial x^{'}} w, \\
v^{'B} &= v^{'A} + \frac{\partial v^{'}}{\partial x^{'}} w, \\
P^{B}_{x^{'}} &= P^{A}_{x^{'}},\ P^{B}_{y^{'}} = P^{A}_{y^{'}},\ \phi^{B} = \phi^{A}.
\end{aligned}
\tag{4.41}
$$

The boundary value problem is then solved with finite elements along non-equilibrium paths to allow for polarization reorientation and formation of the 90^0 domain walls. The displacements and net charge based on the polarization distribution accounting for domain wall thickness are then extracted and used as boundary conditions for the original needle domain problem. More specifically the electric potential is set equal to zero along one of the non-periodic boundaries. The other non-periodic boundary is set to be an equipotential surface and the net charge obtained from the polarization distribution accounting for domain wall thickness is allowed to distribute along the surface as part of the solution. Results of the finite element simulations are presented next.

4.4.1 Equilibrium State of an Infinite Array of Antiparallel Domain Needles

Within the present phase field theory the characteristic length scale is given by $l_0 = \sqrt{a_0 P_0 / E_0}$. As discussed by Su and Landis (2007) the parameter a_0 is important for determining the domain wall thickness and the domain wall surface energy. In the present calculations we take $a_0 = 1 \times 10^{-10} Vm^3 / C,$ unless otherwise specified, yielding a characteristic length of $l_0 \approx 1nm$ (Su and Landis, 2007). To specify the geometry of the representative unit cell the thickness of the needle domain variant enters the problem as a second length scale. Specifying the thickness of the needle variant, the full dimensions of the representative unit cell can be computed for a given relative volume fraction between

the needle and parent domains. For the antiparallel needle case, the needle domains are assumed to initially occupy 12.5% of the total volume of the crystal. The thickness of the needle domains is assumed to be approximately $20l_0$. For the given volume fraction, the thickness of the unit cell is $160l_0$, resulting in alternating domain sizes of $120l_0$ and $20l_0$ for the parent and needle domain variant respectively. The mesh is a structured mesh of eight node quadratic elements varying in size from $0.2-0.5l_0$ to $5-10l_0$. Smaller elements are placed along the straight 90^0 domain walls, between the needle and the parent phase and in regions where the domain walls are expected to move and form the tip, in order to capture the needle domain pattern. Larger elements are placed in regions of homogeneous parent phase away from the domain walls.

Initially, the boundary conditions mentioned in the previous section are applied and the viscous parameter β is gradually reduced to zero until an equilibrium state is found. This is an intermediate step in the analysis to allow the initially rectangular needle domain to evolve to an approximate needle domain. The displacement boundary conditions on the side surfaces accommodate the domain wall thickness of a full rectangular domain. However they are not exactly the corresponding stress-free displacements for a needle domain. As a next step, the above solution with the formed needle tip is used as an initial condition and the displacement boundary conditions from the side surfaces are removed. The side surfaces are now traction free with the electric potential equal to zero on the left hand side. The right hand side surface remains an equipotential surface with a net charge based on the polarization distribution accounting for the domain wall thickness. The full set of periodic boundary conditions is applied on the top and bottom periodic surfaces and a new equilibrium distribution is found.

Figure 4.4.3 shows the contour plots of the polarization components along the horizontal and vertical direction in the deformed configuration. Here, the net charge on

the side boundaries is equal to the net charge based on the polarization distribution accounting for the domain wall thickness. The formation of the needle domains results in a non-uniform polarization distribution of the parent phase especially pronounced for the horizontal polarization component. Note the anti-symmetry of the polarization contour along the vertical direction and the fact that the polarization distribution of the parent phase is charged by almost 10% in regions away from the needle tips compared with the nominal polarization values of the parent variant. This effect of the needle domains on the polarization distribution of the parent phase extends along almost the entire unit cell.

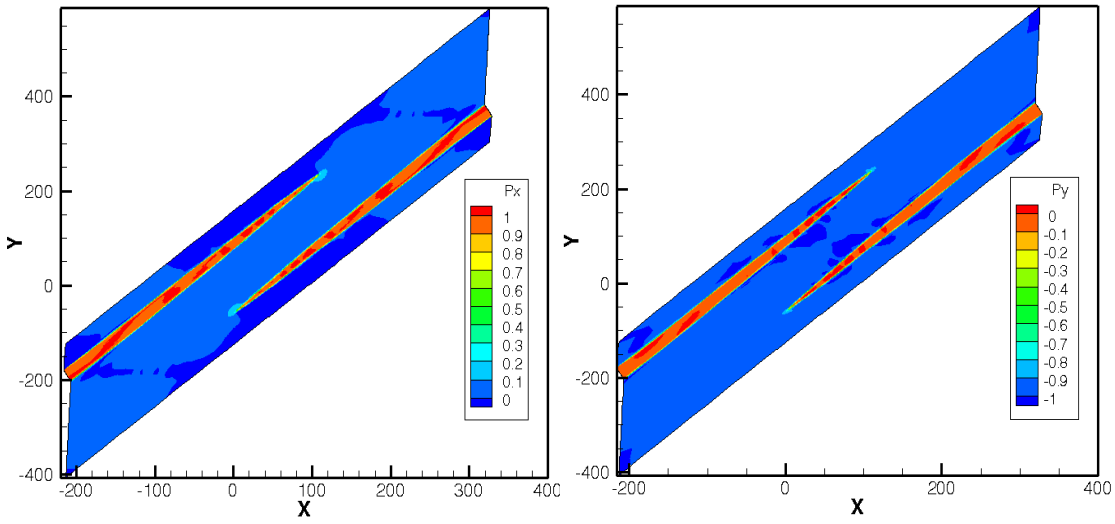

Figure 4.4.3 Deformed configuration of polarization distribution of antiparallel needles of initial volume fraction of 12.5% along the (a) horizontal and (b) vertical direction.

Next, we examine the effect of electrical loading on the anti-parallel array of needles. The net charge on the side surfaces is gradually reduced, resulting in a retraction of the needle domains with respect to each other. In Figure 4.4.4 the net surface charge density is plotted against the average electric field between the side surfaces for a range of loading corresponding to a 40% reduction of net surface charge density. Reducing the

charge on side surfaces results in an almost linear reduction in the potential drop between the side boundaries of the unit cell as it can be seen in Figure 4.4.4. However, for the given range of surface charge, the retraction of the needle tips happens under the effect of a non-zero average electric field between the side boundaries. The marker points from left to right in the Figure correspond to the initial net charge level, taken equal to the net charge based on the polarization distribution accounting for the domain wall thickness and charge reduction by 20% and 40% respectively.

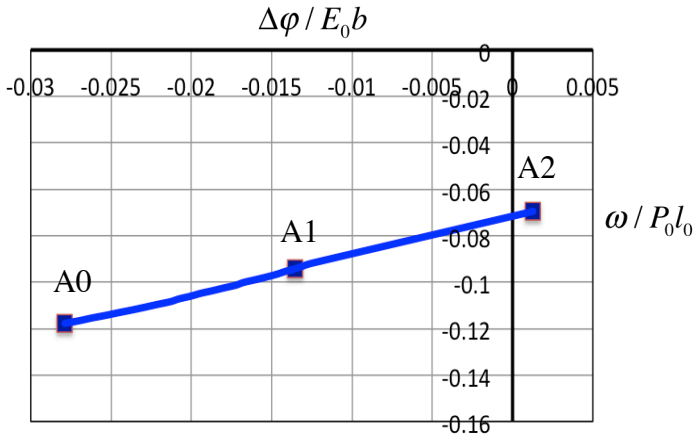

Figure 4.4.4 Net surface charge density plotted against the average electric field between the side surfaces for a range of charge reduction up to 40% from the initial net charge based on the polarization distribution accounting for the domain wall thickness. Marked points A0, A1 and A2 correspond to the initial net charge level and charge reduction by 20% and 40% respectively.

The change in the average electric field and net surface charge across the non-periodic boundaries has an effect on the polarization distribution in the unit cell as well. The polarization distribution along the horizontal direction in the deformed configuration, corresponding to net surface charge levels reduced by 20% and 40% is shown in Figure 4.4.5. It can be seen that the needle domain retraction has a great effect on the polarization distribution of the parent phase in the horizontal direction. The polarization

contours of Figure 4.4.5 show that polarization changes now extend up to half of the length of the needles, localized mostly between the overlapping needle tips. Away from the needle tips along the straight boundaries of the needles the polarization distribution of the parent phase is uniform matching the nominal polarization value. The polarization distribution along the vertical direction for these levels of loading has also changed compared with the distribution shown in Figure 4.4.3. The value of the polarization vertical component matches the nominal polarization and is uniform throughout the unit cell and the contour plots are not shown here, as they are indistinguishable to each other.

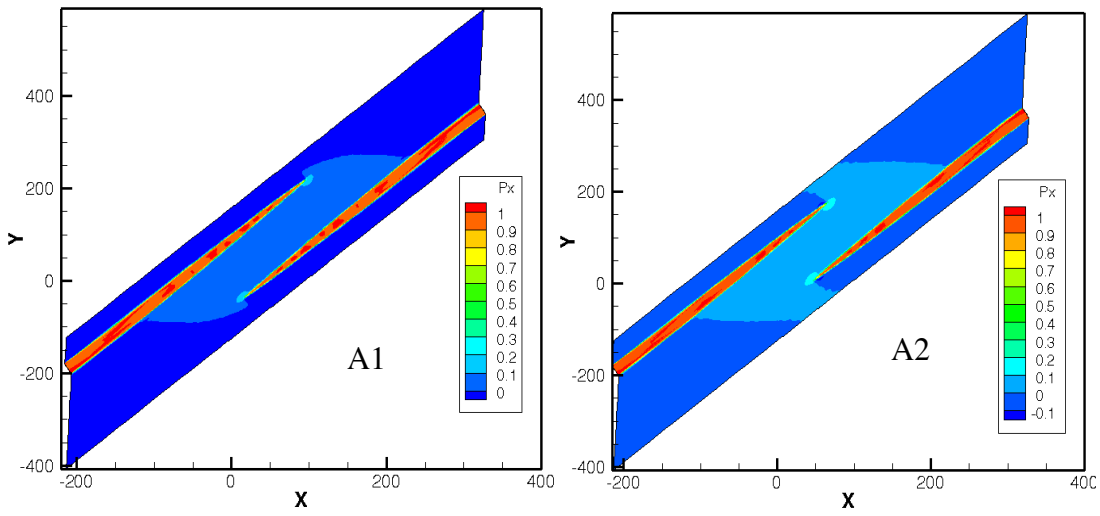

Figure 4.4.5 Deformed configuration of polarization distribution of antiparallel needles of initial volume fraction of 12.5% along the x-direction. The contour plots correspond to net surface charge levels reduced by 20% and 40% shown with marked points A1 and A2 in Figure 4.4.4 respectively.

Figure 4.4.6 presents the variation of the average value of the electric potential between the top and bottom periodic boundaries plotted along the horizontal direction for the three levels of net surface charge density marked in Figure 4.4.4. It is interesting to note that the electric potential experiences a jump due to the needle structure with the pair

of needle tips creating the appearance of a charge dipole in the unit cell and a non-uniform electric field between the needle tips. On the side regions of the unit cell along the straight needle boundaries the electric potential varies continuously. As the straight boundaries start to deviate from the straight line forming the needle tips52, the electric potential experiences a sudden drop followed by a change in the slope as needle tips are approached. For different levels of the net surface charge, the reduction in the average electric field between the side boundaries also results in a change of the slope of the electric potential variation along the sides of the unit cell as can be seen in Figure 4.4.6.

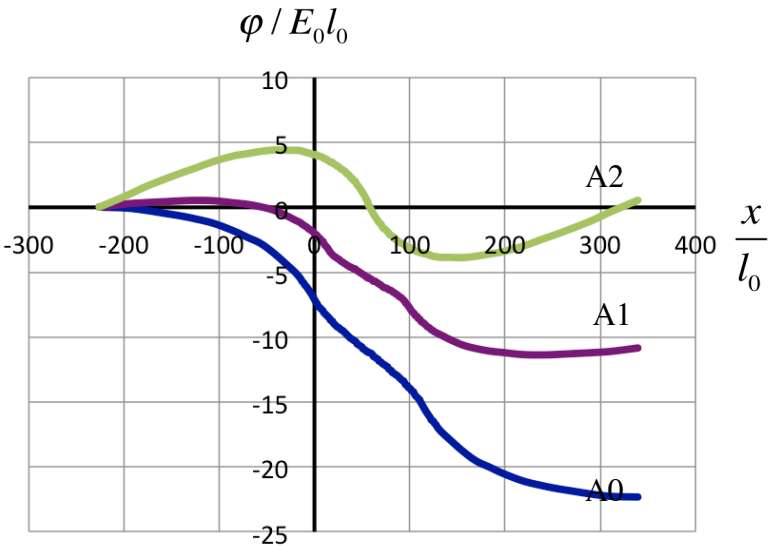

Figure 4.4.6 Average electric potential variation along the horizontal direction. The different colors correspond to different net charge levels on the side boundaries marked in Figure 4.4.4.

Next we examine the needle profiles. Figure 4.4.7 shows the equilibrium needle corresponding to the three levels of loading marked in Figure 4.4.4, plotted on the rotated coordinate system with the horizontal axis along the needle axis. The polarization

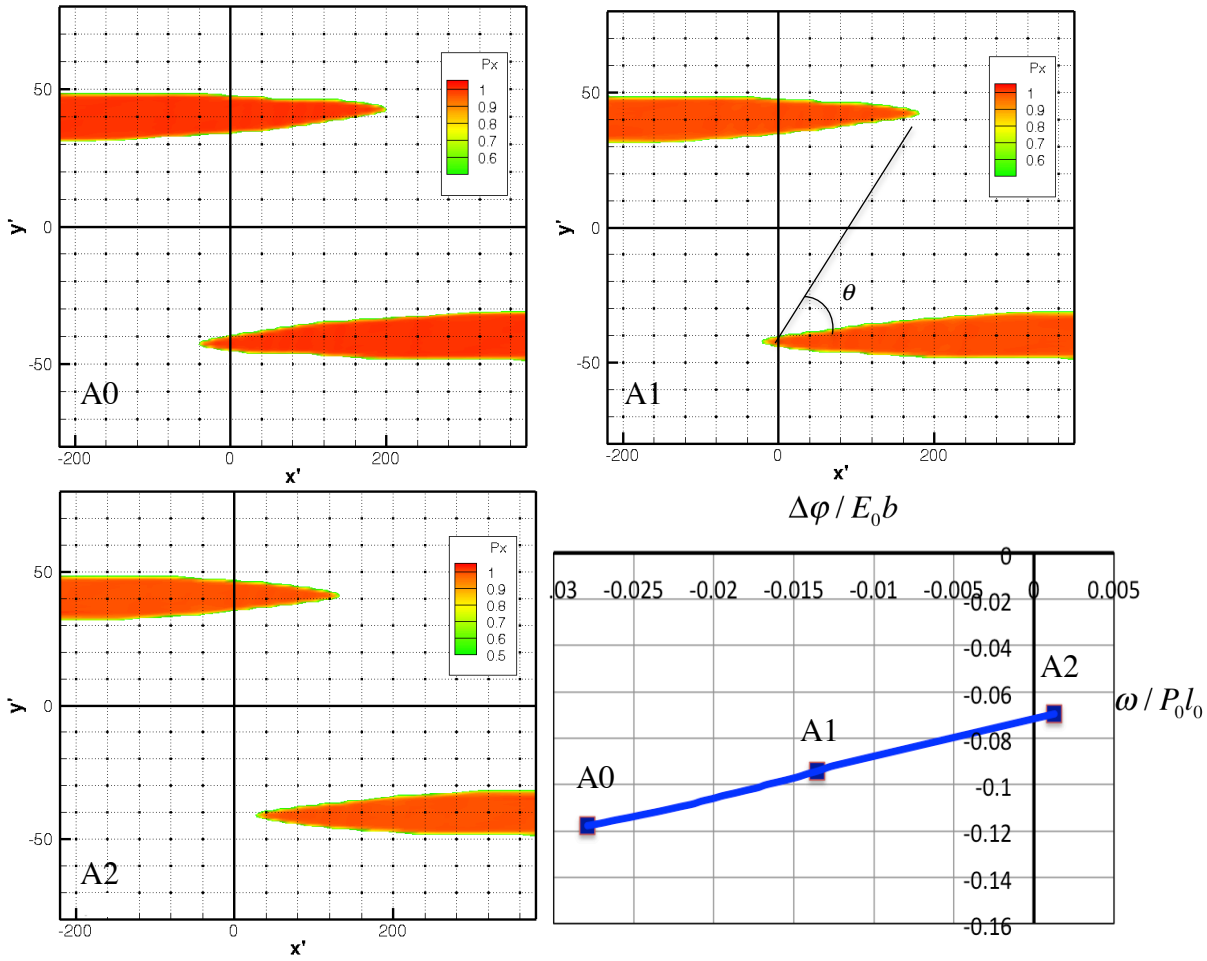

Figure 4.4.7 Needle profiles and evolution of the equilibrium needle tip positions for (a) the full surface charge, corresponding to the relaxed polarization distribution. The charge is then reduced by (b) 20% and (c) 40%. (d) These cases correspond to the marked points on the surface charge density plotted against the average electric field.

contours in the same figure refer to the original coordinate system. The cut-off value of polarization for all needle profiles shown in the figure is chosen $P_x = 0.5P_0$. The needle tip profile is asymmetric with respect to the needle axis. The needle tip surface in the region between the needle pair shows a higher curvature than the outer surfaces of the needle pair. Also note that the initial position of the needle domains is taken such that no

overlapping region between the needle domains exists. However the equilibrium position of the needle tips shows overlapping of the needle tips and deviation from the assumed 45^o with respect to a coordinate system with the horizontal axis along the domain walls. The needle tips form a 70^o angle when the tip is identified at polarization levels of $P_x = 0.5P_0$. Upon loading the needle profiles show a self-similar retraction of the needle tips as the potential drop between the side boundaries decreases. The needle tips evolve through the motion of the needle tip without a significant reduction of their width, changing their relative position. For the two limit cases A0 and A2 of Figure 4.4.4 the distance between the needle tips changes from $241l_0$ to $126l_0$. The angle between the needle tips is 70^0, 66^0 and 42^0 for the cases A0, A1 and A2 shown in the Figure 4.4.7.a-c. The asymmetry in the needle profile and the non-uniform distribution of the polarization between the needles is a consequence of the non-uniform field along the vertical direction between the needles.

4.4.2 Equilibrium State of an Infinite Array of Perpendicular Domain Needles

Next we proceed in the presentation of the simulation results for the perpendicular needle domain pattern. As in the antiparallel needle case, the needle domains are assumed to initially occupy 12.5% of the total volume of the crystal. For alternating domain sizes of approximately $120l_0$ and $20l_0$ for the parent and needle domain variant the representative unit cell is formed by fitting two constituent regions of equal size and equal needle volume fraction and has total dimensions of $400l_0 \times 160l_0$. Full periodic boundary conditions are applied along the left and right boundaries. As before, we first allow the needle domains to reach equilibrium by fixing the displacement on the top and bottom boundaries to the displacements and the net charge based on the polarization distribution corresponding to the fully developed domain walls. This solution is used as

an initial condition when the displacement boundary conditions from the non-periodic boundaries are removed. The top and bottom boundaries of the unit cell are now traction free .The electric potential set to zero on the top surface and the bottom surface set to an equipotential surface with net charge based on the polarization distribution corresponding to the fully developed domain walls.

Figure 4.4.8a shows a contour plot of the polarization component along the $x-$ direction in the deformed configuration. The polarization contours show a non-uniform polarization distribution in the parent phase that is highly localized in a relatively thin region surrounding the needle tips. This was not the case with the antiparallel needle configuration where the effect of the interaction of the needle tips on the polarization distribution extended through almost the entire unit cell for the initial net charge level. Also note that although the effect of the needle tips is localized in the perpendicular case it is also more intense compared to the antiparallel needle configuration. The polarization contour of Figure 4.4.8a shows alternating levels of $P_x = \pm 0.5 P_0$ polarization in the region surrounding the needle tips. The contour plot of the polarization distribution along the vertical direction is highly uniform and is not presented here.

Next, in order to investigate the range of stable equilibrium positions of the needle structure we proceed as in the case of antiparallel needles by electrically loading the array of perpendicular needles. Note that the electric potential is set to zero on the top surface in this case. For the needles to retract the net surface charge on the bottom surface is increased gradually leading to an increase on the electric potential on the bottom boundary and a retraction of needles with respect to each other. The variation of the net surface charge density against the average electric between the top and bottom surfaces is shown in Figure 4.4.8d. The marked points correspond to the initial net charge level, based on the polarization distribution accounting for the thickness of the domain walls,

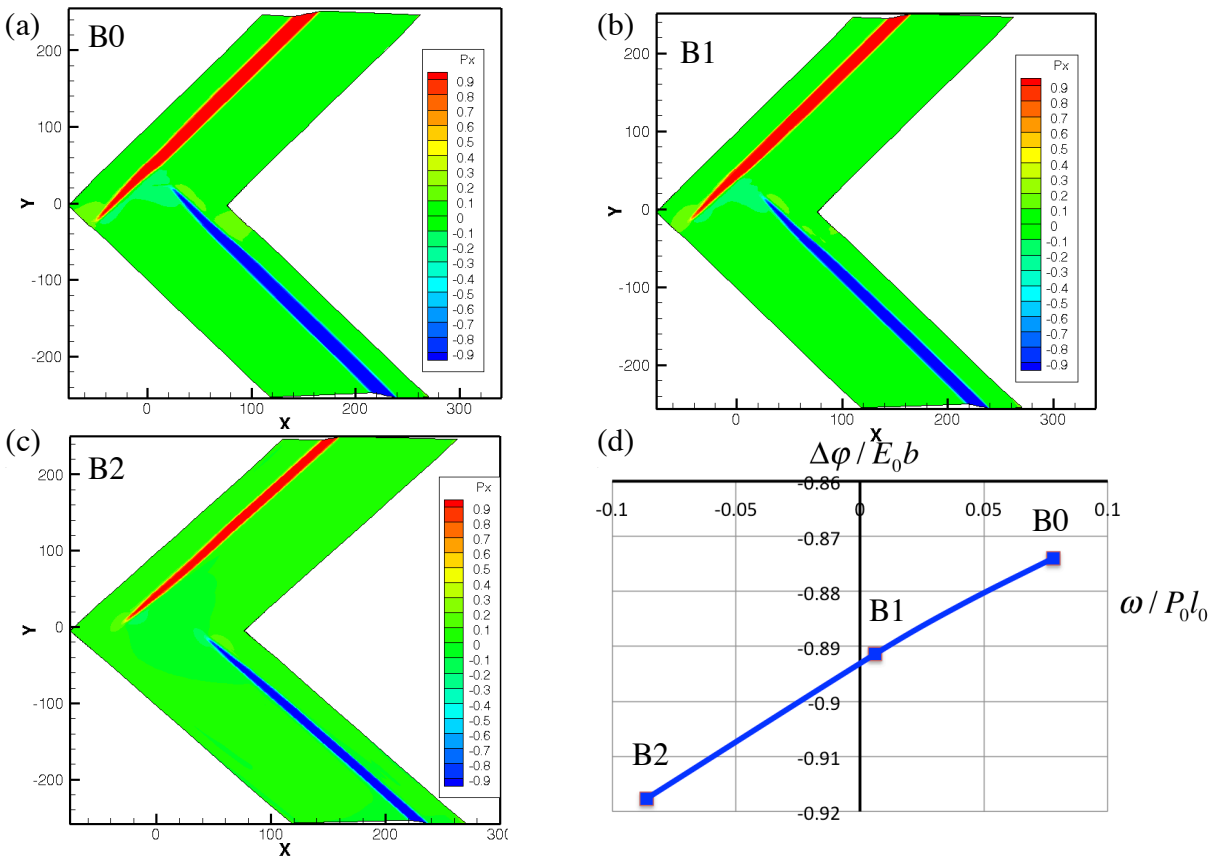

Figure 4.4.8 Deformed configuration of polarization distribution of perpendicular needles of initial needle volume fraction of 12.5%. (a) The surface charge initially is based on the polarization distribution, and then increased gradually. (d) Surface charge density plotted against the average electric field. (b) and (c) correspond to charge reduction by 2% and 5%.

and an increase on the net charge on the top and bottom surfaces by 2% and 5% respectively. The polarization distribution for these cases is also shown in Figure 4.4.8b-c. Changes in the polarization values are even more localized around and between the needle tips with increasing surface charge. In fact, for 5% increase on the surface charge polarization changes are only restricted around the needle tips.

Figure 4.4.9 shows the variation of the average value of the electric potential along the periodic boundaries of the unit cell plotted on the vertical direction. It is interesting to note that as in the antiparallel case the needle tips appear to behave as a boundary that creates a potential drop across it. For the net surface charge levels marked with B0 and the B1 in Figure 4.4.8d corresponding to the initial net charge and a 2% increase respectively, the electric potential exhibits a change in the slope on the region between the needle tips indicating the non-uniform electric field caused by the interaction of the needle tips. This plateau does not appear for further increase on the net charge and followed by a relative retraction of the needle tips. Also, as needle domains retract and with increasing values of the net surface charge, the slope of the electric potential variation away from the needle tips changes.

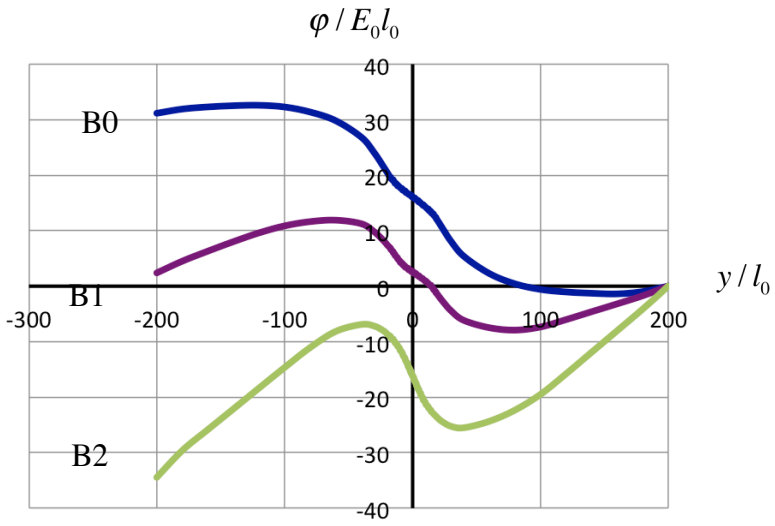

Figure 4.4.9 Average electric potential variation along the vertical direction. The different colors correspond to different net charge levels on the top and bottom surfaces marked in Figures 4.4.7d and 4.4.8d.

Finally, the corresponding needle profiles along the rotated coordinate system for these cases are shown in Figure 4.4.10. As with antiparallel case no initial overlap of the

needle tips was introduced. However, we note a relative overlap of about $60l_0$. The needle profile at the tip is more symmetric with respect to the needle axis compared to the needle profiles of the anti-parallel case. In contrast to the antiparallel case the needle tip consists of mostly straight parts with no significant curvature and the extension of the needle the tip along the needle axis is less pronounced.

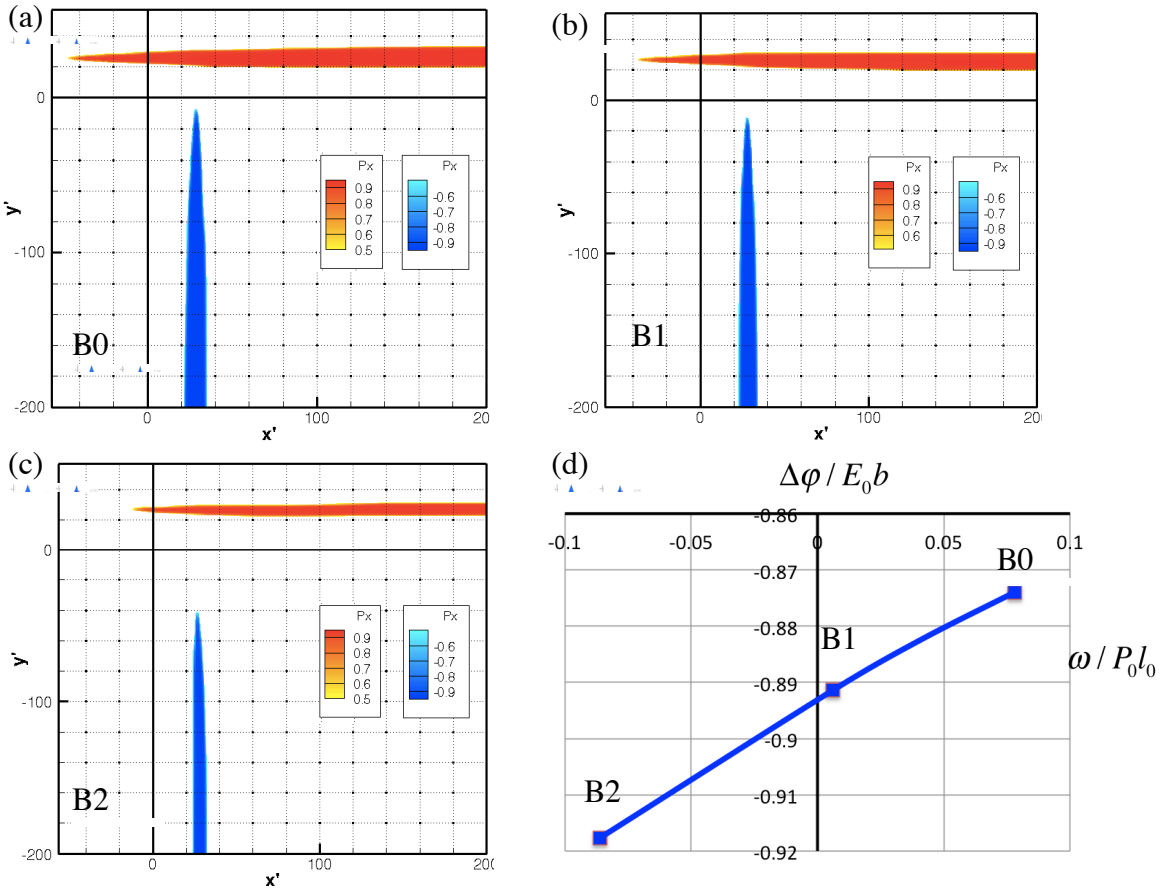

Figure 4.4.10 Needle profiles and evolution of the equilibrium needle tip positions for (a) the full surface charge, corresponding to the relaxed polarization distribution. The charge is increased by (b) 2% and (c) 5%. (d) These cases correspond to the marked points on the surface charge density plotted against the average electric field.

The needle profiles at increased levels of surface charge are shown in Figure 4.4.10b-c. The needles retract in a self-similar way as for the antiparallel case where both needle tips retracted at approximately the same rate. However, the evolution of the perpendicular needles differs from the evolution of the antiparallel needles were the evolution was due to the tip motion. Here, the needle tip motion is followed by lateral motion of the straight parts of the needle introducing a new evolution mechanism for the needle domain structure.

4.5. The Infinite Array of Parallel Needle Domains

The last domain structure analyzed is that of a parallel array of equally spaced and sized parallel needle domains as shown in Figure 4.5.1. The parent phase is uniformly polarized along the $-y$ direction and the needle domain along the x direction creating 90^o domain walls along the straight sides of the needle domain.

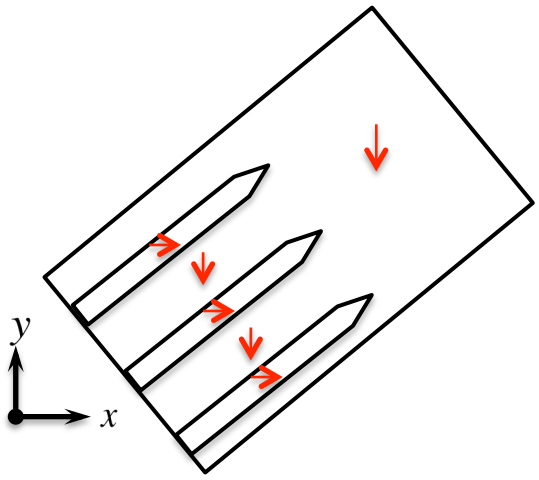

Figure 4.5.1 Schematic of the model infinite array of equally spaced parallel domain needles of equal volume fraction.

Invoking periodicity, Figure 4.5.2 presents a schematic of the representative cell of the model of the infinite array of needle domains. It is assumed that the unit cell is the

result of the electromechanical fitting of the two incompatible domain structures of equal volume also shown in the figure. The corresponding average deformation of the constituent parts can be calculated in terms of the spontaneous strain in the xy coordinate system. The parent domain on the right hand side region has uniform spontaneous polarization $P_x^{Right} = 0,\ P_y^{Right} = P_0$ and a corresponding average strain

$$\begin{aligned} \varepsilon_{xx}^{av,Right} &= \varepsilon_a, \\ \varepsilon_{yy}^{av,Right} &= \varepsilon_c, \\ \varepsilon_{xy}^{av,Right} &= 0. \end{aligned} \tag{4.42}$$

The needle domain has a uniform spontaneous polarization $P_x^N = P_s,\ \mathrm{P}_y^N = 0$, accompanied by a deformation field $\varepsilon_{xx}^N = \varepsilon_c,\ \varepsilon_{yy}^N = \varepsilon_a$ and $\varepsilon_{xy}^N = 0$ respectively. Then assuming a volume fraction f for the needle domain the average deformation field for the left hand side configuration is

$$\begin{aligned} \varepsilon_{xx}^{av,Left} &= f\varepsilon_c + (1-f)\varepsilon_a, \\ \varepsilon_{yy}^{av,Left} &= f\varepsilon_a + (1-f)\varepsilon_c, \\ \varepsilon_{xy}^{av,Left} &= 0. \end{aligned} \tag{4.43}$$

Mechanical compatibility dictates the orientation of the common boundary, marked with a doted line along points A and B in the unit cell schematic as

$$\begin{aligned} &\Delta\varepsilon_{ij} n_i n_j = 0 \Rightarrow f(\varepsilon_c - \varepsilon_a)\left(\sin^2\theta - \cos^2\theta\right) = 0 \\ &\rightarrow \theta = \pi/4, \end{aligned} \tag{4.44}$$

where n_i are the components of the unit vector along the boundary from point A to B and θ is the angle between the unit normal and the y axis. Then mechanically fitting the two domains along the line $y = -x$, with the appropriate periodic boundary conditions is better realized on a coordinate system rotated by the angle θ with the x' axis normal to the boundary.

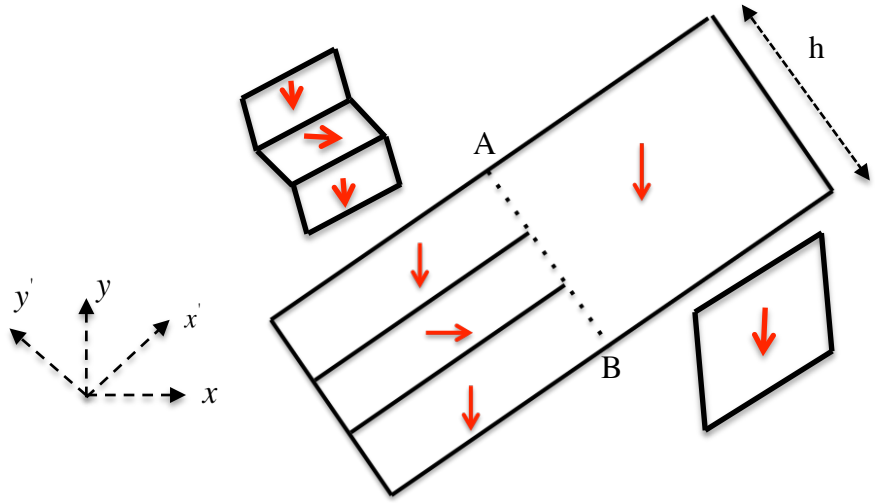

Figure 4.5.2 Schematic of the unit representative cell used to model an infinite array of needles showing the assumed spatial distribution of polarization specifying the initial domain structure. The figure also shows the spontaneous deformation of the two regions fitted together to form the cell.

Periodicity of the fields across the points A and B on the bottom and the top surfaces dictates that

$$
\begin{aligned}
u_{x'}^{B} &= u_{x'}^{A} + \frac{\partial u_{x'}}{\partial y'} h \\
u_{y'}^{B} &= u_{y'}^{A} + \frac{\partial u_{y'}}{\partial y'} h \\
P_{x'}^{B} &= P_{x'}^{A} \\
P_{y'}^{B} &= P_{y'}^{A} \\
\phi^{B} &= \phi^{A} + \frac{\partial \phi}{\partial y'} h
\end{aligned}
\tag{4.45}
$$

Assuming that no electric field is applied, the gradient of the electric potential is taken equal to zero and the displacement gradients are computed by transformation of the average deformation fields (4.42) and (4.43). In the rotated coordinate system yields a displacement field is of the form

$$
\begin{aligned}
u_{x'} &= \frac{(\varepsilon_c + \varepsilon_a)}{2} x', \\
u_{y'} &= \frac{(\varepsilon_c + \varepsilon_a)}{2} y' + (\varepsilon_c - \varepsilon_a)(1 - 2f) x',
\end{aligned}
\tag{4.46}
$$

where $f = 0$ for the right hand side region. Note that the displacement field is continuous along the boundary AB and the rotation $\frac{\partial u_{x'}}{\partial y'}$ has been set equal to zero.

Transforming back to the original coordinate system the periodic boundary conditions (4.45) reads as

$$
\begin{aligned}
u_x^B &= u_x^A - \frac{(\varepsilon_c + \varepsilon_a)}{2}\frac{h}{\sqrt{2}}\ , \\
u_y^B &= u_y^A + \frac{(\varepsilon_c + \varepsilon_a)}{2}\frac{h}{\sqrt{2}}, \\
P_x^B &= P_x^A, \quad P_y^B = P_y^A, \quad \phi^B = \phi^A.
\end{aligned}
\tag{4.47}
$$

Finally, the initial displacement conditions satisfying the average mechanical compatibility used in all calculations are readily computed by a transformation of the displacements (4.46). The polarization and electric potential initial conditions are written as:

$$
\begin{aligned}
&For\ x' < -y' \begin{cases} P_x = P_o,\ P_y = 0 \quad for \quad |y'| \le y'_{needle} \\ P_x = 0,\ P_y = -P_o\ for\ -y'_{bottom} < y' < -y'_{needle}\ and\ y'_{needle} < y' < y'_{top}. \end{cases} \\
&For\ x' \ge -y' \ \begin{cases} P_x = 0,\ P_y = -P_o\ for - y'_{bottom} < y' < y'_{top}. \end{cases} \\
&\phi = 0\ \forall x', y'.
\end{aligned}
\tag{4.48}
$$

The initial polarization distribution is not compatible along the region where the polarization vectors form a head to head domain wall. To allow the polarization to evolve towards an electrically compatible configuration with lower energy the initially non-zero polarization viscosity constant β is gradually reduced until the equilibrium stable state is reached.

4.5.1 Fixed Boundary Conditions - A First Approximation by Stabilizing a Single Needle.

As a first approximation towards the modeling of an infinite array of needles we investigate the existence of a single needle by fixing the displacements on the boundary

corresponding to the periodic boundary conditions (4.47) and the electric potential equal to zero on the top and bottom surfaces of the unit cell. The polarization vector is also fixed to the initial value given from Equation (4.48). The left and right hand side boundaries are traction free and a surface charge distribution corresponding to the polarization is applied.

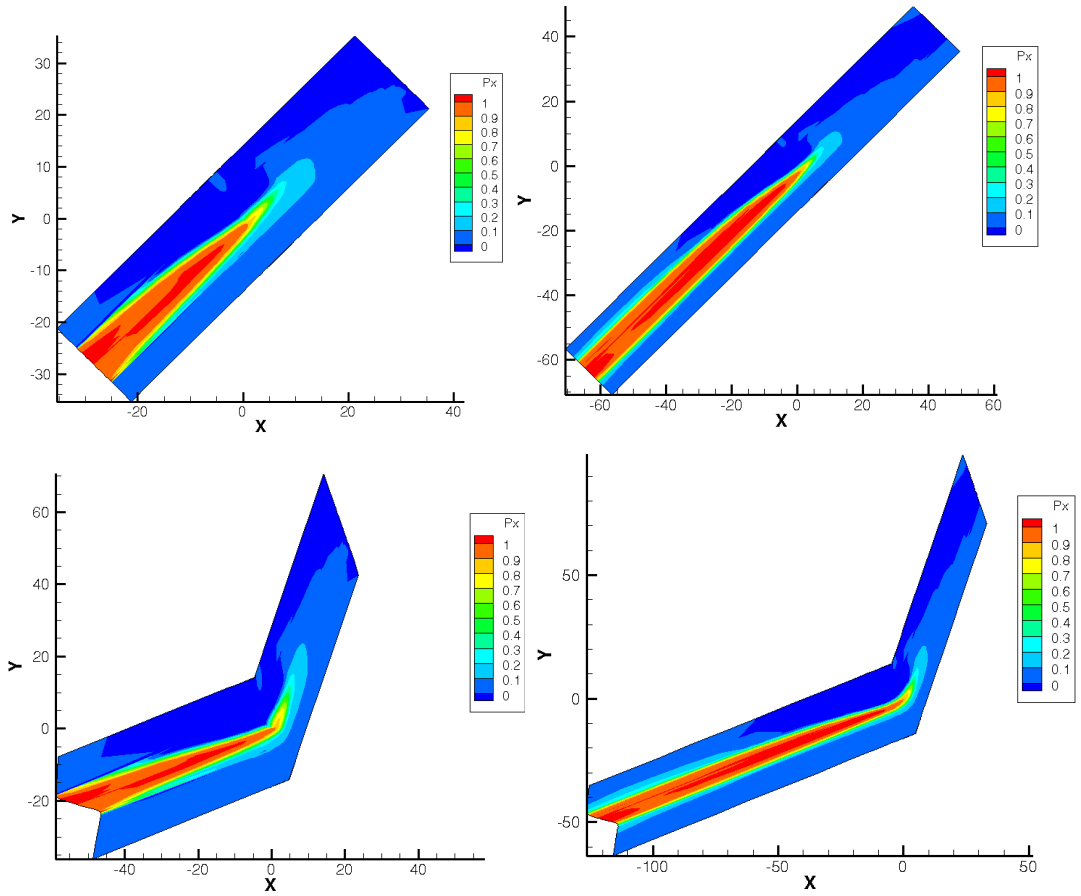

Figure 4.5.3 Un-deformed and deformed configurations of polarization distribution for two different cell sizes, a) $80\times 20l_0$ formed by fitting the two regions of equal volume and b) formed by fitting a $90\times 20l_0$ and a $60\times 20l_0$ region for the left and right hand side constituent configurations respectively. The needle initially occupies 50% of left hand side region.

Figure 4.5.3 shows the contour plots of the polarization component along the $x-$ direction for an initial needle domain volume fraction of 50% of the left hand side region for two different unit cell lengths. In Figure 4.5.3a the unit cell of dimensions $80\times 20l_0$ is formed by fitting two regions of equal volume. In Figure 4.5.3b the left hand side region is $90\times 20l_0$ as apposed to $60\times 20l_0$ for the right hand side constituent configuration. The relative volume difference of the uniform parent domain region to the region containing the needle does not have a large effect on the position and the profile of the needle tip.

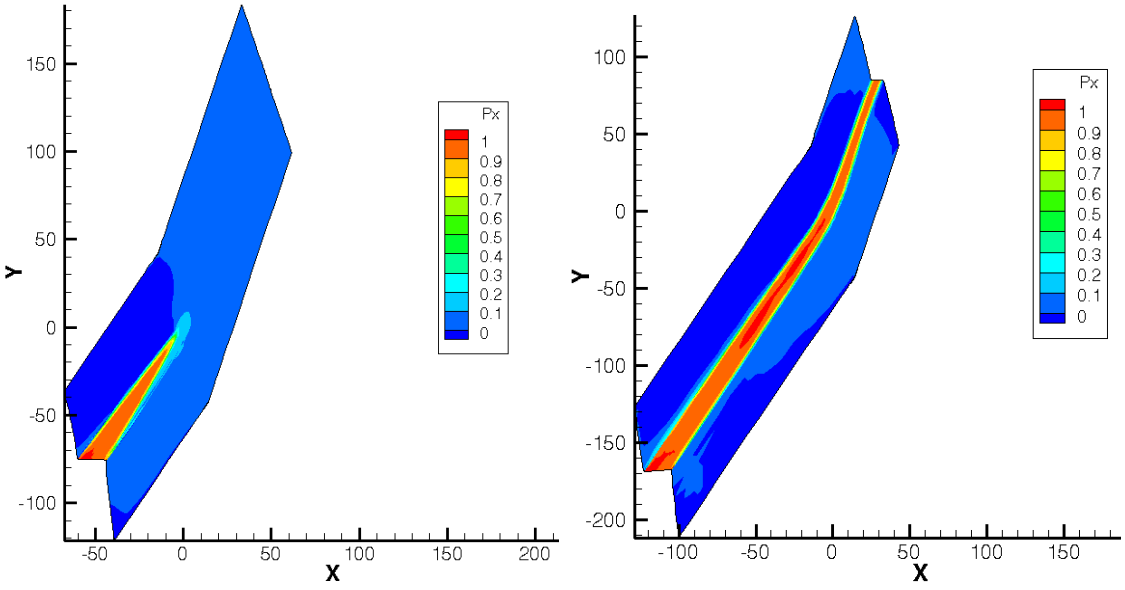

Figure 4.5.4 Effect of relative volume difference between the two constituent regions and the overall needle length. All boundary conditions of Figure 4.5.3 are maintained except the surface charge distribution is replaced with fixing the electric potential equal to zero.

The main difference concerns the overall profile of the needle domain. The shorter needles tend to have a wedge-like shape while in the case of longer needles straight 90^0 domain walls are maintained up to one half of the overall length. The effect of relative volume difference and the overall length of the needle are especially

pronounced in the behavior of the needle under electrical loading. Figure 4.5.4 shows this behavior when the electric potential is fixed to zero on the right hand side surface. All other boundary conditions are the same as reported above. We see that the longer needle is attracted by the grounded surface and eventually evolves to a compatible domain. On the contrary the shorter wedge evolves into a thinner needle and maintains stability under the same boundary conditions. The effect of the initial volume fraction of the needle domain relative to the left hand side part is also important. Corresponding calculations of needle volumes of 0.25 and 0.125 show that the needle domain retracts to the left by motion of the needle tip and is completely diffused away in a self similar fashion, except very close to the left hand side boundary surface where is restricted by the applied charge.

4.5.2 Relaxed Boundary Conditions – An Infinite Array of Needles.

As a next step in the modeling of an infinite array of needle domain the fixed boundary conditions on the top and bottom surfaces are relaxed by gradually replacing them with the periodic boundary conditions (4.47) for one by one of the degrees of freedom and using the previous equilibrium state as an initial solution for the next. For traction free side boundaries, full relaxation of all five degrees of freedom according to the periodic boundary conditions will result in almost complete elimination of the needle when charge is applied on the right and left boundaries and to evolution of the needle to a full domain when the electric potential is fixed to zero on the right hand side.

Sole relaxation of the polarization components according to the periodic boundary conditions along the top and bottom boundaries has the least effect and all above results remain quantitatively the same. Relaxing the electric potential in addition to the polarization degrees of freedom while maintaining the displacements components fixed

has a stronger destabilizing effect. For example, relaxing these conditions in the short needle case in Figure 4.5.3 will also results in evolution of the needle to a full domain towards the right hand side as in the case of the long needle in the same figure.

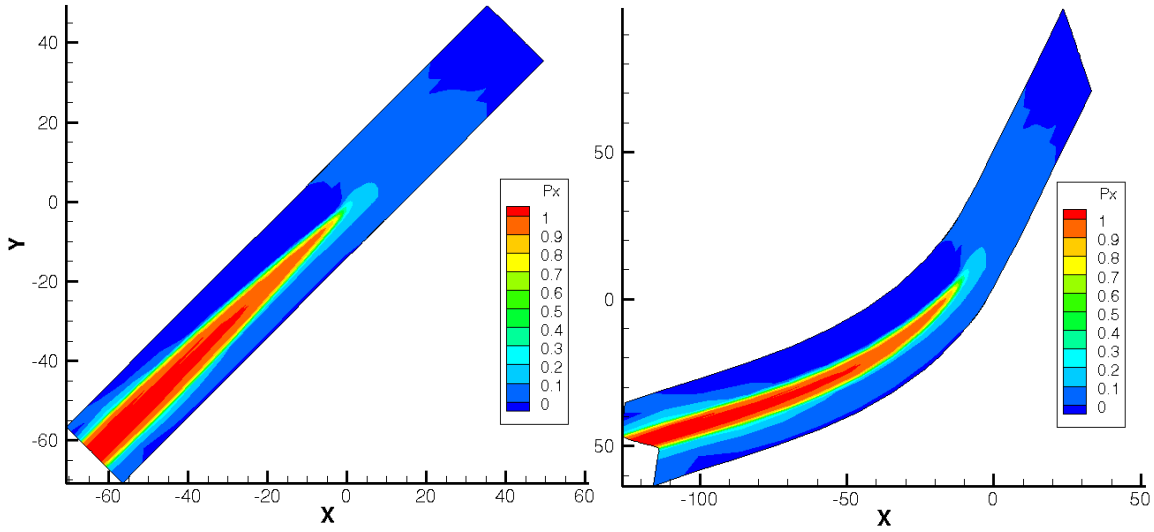

Figure 4.5.5 Polarization contours of un-deformed and deformed configurations of the characteristic unit cell of Figure 4.5.3b with displacements and polarization degrees of freedom relaxed according to the periodic boundary conditions and fixed zero electric potential on top and bottom boundaries. The surface charge corresponding to the polarization is applied on the side surfaces and the displacements are fixed according to (4.42).

Next the displacements on the side boundaries are fixed according to the displacements of equation (4.46). Figure 4.5.5 shows the polarization contours in the deformed and un-deformed configuration of the long unit cell of Figure 4.5.3 in order to avoid any end effects due to fixed displacements and applied charge according to the polarization distribution on the side surfaces. The displacements and polarization boundary conditions are relaxed according to the periodic boundary conditions while the electric potential is fixed to zero. Again we were unable to get a stationary needle by

releasing all five degrees of freedom on the top and bottom boundaries. Releasing the electric potential will result in retraction of the needle indicating the intricate and nonlinear combined effect of electric and mechanical conditions on the existence and stabilization of needle domains to an equilibrium position.

4.5.2.1 Equilibrium Parallel Needle Array with Charge Flow

It is apparent by now that mechanical deformation alone is not enough to overcome the electric field created due to the charge incompatibility of the head to head domain wall for the existence of a stationary needle domain. This depolarizing electric field tends to retract the needle domain to the left in regions of coarse mesh (and hence mesh pinning might interfere with the numerical result). Needle retraction is alleviated in the case when charge redistribution is allowed on the top and bottom boundaries. In the next set of calculations, instead of simply allowing charges to redistribute on the unit cell boundaries we proceed by allowing charges to distribute throughout the entire representative unit cell. To do this, the electric potential degrees of freedom are set equal to zero. The polarization and displacement periodic boundary conditions are then applied to the top and bottom boundaries.

In order to apply realistic boundary conditions on the side surfaces, we first consider the stress free configurations of the left side region with full 90^0 domains, as in the case of perpendicular and antiparallel needle domains. The displacement periodic boundary conditions along the side surfaces in a rotated coordinate system with the horizontal axis along the 90^0 domain walls can be calculated by Equation (4.46). Between the side boundaries and along the needle axis the electric potential and the polarization degrees of freedom are set to be equal and periodic. On the top and bottom surfaces the periodic boundary conditions of Equation (4.47) are applied.

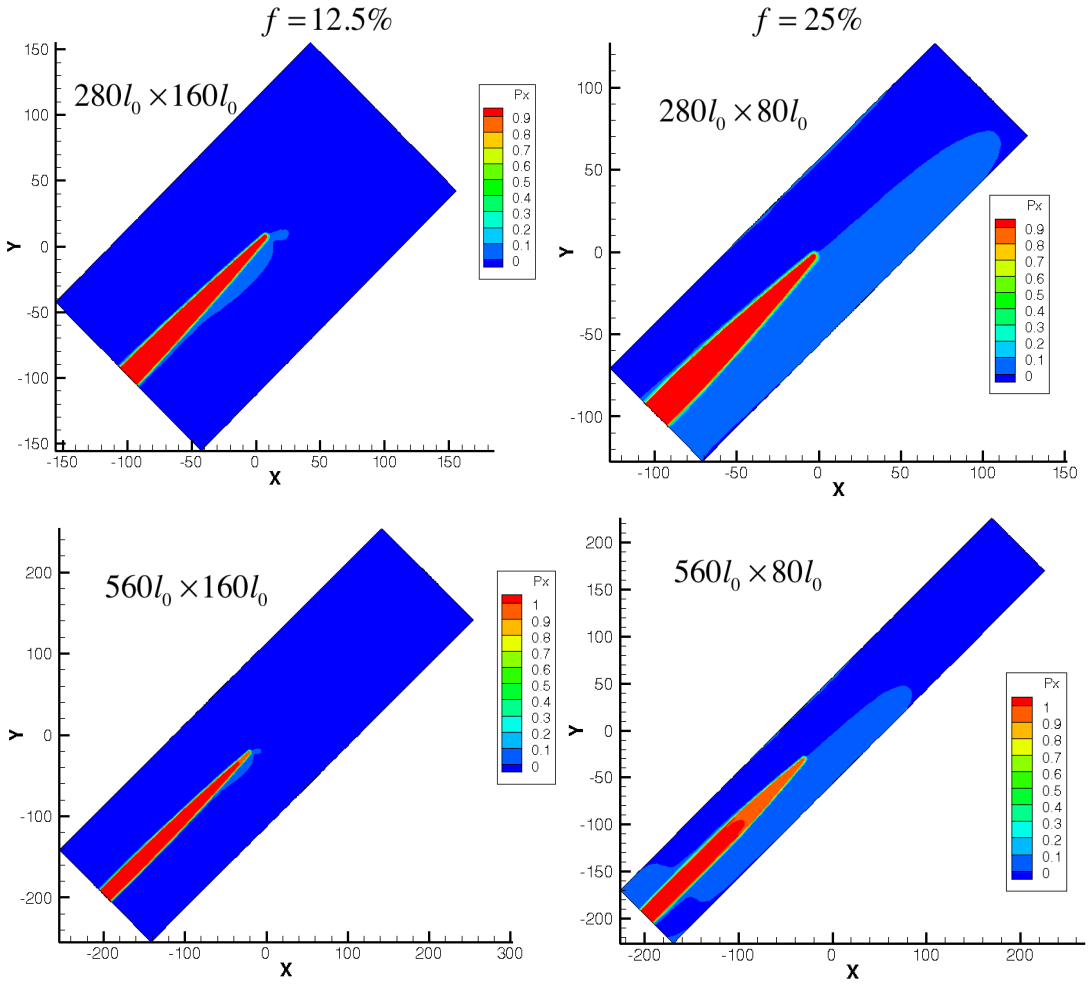

Figure 4.5.6 Polarization contours of un-deformed configurations of the characteristic unit cells of different size for an initial needle volume fraction of 12.5% and 25%. The electric potential is fixed to zero everywhere in the cell and the rest of the degrees of freedom on top and bottom boundaries are relaxed according to the periodic boundary conditions. The displacement degrees of freedom are fixed according to the relaxed stress free displacement and the surface charge corresponding to the polarization is applied on the side surfaces.

The relaxed displacement field and the net charge based on the polarization distribution accounting for the domain wall thickness are then extracted and used as

boundary conditions for the original needle problem as before. Specifically the displacement components on both sides are fixed according to the displacements accounting for the domain wall thickness.

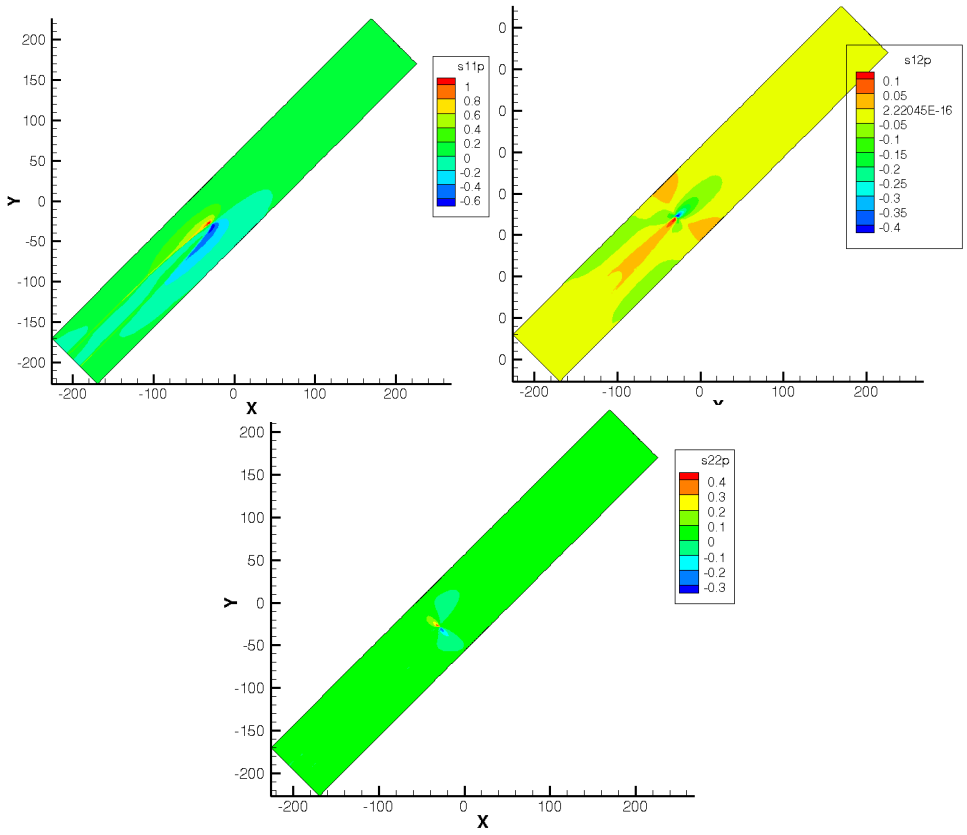

Figure 4.5.7 Stress distribution around the needle tip of the characteristic unit cell of dimension $560l_0 \times 80l_0$ of and initial needle volume fraction of 25%.

Figure 4.5.6 present the polarization contours along the x-direction in the un-deformed configuration for needles of initial volume fraction of 12.5% and 25% respectively. The needle domain thickness is taken to be $20l_0$. Two representative unit cells of different length are used in order to accommodate any boundary effects along the needle axis, caused by the fixed displacements boundary conditions on the side surfaces

The shorter unit cells tend to capture the details of the tip giving to the needle a wedge like characteristic shape. The long unit cell allows for the straight domain walls to be captured. Figure 4.5.7 presents the stress contours along the rotated coordinate system with the horizontal axis along the needle axis. The stress free region corresponds to the part of the needle that maintains the straight domain walls.

Figure 4.5.8 compares the needle tip profiles and positions between the two representative unit cells of different length for the 12.5% and the 25% needle volume fraction cases shown in Figure 4.5.6. The needle tip profiles are symmetric with respect to the needle axis and consist mostly of linear parts that meet at a rounding tip. It is interesting to note that the needle tip position changes with the length of the unit cell. The needle tip for the longer cell has retracted with respect to the equilibrium position of the tip when the shorter cell is considered for both needle volume fractions. Specifically, the difference on the needle tip position along the needle axis is approximately $42l_0$ and $38l_0$ for needle volume fractions of 12.5% and 25% respectively.

The needle tip profile on the other hand is independent of the length for each volume fraction. This is also shown in Figure 4.5.8 where the needle profiles are shifted along the needle axis. Note that for both needle volume fractions the initial position of the needle was assumed to be at the center of the unit cell. Figure 4.5.8a however, shows that only the shorter version of the 25% needle volume fraction reaches equilibrium at the assumed position. The corresponding equilibrium needle tip position for the 12.5% volume fraction is at $15l_0$ from the center of the cell. Figure 4.5.8b compares the needle profiles of the two different volume fractions for the long cell of dimensions $560l_0 \times 80l_0$. The needle tip equilibrium positions differ by approximately $11l_0$ in this case with the thinner needle tip being sharper and extending by $40l_0$ more than the thicker needle of 25% volume fraction which shows a blunted characteristic tip shape.

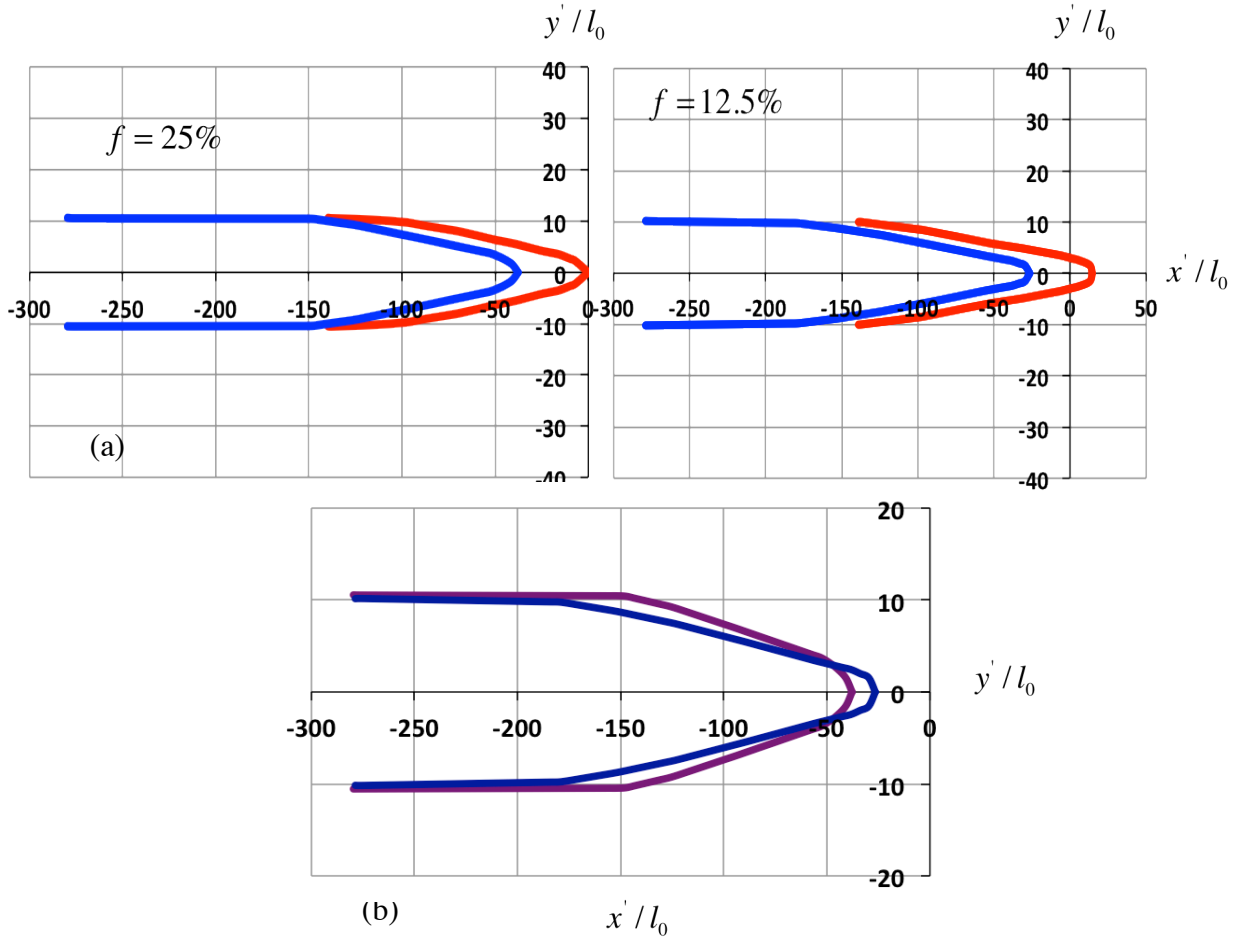

Figure 4.5.8 Needle tip profile and equilibrium position of initial needle volume fraction of 12.5 % and 25%. Red and blue lines correspond to characteristic unit cell of dimensions $280l_0 \times 80l_0$ and $560l_0 \times 80l_0$. Green and red lines correspond to initial needle volume fraction of 12.5% and 25% respectively and unit cell dimensions $560l_0 \times 80l_0$.

4.5.2.2 Effect of Mechanical Loading on the Evolution of the Parallel Needle Array

The effect of mechanical loading on the evolution of the needle is examined next. Here we consider only the 25% needle volume fraction case and the representative unit cell of total dimensions equal to $560l_0 \times 80l_0$. Recall that the unit cell was formed by the mechanical fitting of the two constituent parts of different domain structure shown in Figure 4.5.2. Considering mechanical compatibility in terms of the average deformation

field for a given needle volume fraction, the common boundary was specified in Equation (4.40). Along this boundary the constituent parts of 90^0 domains and the homogeneous parent variant fit together by a simple rotation creating a kink. This kink was shown in the deformed configuration of the single needle equilibrium in Figure 4.5.3.

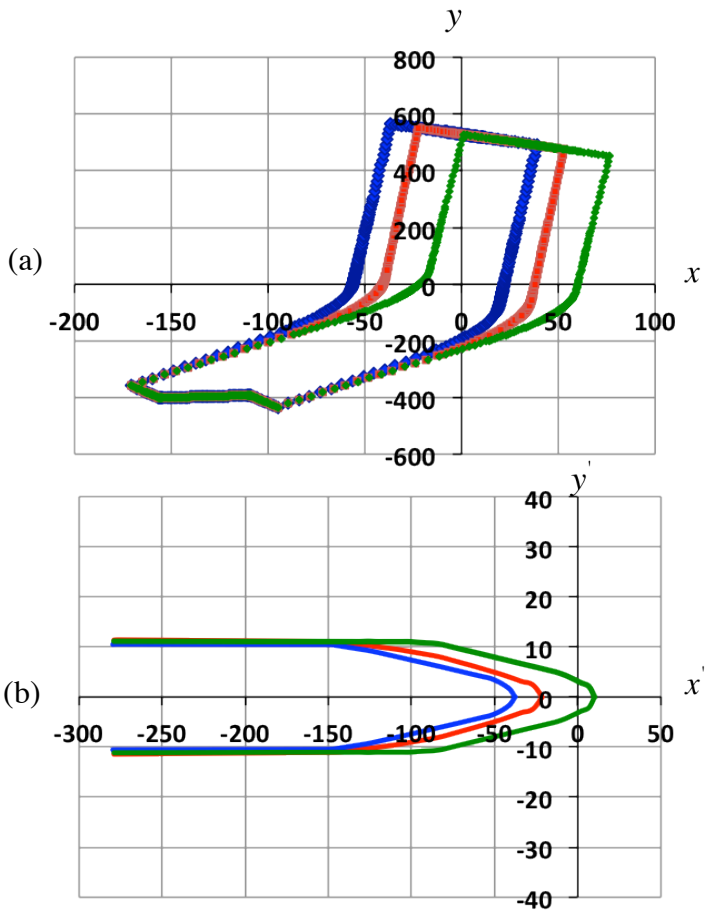

Figure 4.5.9 (a) Deformed configuration of the unit cell of dimensions $560l_0 \times 80l_0$ and initial needle volume fraction of 25%. The blue corresponds to the initial position of the kink at the center of the unit cell. The red and green lines correspond to positions of kink displaced by $15l_0$ and $40l_0$ along the needle axis. (b) The corresponding needle tip profiles and equilibrium positions.

The sharp kink is relaxed to a curved boundary along the region where the needle tip is stabilized when the periodic boundary conditions are applied on the top and bottom surfaces. The initial kink position was taken at the center of the unit cell for all previous calculations, specifying the displacements boundary conditions on the right hand side boundary.

In order to investigate the needle tip equilibrium under mechanical loading we consider the cases were the kink along the common boundary is displaced by $15l_0$ and $40l_0$ along the needle axis and the position of the right hand side surface is calculated. The displacements on the right hand side boundary are fixed to the displacement corresponding to the new positions of the kink. The deformed configuration of the unit cell corresponding to the original position of the kink at the center and the displaced position by $15l_0$ and $40l_0$ along the needle axis are shown in Figure 4.5.9a. Figure 4.5.9b presents the evolution of the needle domain for the different kink positions. We observe that the needle moved forward by evolving the tip by approximately $16l_0$ and $47l_0$ for corresponding kink positions placed at $15l_0$ and $40l_0$ respectively. Our calculations reveal that the 90^0 domain walls along the straight needle body remain stationary with a deviation less than $2l_0$, indicating that the mechanism for the parallel needle evolution under zero stress is through the motion of the tip.

4.6. THE J INTEGRAL FOR EQUILIBRIUM NEEDLE DOMAIN STRUCTURE

The electromechanical J-integral for materials described by the present phase field theory is defined as follows.

$$J = \int_{\Gamma} \left(h n_1 - \sigma_{ij} n_j u_{i,1} + D_i n_i E_1 - \xi_{ji} n_j P_{i,1} \right) d\Gamma \tag{4.48}$$

Here, h is the enthalpy, which can be related to the Helmholtz free energy through the Legendre transformation $h\left(\varepsilon_{ij}, P_i, P_{i,j} E_i\right) = \psi - E_i D_i$. It can be readily proven that the J -integral is zero around a closed contour not enclosing a singularity if the body force b_i , the volume charge density q_i and the polarization rate $\dot{P}_i$ are equal to zero. The latter stresses that the micro-force balance associated with the order parameter is in equilibrium.

All the results reported in this chapter are reported for equilibrium of the micro-force balance associated with the order parameter. The body force and the volume charge density are also taken equal to zero. Therefore, the J integral around the representative unit cells used in this chapter, to model the parallel, antiparallel and orthogonal needle domain arrays, should be equal to zero. We then use J calculations to gage the accuracy of the solutions. Consider a counterclockwise contour around the boundary of the representative unit cell of the parallel needle domains shown in Figure 4.6.1.

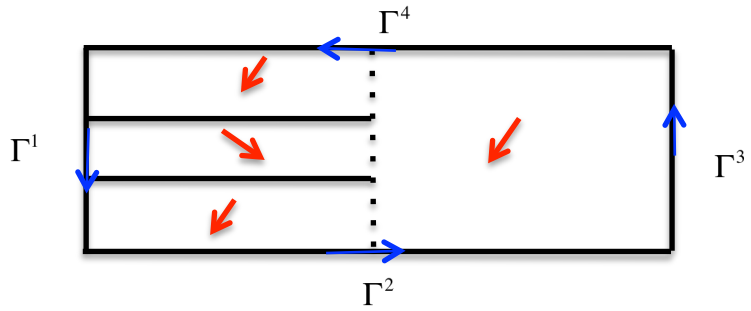

Figure 4.6.1 Counterclockwise contour around the boundary of the representative unit cell of the parallel needle domains.

Note that for the top and bottom periodic boundaries we have:

$$J_{\Gamma^2} = \int_{\Gamma^2} h - \sigma_{11} u_{1,1} - \sigma_{21} u_{2,1} + D_1 E_1 - \xi_{11} P_{1,1} dx_1 = -J_{\Gamma^4} \qquad (4.50)$$

For the side boundaries we have:

$$J_{\Gamma^3} = \int_{\Gamma^3} h - \sigma_{12}u_{1,1} - \sigma_{22}u_{2,1} + D_2E_1 - \xi_{21}P_{1,1} - \xi_{22}P_{2,1}dx_2 = -J_{\Gamma^1} \qquad (4.51)$$

Note that Equations (4.50) and (4.51) also hold for the contour around the corresponding representative unit cells of anti parallel and perpendicular needle domains. Due to the periodic boundary conditions along the top and the bottom surfaces resulting in the contours of the J -integral along the periodic boundaries to cancel, we calculate the J -integral along paths between the periodic surfaces, i.e. along paths corresponding to the Γ^1 and Γ^3 paths of Figure 4.6.1. The value of the J -integral along these paths should then be the same. The J -integral is calculated along these paths for all three needle array configurations and path-independence is established up to 0.5% for all calculations presented in this chapter.

4.7. DISCUSSION

In this chapter, equilibrium configurations of infinite needle-like array patterns often encountered in $BaTiO_3$ single crystals were modeled using a phase field model approach and the finite element method. A representative unit cell was employed to model the far field electromechanical conditions that render stable needle patterns. It was assumed that the unit cell is a result of electromechanical fitting of the domain patterns far way from the needle tips in terms of average spontaneous deformation fields. Three needle domain patterns were considered and equilibrium needle profiles and the distribution of fields around the needle tips were studied. The evolution and stability of

perpendicular and antiparallel needle configurations was investigated under electric loading conditions.

Stable parallel needle patterns were obtained allowing charge to flow freely on the unit cell and evolution of the needle was investigated under mechanical loading. We were unable to model stable parallel needle configurations without charge flow. This is attributed to the fact that the excess charge at the tip is not be compensated by polarization redistribution, creating a depolarizing field that tends to dissolve the needle.

Chapter V Outlook and Future Work

Numerical problems related to mesh requirements were encountered in the study of the equilibrium needle domain patterns. The mesh used in these calculations was a structured mesh of certain capabilities. On regions surrounding the needle tips large polarization gradient were expected and fine mesh requirements were met, often with a trial and error approach, as the needle final equilibrium tip position could not always have been predicted. Evolution of needle domains in regions of coarse mesh would cause numerical pinning and interfere with the accuracy of the calculations. A domain wall that would otherwise sweep through a region unimpeded is instead stopped at the location where the mesh coarsens. On the other hand using a structured mesh and meeting the fine mesh requirements along the regions that demand it transfers to regions of smooth polarization distribution that do not require special treatment. This fact considerably increases the mesh size requirements and posed a restriction on the needle domain thicknesses and the relative needle volume fractions investigated. Adaptive meshing techniques would greatly facilitate the calculations and provide the means to investigate a broader case of needle domains of realistic thickness and volume fraction.

In this work we only investigated the retraction of perpendicular and antiparallel needles for a small range of net surface charge loading between the non-periodic boundaries and a possible lower limit in the stability of the needles was only approached for the perpendicular case. More calculations need to be performed to expand the range of electrical loading and examine the limit loading for stable needle retraction. Finally the same analysis should be performed for needle domain motion on the opposite direction, i.e. meeting of the needle tips.

Appendix A: Integration of Constitutive Equations and the Algorithmic Tangent Matrix

In the finite element setting the total strain is known at every material point (integration station) at material time $t + \Delta t$. The stress state is updated by the integration of the non-linear constitutive equations using a Backward Euler scheme. For this purpose the rate equations are written in the incremental form as

$$\frac{3}{2}\hat{s}_{ij}^{I+1}\hat{s}_{ij}^{I+1} - \sigma_0^2 = 0 \tag{A.1}$$

$$\hat{s}_{ij}^{I+1} = 2\mu\left(e_{ij}^{t+\Delta t} - \varepsilon_{ij}^{r,t} - \Delta\varepsilon_{ij}^{r}\right) - s_{ij}^{B} \tag{A.2}$$

$$\Delta\varepsilon_{ij}^{r} = 3\lambda\hat{s}_{ij}^{I+1} \tag{A.3}$$

where the time t is associated with the previous equilibrium state of the finite element procedure and the superscript $I+1$ corresponds to the ongoing iteration of the current finite element step. The solution of the above equations is reduced to finding the components of the remanent strain increment as in metal plasticity. Using the consistency condition and noting that $\hat{s}_{ij}^{I+1}\hat{s}_{ij}^{I+1} = \frac{2}{3}\sigma_0^2$, allows us to solve for the plastic multiplier as

$$\lambda = \frac{\sqrt{\frac{2}{3}\Delta\varepsilon_{kl}^{r}\Delta\varepsilon_{kl}^{r}}}{2\sigma_0} \tag{A.4}$$

Then, at every iteration, $I+1$, the components of the remanent strain increment have to satisfy the following set of non-linear equations.

$$\Delta\varepsilon_{ij}^{r} - \frac{3\Delta\varepsilon^{r}}{2\sigma_0}\left[2\mu\left(e_{ij}^{t+\Delta t} - \varepsilon_{ij}^{r,t} - \Delta\varepsilon_{ij}^{r}\right) - s_{ij}^{B}\right] = r_{ij} = 0 \tag{A.5}$$

where $\Delta\varepsilon^{r} = \sqrt{\frac{2}{3}\Delta\varepsilon_{kl}^{r}\Delta\varepsilon_{kl}^{r}}$. The above equations are solved iteratively using the Newton-Raphson method. The strain increments update is written to first order as $\Delta\varepsilon_{ij}^{r,i+1} = \Delta\varepsilon_{ij}^{r,i} + d\varepsilon_{ij}^{r}$ where $d\varepsilon_{ij}^{r}$ is computed by the linear equations

$$J_{ijkl}\, d\varepsilon_{ij}^{r} = -r_{ij}^{i} \tag{A.6}$$

Here, the superscript i refers to the iteration of the constitutive integration scheme and r_{ij}^{i} is the residual of the equation (3.14). The Jacobian of the system is computed by differentiating the equations r_{ij}^{i} with respect to the unknown remanent strain and is given as

$$\begin{aligned} J_{ijkl} = \delta_{ik}\delta_{jl} + \frac{3}{2\sigma_0}\Delta\varepsilon^{r}\left(2\mu\delta_{ik}\delta_{jl} + H_{ijkl}\right) \\ - \frac{\Delta\varepsilon_{kl}^{r,i}}{\sigma_0\Delta\varepsilon^{r}}\left[2\mu\left(e_{ij} - \varepsilon_{ij}^{r} - \Delta\varepsilon_{ij}^{r,i}\right) - s_{ij}^{B,i}\right]. \end{aligned} \tag{A.7}$$

where $s_{ij}^{B,i} = \left.\frac{\partial\Psi^{r}}{\partial\varepsilon_{ij}^{r}}\right|_{\varepsilon_{ij}^{r,t}+\Delta\varepsilon_{ij}^{r,i}}$. Next, noting that $2\mu\left(e_{ij}^{t+\Delta t} - \varepsilon_{ij}^{r,t} - \Delta\varepsilon_{ij}^{r,i}\right) - s_{ij}^{B} = \hat{s}_{ij}^{I+1} = \frac{2\sigma_0\Delta\varepsilon_{ij}^{r,i}}{3\Delta\varepsilon^{r}}$ and the symmetries implied, i.e. $J_{ijkl} = J_{klij} = J_{lkij} = J_{lkji}$, the forth order tensor J_{ijkl} can be written as

$$J_{ijkl} = \frac{1}{2}\frac{\sigma_0}{\Delta\varepsilon^r}\left(\delta_{ik}\delta_{jl} + \delta_{il}\delta_{jk}\right) + \frac{3}{2}\left(\mu\left(\delta_{ik}\delta_{jl} + \delta_{il}\delta_{jk}\right) + H_{ijkl}\right) - \frac{2\Delta\varepsilon_{ij}^{r,i}\Delta\varepsilon_{kl}^{r,i}}{3\Delta\varepsilon^{r3}} \tag{A.8}$$

where $H_{ijkl} = \left.\dfrac{\partial^2\Psi^r}{\partial\varepsilon_{kl}^r\partial\varepsilon_{ij}^r}\right|_{\varepsilon_{ij}^{r,I}+\Delta\varepsilon_{ij}^{r,i}}$. Once the remanent strain state is determined the algorithmic tangent modulus is computed by varying the strain in (3.14) and noting that at the converged solution we have $\Delta\varepsilon_{ij}^r = 3\lambda\left(s_{ij}^{I+1} - s_{ij}^B\right)$. Then

$$\underbrace{\left[\delta_{ik}\delta_{jl} - \frac{9\left(s_{ij}^{I+1} - s_{ij}^B\right)\left(s_{kl}^{I+1} - s_{kl}^B\right)}{6\sigma_0^2} + 6\lambda\mu\delta_{ik}\delta_{jl} - 3\lambda H_{ijkl}\right]}_{A_{ijkl}^{-1}} d\varepsilon_{kl}^r = 6\mu\lambda de_{ij} \Rightarrow$$

$$\boxed{d\varepsilon_{ij}^r = 6\mu\lambda A_{ijkl} de_{ij}} \tag{A.9}$$

Substituting in the incremental stress-strain constitutive relation we then have

$$d\sigma_{ij} = \left(\lambda_e + 2\mu\right)\delta_{ij}d\varepsilon_{kk} + 2\mu\left(\delta_{ik}\delta_{jl} - 6\lambda\mu A_{ijkl}\right)de_{kl} \tag{A.10}$$

where λ_e is the *Lame* constant and δ_{ij} the Kronecker delta. We are interested in a plane strain crack with a volume conserving remanent deformation. The problem can be specifically formulated to calculate only the plane components of the remanent strain increment, i.e. $\Delta\varepsilon_{11}^r$, $\Delta\varepsilon_{22}^r$, $\Delta\varepsilon_{12}^r$ as follows.

Eliminating the equation corresponding to the out of plane strain increment and using that $d\varepsilon_{33}^r = -d\varepsilon_{11}^r - d\varepsilon_{22}^r$ the correction of the remanent strain components is given as the solution of the system

$$\left[J^{ps} \right] \left\lfloor d\varepsilon^{r} \right\rfloor = \left\lfloor f \right\rfloor \tag{A.11}$$

where

$$\left\lfloor d\varepsilon^{r} \right\rfloor = \left\{ \begin{array}{ccc} d\varepsilon_{11}^{r} & d\varepsilon_{22}^{r} & d\varepsilon_{12}^{r} \end{array} \right\}^{T} ,$$

$$\left\lfloor f \right\rfloor = \left\{ \begin{array}{ccc} -r_{11} + r_{33} & -r_{22} + r_{33} & -r_{12} - r_{21} \end{array} \right\}^{T} \text{ and}$$

$$\left[J^{ps} \right] = \left[\begin{array}{ccc} J_{1111} - J_{1133} - J_{3311} + J_{3333} & J_{1122} - J_{1133} - J_{3322} + J_{3333} & J_{1112} + J_{1121} - J_{3312} - J_{3321} \\ J_{2211} - J_{2233} - J_{3311} + J_{3333} & J_{2222} - J_{2233} - J_{3322} + J_{3333} & J_{2212} + J_{2221} - J_{3312} - J_{3321} \\ J_{1211} + J_{2111} - J_{1233} - J_{2133} & J_{1222} + J_{2122} - J_{1233} - J_{2133} & J_{1212} + J_{1221} + J_{2112} + J_{2121} \end{array} \right]$$

Note that in solving $\left\lfloor f \right\rfloor = 0$, the Jacobian matrix $\left[J^{ps} \right]$ is symmetric. Next, using the same algebraic manipulations the consistent tangent modulus is calculated explicitly as

$$\left[A^{-1} \right] \left\lfloor de^{r} \right\rfloor = 3\mu \left\lfloor de \right\rfloor \tag{A.12}$$

where

$$\left\lfloor de^{r} \right\rfloor = \left\{ \begin{array}{ccc} de_{11}^{r} & de_{22}^{r} & de_{12}^{r} \end{array} \right\}^{T} ,$$

$$\left\lfloor de \right\rfloor = \left\{ \begin{array}{ccc} de_{11} - de_{33} & de_{22} - de_{33} & de_{12} + de_{21} \end{array} \right\}^{T} \text{ and}$$

$$\left[A^{-1}\right]=\begin{bmatrix} A^{-1}_{1111}-A^{-1}_{1133}-A^{-1}_{3311}+A^{-1}_{3333} & A^{-1}_{1122}-A^{-1}_{1133}-A^{-1}_{3322}+A^{-1}_{3333} & A^{-1}_{1112}+A^{-1}_{1121}-A^{-1}_{3312}-A^{-1}_{3321} \\ A^{-1}_{2211}-A^{-1}_{2233}-A^{-1}_{3311}+A^{-1}_{3333} & A^{-1}_{2222}-A^{-1}_{2233}-A^{-1}_{3322}+A^{-1}_{3333} & A^{-1}_{2212}+A^{-1}_{2221}-A^{-1}_{3312}-A^{-1}_{3321} \\ A^{-1}_{1211}+A^{-1}_{2111}-A^{-1}_{1233}-A^{-1}_{1233} & A^{-1}_{2122}+A^{-1}_{1222}-A^{-1}_{1233}-A^{-1}_{1233} & A^{-1}_{1212}+A^{-1}_{1221}+A^{-1}_{2112}+A^{-1}_{2121} \end{bmatrix}$$

Note that $\left\lfloor de^{r}\right\rfloor = 3\mu\left[d\right]\left[A\right]\left[d\right]\left\lfloor d\varepsilon\right\rfloor$.

Finally, the stress update can be written as

$$\left\lfloor d\sigma\right\rfloor = \left[C^{\tan}\right]\left\lfloor d\varepsilon\right\rfloor \tag{A.13}$$

where

$$\left[C^{\tan}\right] = \left[C\right] - 3\mu\left[C\right]\left\lfloor d\right\rfloor\left[A\right]\left\lfloor d\right\rfloor \tag{A.14}$$

is the plane strain algorithmic tangent matrix and $\left[d\right]$ is a constant matrix relating the deviatoric components of strain to the strain, $\left\lfloor de\right\rfloor = \left[d\right]\left\lfloor d\varepsilon\right\rfloor$.

Appendix B: Helmholtz Free Energy and Material Properties of $BaTiO_3$

The general form for the Helmholtz free energy applied in Chapter 4 is given in Equation (4.25). For a coordinate system with the Cartesian axes aligned with [100] directions, the specific form used to fit the dielectric, piezoelectric and elastic properties of ferroelectric single crystals that undergo a cubic to tetragonal phase transformation through the Curie temperature is simplified to (Su and Landis, 2007):

$$
\begin{aligned}
\psi = {} & \frac{a_0}{2}\left(P_{1,1}^2 + P_{2,2}^2 + P_{3,3}^2 + P_{1,2}^2 + P_{2,1}^2 + P_{1,3}^2 + P_{3,1}^2 + P_{2,3}^2 + P_{3,2}^2\right) \\
& + \frac{a_1}{2}\left(P_1^2 + P_2^2 + P_3^2\right) + \frac{a_2}{4}\left(P_1^4 + P_2^4 + P_3^4\right) + \frac{a_3}{2}\left(P_1^2 P_2^2 + P_2^2 P_3^2 + P_1^2 P_3^2\right) \\
& + \frac{a_4}{6}\left(P_1^6 + P_2^6 + P_3^6\right) + a_6\left(P_1^4\left(P_2^2 + P_3^2\right) + P_2^4\left(P_1^2 + P_3^2\right) + P_3^4\left(P_1^2 + P_2^2\right)\right) \\
& + \frac{a_5}{4}\left(P_1^4 P_2^4 + P_2^4 P_3^4 + P_1^4 P_3^4\right) - \frac{b_1}{2}\left(\varepsilon_{11} P_1^2 + \varepsilon_{33} P_2^2 + \varepsilon_{33} P_3^2\right) \\
& - \frac{b_2}{2}\left(\left(\varepsilon_{22} + \varepsilon_{33}\right) P_1^2 + \left(\varepsilon_{11} + \varepsilon_{33}\right) P_2^2 + \left(\varepsilon_{22} + \varepsilon_{11}\right) P_3^2\right) \\
& - b_3\left(\left(\varepsilon_{12} + \varepsilon_{21}\right) P_1 P_2 + \left(\varepsilon_{13} + \varepsilon_{31}\right) P_1 P_3 + \left(\varepsilon_{23} + \varepsilon_{32}\right) P_2 P_3\right) \\
& + \frac{c_1}{2}\left(\varepsilon_{11}^2 + \varepsilon_{22}^2 + \varepsilon_{33}^2\right) + c_2\left(\varepsilon_{11}\varepsilon_{22} + \varepsilon_{22}\varepsilon_{33} + \varepsilon_{22}\varepsilon_{33}\right) \\
& + \frac{c_3}{2}\left(\varepsilon_{12}^2 + \varepsilon_{21}^2 + \varepsilon_{13}^2 + \varepsilon_{31}^2 + \varepsilon_{23}^2 + \varepsilon_{32}^2\right) \\
& + \left(\frac{f_1}{2}\varepsilon_{11}^2 + \frac{f_2}{2}\left(\varepsilon_{22}^2 + \varepsilon_{33}^2\right) + f_3\left(\varepsilon_{11}\varepsilon_{22} + \varepsilon_{11}\varepsilon_{33}\right) + f_4\varepsilon_{22}\varepsilon_{33}\right. \\
& \left. + \frac{f_5}{2}\left(\varepsilon_{12}^2 + \varepsilon_{21}^2 + \varepsilon_{13}^2 + \varepsilon_{31}^2\right) + \frac{f_6}{2}\left(\varepsilon_{23}^2 + \varepsilon_{32}^2\right)\right) P_1^2 \\
& + \left(\frac{f_1}{2}\varepsilon_{22}^2 + \frac{f_2}{2}\left(\varepsilon_{11}^2 + \varepsilon_{33}^2\right) + f_3\left(\varepsilon_{11}\varepsilon_{22} + \varepsilon_{22}\varepsilon_{33}\right) + f_4\varepsilon_{11}\varepsilon_{33}\right. \\
& \left. + \frac{f_5}{2}\left(\varepsilon_{12}^2 + \varepsilon_{21}^2 + \varepsilon_{23}^2 + \varepsilon_{32}^2\right) + \frac{f_6}{2}\left(\varepsilon_{13}^2 + \varepsilon_{31}^2\right)\right) P_2^2 \\
& + \left(\frac{f_1}{2}\varepsilon_{33}^2 + \frac{f_2}{2}\left(\varepsilon_{22}^2 + \varepsilon_{11}^2\right) + f_3\left(\varepsilon_{11}\varepsilon_{33} + \varepsilon_{22}\varepsilon_{33}\right) + f_4\varepsilon_{11}\varepsilon_{22}\right. \\
& \left. + \frac{f_5}{2}\left(\varepsilon_{13}^2 + \varepsilon_{31}^2 + \varepsilon_{23}^2 + \varepsilon_{32}^2\right) + \frac{f_6}{2}\left(\varepsilon_{12}^2 + \varepsilon_{21}^2\right)\right) P_3^2 \\
& + \left(\frac{g_1}{4}\varepsilon_{11} + \frac{g_2}{4}\left(\varepsilon_{22} + \varepsilon_{33}\right)\right) P_1^4 + \left(\frac{g_1}{4}\varepsilon_{22} + \frac{g_2}{4}\left(\varepsilon_{11} + \varepsilon_{33}\right)\right) P_2^4 \\
& + \left(\frac{g_1}{4}\varepsilon_{33} + \frac{g_2}{4}\left(\varepsilon_{11} + \varepsilon_{22}\right)\right) P_3^4 + \frac{g_3}{4}\left(\varepsilon_{12} + \varepsilon_{21}\right)\left(P_1 P_2^3 + P_2 P_1^3\right) \\
& + \frac{g_3}{4}\left(\varepsilon_{13} + \varepsilon_{31}\right)\left(P_1 P_3^3 + P_3 P_1^3\right) + \frac{g_3}{4}\left(\varepsilon_{23} + \varepsilon_{32}\right)\left(P_2 P_3^3 + P_3 P_2^3\right) \\
& + \frac{1}{2\kappa_0}\left(\left(D_1 - P_1\right)^2 + \left(D_2 - P_2\right)^2 + \left(D_3 - P_3\right)^2\right)
\end{aligned}
\tag{B.1}
$$

The properties of mono-domain single crystal barium titanate ($BaTiO_3$) have been measured by Li et al. (Li et al., 1991), at room temperature (~22 °C). For a domain with spontaneous polarization in the x_3 direction, the spontaneous polarization and strain rate are:

$$P_3^s = 0.26C/m^2,\ P_1^s = P_2^s = 0,\ \varepsilon_{33}^s = 0.0082,$$
$$\varepsilon_{11}^s = \varepsilon_{22}^s = -0.0027,\ \varepsilon_{12}^s = \varepsilon_{21}^s = \varepsilon_{23}^s = 0.$$

In the same coordinate system, the elastic, piezoelectric, and dielectric properties given in standard Voigt notation are:

$$s_{11}^E = 8.01\times10^{-12}m^2/N, \quad s_{12}^E = -1.57\times10^{-12}m^2/N, \quad s_{13}^E = -4.6\times10^{-12}m^2/N$$
$$s_{33}^E = 12.8\times10^{-12}m^2/N, \quad s_{44}^E = 17.8\times10^{-12}m^2/N, \quad s_{66}^E = 7.91\times10^{-12}m^2/N,$$
$$d_{33} = 8106\times10^{-12}C/N, \quad d_{31} = -50\times10^{-12}m^2/N, \quad d_{15} = 580\times10^{-12}m^2/N,$$
$$\kappa_{11}^\sigma = 3.63\times10^{-9}Vm/C, \quad \kappa_{33}^\sigma = 1.42\times10^{-9}Vm/C,$$
$$\kappa_0 = 8.854\times10^{-12}Vm/C.$$

where κ_0 is the dielectric permittivity of free space.

In order to fit these properties of a mono-domain the coefficients of the Helmholtz free energy are chosen as follows:

where $E_0 = 2.12847 \times 10^7 V/m$, $\sigma_0 = E_0 P_0 / \varepsilon_0 = 692 \times 10^6 N/m^2$. The definition of P_0 and ε_0 arises from the spontaneous state and are $P_0 = 0.26 C/m^2$, $\varepsilon_0 = 0.0082$. And the critical electric field E_0 is the magnitude of the electric field required to cause homogeneous 180° switching when the electric field is applied in the opposite direction of the uniform spontaneous polarization. Finally, the stress σ_0 is a derived quantity used for normalizations.

References

R. J. Astley (1996), FE mode-matching schemes for the exterior helmholtz problem and their relationship to the FE-DtN approach, Communications in Num. Methods in Eng., 12, pp. 257–267.

R.S. Barsoum (1977), Triangular Quarter-Point Elements as Elastic and Perfectly-Plastic Crack Tip Elements, International Journal for Numerical Methods in Engineering, 11, pp. 85-98.

B. Budiansky, J. W. Hutchinson and J. C. Lambropoulos (1983), Continuum theory of dilatant transformation toughening in ceramics Int. J. Solids Struct. 19, pp. 337–55.

W. Cao and L. E. Cross (1991), Theory of tetragonal twin structures in ferroelectric perovskites with a first-order phase transition, Physical Review B, 44, pp. 5-12.

D. Carka and C. M. Landis (2011), On the Path-Dependence of the J-integral Near a Stationary Crack in an Elastic-Plastic Material, Journal of Applied Mechanics, 78, pp. 011006.

D. Carka, M. E. Mear, M.E. and C. M. Landis (2011), The Dirichlet-to-Neumann Map for Two-Dimensional Crack Problems, Computer Methods in Applied Mechanics and Engineering, 200, pp. 1263-1271.

S. Choudhury, Y. L. Li, C. E. Krill and L. Q. Chen (2005), Phase-field simulation of polarization switching and domain evolution in ferroelectric polycrystals, Acta Materialia, 53, pp. 5313-5321.

A. C. F. Cocks and R. M. and McMeeking (1999), A phenomenological constitutive law for the behavior of ferroelectrics, Ferroelectrics, 228, pp. 219–228.

D. Damjanovic (1998), Ferroelectric, dielectric and piezoelectric properties of ferroelectric thin films and ceramics, Rep. Prog. Phys., 61, pp. 1267–1324.

A. F. Devonshire, (1954), Theory of Ferroelectrics, Philosophical Magazine Supplement.

W. J. Drugan, J. R. Rice and T. L. Sham (1982), Asymptotic Analysis of Growing Plane Strain Tensile Cracks in Elastic-Ideally Plastic Solids, Journal of the Mechanics and Physics of Solids, 30, pp. 447-473.

Z. Z. Du and J. W. Hancock (1991), The Effect of Non-Singular Stresses on Crack-Tip Constraint, Journal of the Mechanics and Physics of Solids, 39, pp. 555-567.

J. Dundurs (1969), Discussion of a paper by D.B. Bogy, Journal of Applied Mechanics, 36, pp. 650–652.

J. D. Eshelby (1956), The Continuum Theory of Lattice Defects, Solid State Physics, III, eds. Seitz, F. and Turnbull, D., Academic Press.

J. D. Eshelby (1970), The Energy Momentum Tensor in Continuum Mechanics, Inelastic Behavior of Solids, ed. Kanninen, M.F. et al., McGraw-Hill, New York.

D. Fang and C. Li (1999), Nonlinear electric-mechanical behavior of a soft PZT-51 ferroelectric ceramic, J. Mater. Sci. 34, pp. 4001–4010.

I. Fried (1974), Finite elements analysis of incompressible material by residual energy balancing, Int. J. of Solids Structs. 10, pp. 993-1002.

A. Frolich (2001), Mikromechanisches modell zur ermittlung effektiver materialeigenschaften von piezoelektrischen polykristallen, Thesis Universitat Karlsruhe, Germany.

E. Fried, and M. E. Gurtin (1993), Continuum Theory of Thermally Induced Phase Transitions Based on an Order Parameter, Physica D, 68, pp. 326-343.

E. Fried, and M. E. Gurtin (1994), Dynamic Solid-solid Transitions with Phase Characterized by an Order Parameter, Physica D, 72, pp. 287-308.

P. W. Forsbergh (1949), Domain structure and phase transition in $BaTiO_3$, Physical Review, 76 (8), pp. 1187-1201.

J. Fousek and V. Janovec (1969), The Orientation of Domain Walls in Twinned Ferroelectric Crystals, J. Appl. Physics, 40(1), pp. 135-142.

J. Fousek and B. Brezina (1961a). A contribution to the statics of 90◦ wedge-shaped domains in BaTiO3 crystals. Czech J Phys., 1961, 11,pp. 261–7.

J. Fousek and B. Brezina (1961b). The motion of 90◦ wedge domains in $BaTiO_3$ in an alternating electric field. Czech J Phys., 11, pp. 344–84.

D. Givoli and J.B. Keller (1989), A Finite Element Method for Large Domains, Computer Methods in Applied Mechanics and Engineering, 76, pp. 41-66.

D. Givoli and J.B. Keller (1990), Non-Reflecting Boundary Conditions for Elastic Waves, Wave Motion, 12, pp. 261-279.

D. Givoli (1991), Non-Reflecting Boundary Conditions, Journal of Computational Physics, 94, pp. 1-29.

D. Givoli (1992), Numerical Methods for Problems in Infinite Domains, Elsevier, Amsterdam.

D. Givoli and L. Rivkin (1993), The DtN finite-element method for elastic domains with cracks and re-entrant corners, Computers and Structures, 49, pp. 633–642.

D. Givoli, I. Patlashenko and J.B. Keller (1998), Discrete Dirichlet-to-Neumann Maps for Unbounded Domains, Computer Methods in Applied Mechanics and Engineering, 164, pp. 173-185.

M. E. Gurtin (1996), Generalized Ginzburg-Laudau and Cahn-Hilliard Equations Based on a Microforce Balance, Physica D, 92, pp. 178-192.

S. Hackemann and W. Pfeiffer (2003), Domain switching in process zones of PZT: characterization by micro diffraction and fracture mechanical methods, J. Eur. Ceram. Soc., 23, pp.141–151.

G.H. Haertling (1999), Ferroelectric Ceramics: History and Technology, Journal of the American Ceramics Society 82.

P.D. Hilton, and J.W. Hutchinson (1971), Plastic Intensity Factors for Cracked Plates, Engineering Fracture Mechanics, 3, pp. 435-451.

J. E. Huber, N. A. Fleck, C. M. Landis and R. M. McMeeking (1999), A constitutive model for ferroelectric polycrystals, J. Mech. Phys. Solids, 47, pp. 1663–1697.

J.W. Hutchinson (1968), Plastic Stress and Strain Fields at a Crack Tip, Journal of the Mechanics and Physics of Solids, 16, pp. 337-347.

J. W. Hutchinson (1983), Fundamentals of the Phenomenological Theory of Non-Linear Fracture Mechanics, Journal of Applied Mechanics, 50, pp. 1042-1051.

J. W. Hutchinson (1968), Singular Behaviour at the End of a Tensile Crack in a Hardening Material, Journal of the Mechanics and Physics of Solids, 16, pp. 13-31.

E. T. Jaynes (1953), Ferroelectricity, Princeton University Press.

Y. Jiang, D. Fang and F. Li (2007), In situ observation of electric-field-induced domain switching near a crack tip in poled 0.62PbMg1/3Nb2/3O3–0.38PbTiO3 single crystal, Applied Physics Letters, 90, 222907.

F. Jona and G. Shirane, (1962), Ferroelectric Crystals, Pergamon Press, New York.

J. L. Jones, S. M. Motahari, M. Varlioglu, U. Lienert, J. V. Bernier, M. Hoffman and E. Ustundag (2007), Crack tip process zone domain switching in a soft lead zirconate titanate ceramic, Acta Mater., 55, pp. 5538–5548.

M. Kamlah (2001), Ferroelectric and ferroelastic piezoceramics—modeling and electromechanical hysteresis phenomena, Contin. Mech. Thermodyn., 13, pp. 219–268.

J.B. Keller and D. Givoli (1989), Exact Non-Reflecting Boundary Conditions, Journal of Computational Physics, 82, pp. 172-192.

H. Kessler and H. J. Balke (2001), On the local and average energy release in polarization switching phenomena, J. Mech. Phys. Solids, 49, pp. 953–978.

J. H. Kim and G.H. Paulino (2002), Finite Element Evaluation of Mixed Mode Stress Intensity Factors in Functionally Graded Materials, Internationl Journal for Numerical Methods in Engineering, 53, pp. 1903-1935.

A. Kontsos and C. M. Landis (2009), Computational modeling of domain wall interactions with dislocations in ferroelectric single crystals, International Journal of Solids and Structures, 46, pp. 1491-1498.

M. Kuna (2010), Fract. mechanics of piezoelectric materials—Where are we right now? Eng. Fract. Mech., 77, pp. 309–326.

C. M. Landis (2002), A New Finite-Element Formulation for Electromechanical Boundary Value Problems, International Journal for Numerical Methods in Engineering, 55, pp. 613-628.

C. M. Landis (2002), Uncoupled, Asymptotic Mode III and Mode E Crack Tip Solutions in Non-Linear Ferroelectric Materials, Engineering Fracture Mechanics, 69, pp. 13-23.

C. M. Landis (2002), Fully coupled, multi-axial, symmetric constitutive laws for polycrystalline ferroelectric ceramics, J. Mech. Phys. Solids, 50, pp. 127–152.

C. M. Landis (2003a), On the strain saturation conditions for polycrystalline ferroelastic materials, J. Appl. Mech., 70, pp. 470–478.

C. M. Landis (2003b), On the fracture toughness of ferroelastic materials, J. Mech. Phys. Solids, 51, pp. 1347–1369.

C. M. Landis (2004), Nonlinear constitutive modeling of ferroelectrics, Curr. Opin. Solid State Mater. Sci., 8, pp. 59–69.

C. M. Landis, J. Wang and J. Sheng (2004), Micro-electromechanical determination of the possible remanent strain and polarization states in polycrystalline ferroelectrics and implications for phenomenological constitutive theories, J. Intell. Mater. Syst. Struct., 15, pp. 513–525.

N. Levy, P. V. Marcal, W. J. Ostergren and J. R. Rice (1971), Small Scale Yielding Near a Crack in Plane Strain: A Finite Element Analysis, International Journal of Fracture, 7, pp. 142-156.

F.Z. Li, C.F. Shih, and A. Needleman (1985), A Comparison of Methods for Calculating Energy Release Rates, Engineering Fracture Mechanics, 21, pp. 405-421.

J. Y. Li and D. Liu (2004), On ferroelectric crystals with engineered domain configurations, Journal of Mechanics and Physics of Solids, 52, pp. 1719-1742.

W. Li, C. M. and Landis (2011), Nucleation and growth of domains near crack tips in single crystal ferroelectrics, Engineering Fracture Mechanics, 78, pp. 1505-1513.

Z. Li, S. K. Chan, M. H. Grimsditch, and E. S. Zouboulis (1991), The Elastic and Electromechanical Properties of Tetragonal BaTiO3 Single Crystals, Journal of Applied Physics, 70, pp. 7327-7332.

E. A. Little (1955), Dynamic behavior of domain walls in barium titanate. Phys. Rev., 98 (4), pp. 978–84.

C. S. Lynch (1996), The effect of uniaxial stress on the electro-mechanical response of 8/65/35 PLZT, Acta Mater., 44, pp. 4137–4148.

C. Manu (1985), Complete Quadratic Isoparametric Finite-Elements in Fracture-Mechanics Analysis, International Journal for Numerical Methods in Engineering, 21, pp. 1547-1553.

M. Malhorta, P.M. Pinsky (1996), A matrix-free interpretation of the non-local Dirichlet-to-Neumann radiation boundary condition, Int. J. Numer. Meth. Engrg., 39, pp. 3705–3713.

L. J. McGilly, A. Schilling, and J. M. Gregg (2010), Domain Bundle Boundaries in Single Crystal BaTiO3 Lamellae: Searching for Naturally Forming Dipole Flux-Closure/Quadrupole Chains Nano Letters, 10, pp. 4200-4204.

R. M. McMeeking (1977), Finite Deformation Analysis of Crack-Tip Opening in Elastic-Plastic Materials and Implications for Fracture, Journal of the Mechanics and Physics of Solids, 25, pp. 357-381.

R. M. McMeeking and J. R. Rice (1975), Finite-Element Formulations for Problems of Large Elastic-Plastic Deformation, International Journal of Solids and Structures, 11, pp. 601-616.

R. M. McMeeking and A. G. Evans (1982), Mechanics of transformation toughening in brittle materials, J. Am. Ceram. Soc., 65, pp. 242–246.

J. C. Nagtegaal, D. M. Parks and J. R. Rice (1974), On numerically accurate finite element solutions in the fully plastic range, Comp. Meths. Appl. Mech. Eng., 4, pp. 153-178.

J. Novak, U. Bismayer and E. K. H. Salje (2002), Simulated equilibrium shapes of ferroelastic needle domains, J. Phys. Condens. Matter, 14, pp. 657.

P. R. Pontis, N. Tsou and J. E. Huber (2011), A review of domain modeling and domain imaging techniques in ferroelectric crystals, Material, 4, pp. 417-447.

P. Potnis, J. Huber (2012), In-situ observation of needle domain evolution in barium titanate single crystals Journal of the European Ceramic Society, In press.

M. J. Reece and F. Guiu (2002), Toughening produced by crack-tip-stress-induced domain reorientation in ferroelectric and/or ferroelastic materials, Phil. Mag. A, 82, pp. 29–38.

J.R. Rice (1967), Stresses Due to a Sharp Notch in a Work-Hardening Elastic-Plastic Materials Loaded by Longitudinal Shear, Journal of Applied Mechanics, 34, pp. 287-298.

J.R. Rice (1968), A Path Independent Integral and Approximate Analysis of Strain Concentration by Notches and Cracks, Journal of Applied Mechanics, 35, pp. 379-386.

J.R. Rice (1968), Mathematical Analysis in the Mechanics of Fracture, Fracture: An Advanced Treatise, vol. II, ed. Liebowitz, H., Academic Press, New York, pp. 191-311.

J. R. Rice and J. F. Rosengren (1968), Plane Strain Deformation Near a Crack Tip in a Power-Law Hardening Material, Journal of the Mechanics and Physics of Solids, 16, pp. 1-12.

J. R. Rice and E. P. Sorenson (1978), Continuing Crack-Tip Deformation and Fracture for Plane-Strain Crack Growth in Elastic-Plastic Solids," Journal of the Mechanics and Physics of Solids, 26, pp. 163-186.

J. R. Rice (1974), Limitations to Small-Scale Yielding Approximation for Crack Tip Plasticity, Journal of the Mechanics and Physics of Solids, 22, pp. 17-26.

J. R. Rice and D.M. Tracey (1973), Computational Fracture Mechanics," Numerical and Computer Methods in Structural Mechanics, Academic Press, New York, pp. 585-623.

J. F. Scott (2000), Ferroelectric Memories, Springer, New York.

E. H. Salje and Y. Ishibashi (1996), Mesoscopic structures in ferroelastic crystals: needle twins and right angle domains, J. Phys. Condens. Matter, 8, pp. 8477-8495.

E. H. Salje, A. Buckley, G. Van Tendeloo, Y. Ishibashi and G. Nord Jr. (1998), Needle twins and right-angled twins in minerals; comparison between experiment and theory, American Mineralogist, 83, pp. 811–822.

G. A. Schneider (2007), Influence of electric field and mechanical stress on the fracture of ferroelectrics, Ann. Rev. Mater. Res., 37, pp. 491–538.

C.F. Shih (1974), Small Scale Yielding Analysis of Mixed Mode Plane Strain Crack Problems, ASTM STP 560, pp. 187-210.

C.F. Shih (1981), Relationships Between the J-integral and the Crack Opening Displacement for Stationary and Extending Cracks, Journal of the Mechanics and Physics of Solids, 29, pp. 305-326.

C.F. Shih, H.G. Delorenzi and M.D. German (1976), Crack Extension Modeling with Singular Quadratic Isoparametric Elements, International Journal of Fracture, 12, pp. 647-651.

Y. C. Shu and K. Bhattacharya (2001), Domain patterns and macroscopic behavior of ferroelectric materials, Philos. Mag. B, 81, pp. 2021-54.

C. Song and J. P. Wolf (2002), Semi-analytical representation of stress singularities as occurring in cracks in anisotropic multi-materials with the scaled boundary finite-element, Computers & Structures, 80, pp. 183-197.

Y. C. Song, A. K. Soh and Y. Ni (2007), Phase field simulation of crack tip domain switching in ferroelectrics, Journal of Physics D: Applied Physics, 40, pp. 1175–1182.

Z. Sou, C.M. Kuo, D.M. Barnett and J.R. Willis (1992), Fracture Mechanics for Piezoelectric Ceramics, Journal of the Mechanics and Physics of Solids, 40, pp. 739-765.

P.S. Steif (1987), A Semi-Infinite Crack Partially Penetrating a Circular Inclusion, Journal of Applied Mechanics, 54, pp. 87-92.

M. Stern (1979), Families of Consistent Conforming Elements with Singular Derivative Fields, International Journal for Numerical Methods in Engineering, 14, pp. 409-421.

A.N. Stroh (1958), Dislocations and Cracks in Anisotropic Elasticity, Philosophical Magazine, 3, pp. 625-646.

Y. Su and C. M. Landis (2007), Continuum thermodynamics of ferroelectric domain evolution: Theory, finite element implementation and application to domain wall pinning, Journal of the Mechanics and Physics of Solids, 55, pp. 280-305.

A. K. Tagantsev, L. E. Cross and J. Fousek (2010), Domains in ferroic crystals and thin films, Springer, New York.

T.C.T. Ting (1996), Anisotropic Elasticity: Theory and Applications, Oxford University Press, New York.

N. T. Tsou and J. E. Huber (2010), Domain evolution of herringbone structures in ferroelectric single crystals, Smart Materials, Adaptive Structures and Intelligent Systems, ASME, New York.

Y. Wang and R. Ballarini (2003), A Long Crack Penetrating a Circular Inhomogeneity, Meccanica, 38, pp. 579-593.

J. Wang and C. M. Landis (2004), On the fracture toughness of ferroelectric ceramics with electric field applied parallel to the crack front, Acta Mater., 52, pp. 3435–3446.

J. Wang and C. M. Landis (2006), Effects of in-plane electric fields on the toughening behavior of ferroelectric ceramics, J. Mech. Mater. Struct., 1, pp. 1075–1095.

M.L. Williams (1957), On the Stress Distribution at the Base of a Stationary Crack, Journal of Applied Mechanics, 24, pp. 109-114.

Y. Xu (1991), Ferroelectric Materials and Their Applications, North-Holland, Amsterdam, NL.

B. Yang and K. Ravi-Chandar (1999), Evaluation of elastic T-stress by the stress difference method, Engineering Fracture Mechanics, 64, pp. 589-605.

W. Yang and T. Zhu (1998), Switch toughening of ferroelectrics subjected to electric fields, J. Mech. Phys. Solids, 46, pp. 291–311.

W. Zhang and K. Bhattacharya (2005), A computational model of ferroelectric domains. Part I: model formulation and domain switching, Acta Materialia, 53, pp. 185-198.